Doctoral Dissertation

Doctoral Program in Aerospace Engineering (31thcycle)

in cotutelle with

Universidad Carlos III de Madrid

Interuniversity Doctoral Program in Fluid Mechanics

Conflict Resolution Algorithms for Optimal Trajectories in Presence of Uncertainty

By

Daniele Giuseppe Mazzotta

******

Supervisor(s):

Prof. Lorenzo Casalino

Prof. Manuel Soler Arnedo

Doctoral Examination Committee:

To be defined.

Politecnico di Torino

July, 2019

Declaration

This thesis is licensed under a Creative Commons License, Attribution - Noncommercial - NoDerivative Works 4.0 International: see www.creativecommons.org. The text may be reproduced for non-commercial purposes, provided that credit is given to the original author.

This dissertation is presented in partial fulfillment of the requirements for Ph.D. degree in the Graduate School of Politecnico di Torino (ScuDo) in **co-tutorship** with Doctoral School of Universidad Carlos III de Madrid, Spain.

I hereby declare that, the contents and organization of this dissertation constitute my own original work and does not compromise in any way the rights of third parties, including those relating to the security of personal data.

Daniele Giuseppe Mazzotta

July, 2019

I would like to dedicate this thesis to
Lia e Nino,
my life.

Acknowledgements

Un edificante ringraziamento alla persona che ha impersonato nel modo più aulico la 'locura en Abril', grazie avvocato. Grazie a Luca Rota, hai spronato la mia persona in un momento chiave e delicato di questa tesi.

Ad ogni singolo ed impagabile momento trascorso assieme alle persone a Torino. In particolare, ad Andrea il Cattivo, Alessandro, e Andrea Casini, va un grazie speciale per l'infinita pazienza.

Un sincero e sentito ringrazimento a Sara, che ha supportato, sopportandomi nel modo più coraggioso e onesto, questo mio percorso.

Ad Ilenia, ancora di saggezza, di luce, di inestimabili consigli, e profonda conoscitrice delle più oscure fatiche resesi necessarie.

Alla mia famiglia, Mamma e Papá, coloro che, dall'inizio della mia vita, hanno realmente reso possibile tutto questo.

Grazie

Abstract

The objective of the work presented in this Ph.D. thesis is to develop a novel method to address the aircraft-obstacle avoidance problem in presence of uncertainty, providing optimal trajectories in terms of risk of collision and time of flight. The obstacle avoidance maneuver is the result of a Conflict Detection and Resolution (CD&R) algorithm prepared for a potential conflict between an aircraft and a fixed obstacle which position is uncertain.

Due to the growing interest in Unmanned Aerial System (UAS) operations, CD&R topic has been intensively discussed and tackled in literature in the last 10 years. One of the crucial aspects that needs to be addressed for a safe and efficient integration of UAS vehicles in non-segregated airspace is the CD&R activity. The inherent nature of UAS, and the dynamic environment they are intended to work in, put on the table of the challenges the capability of CD&R algorithms to handle with scenarios in presence of uncertainty. Modeling uncertainty sources accurately, and predicting future trajectories taking into account stochastic events, are rocky issues in developing CD&R algorithms for optimal trajectories. Uncertainty about the origin of threats, variable weather hazards, sensing and communication errors, are only some of the possible uncertainty sources that make jeopardize air vehicle operations.

In this work, conflict is defined as the violation of the minimum distance between a vehicle and a fixed obstacle, and conflict avoidance maneuvers can be achieved by only varying the aircraft heading angle. The CD&R problem, formulated as Optimal Control Problem (OCP), is solved via indirect optimal control method. Necessary conditions of optimality, namely, the Euler-Lagrange equations, obtained from calculus of variations, are applied to the vehicle dynamics and the obstacle constraint modeled as stochastic variable. The implicit equations of optimality lead to formulate a Multipoint Boundary Value Problem (MPBVP) which solution is in

general not trivial. The structure of the optimality trajectory is inferred from the type of path constraint, and the trend of Lagrange multiplier is analyzed along the optimal route. The MPBVP is firstly approximated by Taylor polynomials, and then solved via Differential Algebra (DA) techniques.

The solution of the OCP is therefore a set of polynomials approximating the optimal controls in presence of uncertainty, i.e., the optimal heading angles that minimize the time of flight, while taking into account the uncertainty of the obstacle position. Once the obstacle is detected by on-board sensors, this method provide a useful tool that allows the pilot, or remote controller, to choose the best trade-off between optimality and collision risk of the avoidance maneuver. Monte Carlo simulations are run to validate the results and the effectiveness of the method presented. The method is also valid to address CD&R problems in presence of storms, other aircraft, or other types of hazards in the airspace characterized by constant relative velocity with respect to the own aircraft.

Sommario

L'obiettivo del lavoro presentato in questa tesi di dottorato è la ricerca e lo sviluppo di un nuovo metodo di anti collisione velivolo-ostacolo in presenza di incertezza, fornendo traiettorie ottimali in termini di rischio di collisione e tempo di volo.

La manovra di anticollisione è il risultato di un algoritmo di detezione e risoluzione dei conflitti, in inglese Conflict Detection and Resolution (CD&R), che risolve un potenziale conflitto tra un velivolo e un ostacolo fisso la cui posizione è incerta.

A causa del crescente interesse nelle operazioni che coinvolgono velivoli autonomi, anche definiti Unmanned Aerial System (UAS), negli ultimi 10 anni molte ricerche e sviluppi sono state condotte nel campo degli algoritmi CD&R. Uno degli aspetti cruciali per un'integrazione sicura ed efficiente dei velivoli UAS negli spazi aerei non segregati è l'attività CD&R. La natura intrinseca degli UAS e l'ambiente dinamico in cui sono destinati a lavorare, impongono delle numerose sfide fra cui la capacità degli algoritmi CD&R di gestire scenari in presenza di incertezza. La modellizzazione accurata delle fonti di incertezza e la previsione di traiettorie che tengano conto di eventi stocastici, sono problemi particolarmente difficoltosi nello sviluppo di algoritmi CD&R per traiettorie ottimali. L'incertezza sull'origine delle minacce, zone di condizioni metereologiche avverse al volo, errori nei sensori e nei sistemi di comunicazione per la navigazione aerea, sono solo alcune delle possibili fonti di incertezza che mettono a repentaglio le operazioni degli aeromobili.

In questo lavoro, il conflitto è definito come la violazione della distanza minima tra un veicolo e un ostacolo fisso, e le manovre per evitare i conflitti possono essere ottenute solo variando l'angolo di rotta dell'aeromobile, ovvero virando. Il problema CD&R, formulato come un problema di controllo ottimo, o Optimal Control Problem (OCP), viene risolto tramite un metodo indiretto. Le condizioni necessarie di ottimalità, vale a dire le equazioni di Eulero-Lagrange derivanti dal calcolo delle variazioni, sono applicate alla dinamica del velivolo e all'ostacolo modellizato come

una variabile stocastica. Le equazioni implicite di ottimalità formano un problema di valori al controno multipunto, Multipoint Boundary Value Problem(MPBVP), la cui soluzione in generale è tutt'altro che banale. La struttura della traiettoria ottimale viene dedotta dal tipo di vincolo, e l'andamento del moltiplicatore di Lagrange viene analizzato lungo il percorso ottimale. Il MPBVP viene prima approssimato con un spazio di polinomi di Taylor e successimvamente risolto tramite tecniche di algebra differenziale, in inglese Differential Algebra (DA).

La soluzione del OCP è quindi un insieme di polinomi che approssima il controllo ottimo del problema in presenza di incertezza. In altri termini, il controllo ottimo è l'insieme degli angoli di prua del velivolo che minimizzano il tempo di volo e che tenendo conto dell'incertezza sulla posizione dell'ostacolo. Quando l'ostacolo viene rilevato dai sensori di bordo, questo metodo fornisce un utile strumento al pilota, o al controllore remoto, al fine di scegliere il miglior compromesso tra ottimalità e rischio di collisione con l'ostacolo. Simulazioni Monte Carlo sono eseguite per convalidare i risultati e l'efficacia del metodo presentato. Il metodo è valido anche per affrontare problemi CD&R in presenza di tempeste, altri velivoli, o altri tipi di ostacoli caratterizzati da una velocità relativa costante rispetto al proprio velivolo.

Resumen

El objetivo del trabajo presentado en esta tesis doctoral es la búsqueda y el desarrollo de un método novedoso de anticolisión con osbstáculos en espacios aéreos en presencia de incertidumbre, proporcionando trayectorias óptimas en términos de riesgo de colisión y tiempo de vuelo.

La maniobra de anticolisión es el resultado de un algoritmo de detección y resolución de conflictos, en inglés Conflict Detection and Resolution (CD&R), preparado para un conflicto potencial entre una aeronave y un obstáculo fijo cuya posición es incierta.

Debido al creciente interés en las operaciones de vehículos autónomos, también definidos como Unmanned Aerial System (UAS), en los últimos 10 años muchas investigaciones se han llevado a cabo en el tema CD&R. Uno de los aspectos cruciales que debe abordarse para una integración segura y eficiente de los vehículos UAS en el espacio aéreo no segregado es la actividad CD&R. La naturaleza intrínseca de UAS, y el entorno dinámico en el que están destinados a trabajar, suponen un reto para la capacidad de los algoritmos de CD&R de trabajar con escenarios en presencia de incertidumbre. La precisa modelización de las fuentes de incertidumbre, y la predicción de trayectorias que tengan en cuenta los eventos estocásticos, son problemas muy difíciles en el desarrollo de algoritmos CD&R para trayectorias óptimas. La incertidumbre sobre el origen de las amenazas, condiciones climáticas adversas, errores en sensores y sistemas de comunicación para la navegación aérea, son solo algunas de las posibles fuentes de incertidumbre que ponen en peligro las operaciones de los vehículos aéreos.

En este trabajo, el conflicto se define como la violación de la distancia mínima entre un vehículo y un obstáculo fijo, y las maniobras de anticolisión se pueden lograr variando solo el ángulo de rumbo de la aeronave, es decir virando. El problema CD&R, formulado como problema de control óptimo, o Optimal Control Problem

(OCP), se resuelve a través del método de control óptimo indirecto. Las condiciones necesarias de optimalidad, es decir, las ecuaciones de Euler-Lagrange que se obtienen a partir del cálculo de variaciones, son aplicadas a la dinámica de la aeronave y al obstáculo modelizado como variable estocástica. Las ecuaciones implícitas de optimalidad forman un problema de valor de frontera multipunto (MPBVP) cuya solución en general no es trivial. La estructura de la trayectoria de optimalidad se deduce del tipo de vínculo, y la tendencia del multiplicador de Lagrange se analiza a lo largo de la ruta óptima. El MPBVP se aproxima en primer lugar a través de un espacio de polinomios de Taylor, y luego se resuelve por medio de técnicas de álgebra diferencial, en inglés Differential Algebra(DA).

La solución del OCP es un conjunto de polinomios que aproximan los controles óptimos en presencia de incertidumbre, es decir, los ángulos de rumbo óptimos que minimizan el tiempo de vuelo teniendo en cuenta la incertidumbre asociada a la posición del obstáculo. Una vez que los sensores a bordo detectan el obstáculo, este método proporciona una herramienta muy útil que permite al piloto, o control remoto, elegir el mejor compromiso entre optimalidad y riesgo de colisión con el obstáculo. Se ejecutan simulaciones de Monte Carlo para validar los resultados y la efectividad del método presentado. El método también es válido para abordar los problemas de CD&R en presencia de tormentas, otras aeronaves u otros tipos de obstáculos caracterizados por una velocidad relativa constante con respecto a la propia aeronave.

Contents

List of Figures

List of Tables

Nomenclature

Roman Symbols

$\mathbf{J}$	Jacobian matrix
$\boldsymbol{u}$	System controls vector
$\mathscr{L}$	Lagrangian Function
$\mathscr{M}$	Taylor polynomial map
$\mathscr{T}$	Taylor polynomial approximation
C	Path constraint
C_D	Aerodynamics drag coefficient
C_L	Aerodynamics lift coefficient
D	Vehicle aerodynamic drag
E	East coordinate
g	Constant gravitational acceleration
H	Hamiltonian function or Vehicle altitude
J	Cost function
L	Lagrangian cost term or vehicle aerodynamic lift
M	Mach number
m	Vehicle gross mass

N	North coordinate
T	Vehicle thrust
V	Vehicle true air speed

Greek Symbols

χ, ψ	Vehicle heading angle
$\delta_{(\cdot)}$	Independent variable of Taylor expansion
Γ	Vehicle-Obstacle minimum lateral separation or obstacle radius
γ	Flight path angle
λ	Equality constraint Lagrange multiplier
$\boldsymbol{\Pi}$	vector of costate multiplier
$\boldsymbol{\psi}$	Vector of boundary conditions
$\boldsymbol{\Sigma}$	Covariance matrix
$\boldsymbol{x}$	System states vector
μ	Vector of expected value or inequality constraint Lagrange multiplier
ϕ	Vehicle bank angle or Mayer cost term.
ψ	Vehicle heading angle

Acronyms

ADS-B	Automatic Dependent Surveillance - Broadcast
AFRL	Air Force Research Laboratory
ATM	Air Traffic Management
CD&R	Conflict detection and Resolution
COTS	Commercial Off-The-Shelf
CPDLC	Controller-Pilot Data-Link Communication

DA	Differential Algebra
DACE	Differential Algebra Computational Engine
EASA	European Aviation Safety Agency
EO	Electro-Optical
FAA	Federal Aviation Authority
FMS	Flight Management System
FOR	Field of Regard
FOV	Field of View
FPA	Flight Path Angle
GNC	Guidance Navigation and Control
GNSS	Global Navigation Satellite Systems
GPS	Global Positioning System
HLGL	Hermite-Legendre-Gauss-Lobatto
HOCP	Hybrid Optimal Control Problem
ICAO	International Civil Aviation organization
IMC	Instrument Meteorological Condition
IR	Infra-Red
LIDAR	Light Detection And Ranging or Laser Imaging Detection And Ranging
LOAM	Laser Obstacle Avoidance and Monitoring
LoC	Level of Confidence
MC	Monte Carlo
MINLP	Mixed-Integer Non-Linear Programming

MIOCP	Mixed-Integer Optimal Control Problem
MPBVP	Multi-Point Boundary Value Problem
NASA	National Aeronautics and Space Administration
NFZ	No-Fly Zone
NLP	Non-Linear Programming
OCP	Optimal Control Problem
ODE	Ordinary Differential Equation
OR	Operational Research
PANCAS	Passive Acoustic Non-cooperative Collision-Alert System
PCFA	Persistent Contrail Formation Area
PDF	Probability Density Function
RPAS	Remotely Piloted Aircraft Systems
S&A	Sense and Avoid
SAR	Synthetic Aperture radar
SDC	Standard Deviation Curve
SQP	Sequential Quadratic Programming
TAS	True Air Speed
TCAS	Traffic alert and Collision Avoidance System
ToF	Time of Flight
TSFC	Thrust Specific Fuel Consumption
UAS	Unmanned Aerial System
UAV	Unmanned Aerial Vehicle
UTM	UAS Traffic Management
VMC	Visual Meteorological Condition

Chapter 1

Introduction

1.1 Motivation

Typical Sense and Avoid (S&A), or Conflict Detection and Resolution (CD&R) techniques can be defined as the sequence of processes that lead a vehicle to a) identify an hazards along its route, b) run decision making processes regarding the evasion action, c) plan, optimize, and schedule the avoidance maneuver, d) and finally guide and control the vehicle along its conflict-free path.

The main goal of this Ph.D. activity is to find innovative and effective CD&R methods, in the field of optimization and path planning, for providing optimal deconfliction routes in presence of uncertainty. Since the sensing, decision, and guidance tasks are not treated in this work, the acronym CD&R is used here to refer only to the conflict resolution task, excluding the detection part. Beyond the Ph.D. main scope, this work is required also for safe integration of Remotely Piloted Aircraft System (RPAS)[1] into existing current Air Traffic Management (ATM) network.

The first step of the work was to depict a wide spectrum of the CD&R algorithms already available in literature, and some relevant works under development on this topic. Thus, the problem of CD&R has been tackled via different approaches, and all of them have been based on the formulation of Optimal Control Problems (OCPs). This review has been done to test the effectiveness of some existing algorithms

---

[1]A set consisting of a remotely piloted vehicle, relative remote pilot station(s), the command and control links, and any other elements required during the unmanned vehicle operations [3].

purposed for CD&R problems, and for building up a road-map leading finally to the method and the results presented in this work. The review is presented in Section 2.2.

After depicting a non-exhaustive big picture of CD&R algorithms available in literature, the method developed in this work is presented. The method relies on an analytic tool providing optimal free conflict trajectories in presence of an obstacle affected by spatial uncertainty. The stochastic obstacle avoidance problem is formulated as Optimal Control Problem (OCP), and differential algebra techniques are then used to give an approximation of the optimal solution in presence of uncertainty.

1.2   Paving the way for UASs integration

In the current air transportation context, an imminent evolution is needed. More players and innovative solutions are required to cope with the continuous growth of air traffic demand, increasing fuel cost, and emerging concerns over the environmental impact of air transportation sector. Additionally, Unmanned Aerial Systems(UASs)[2] are drawing ever more interest and attention in various civilian and military applications. In facts, due to their versatility, low cost, and vast capabilities in terms of intelligence, surveillance and reconnaissance purposes, UASs are the next novel aircraft that will share the sky with manned aviation. Nonetheless, the enabling technologies needed for the complete integration of UAS with the Air Traffic Management (ATM) context are still less developed in terms of maturity when compared to that of manned systems.

The hurdles for the safe integration of UASs in the mainstream manned airspace operations are numerous. As shown in Figure 1.1, the inabilities of current ATM paradigm can be grouped in four main areas: communication capabilities, onboard and ground-based reliable S&A technologies, aviation infrastructure and regulatory framework, and human-autonomous systems interaction.

---

[2]Aircraft and all associated elements which are controlled with no pilot on board[3].
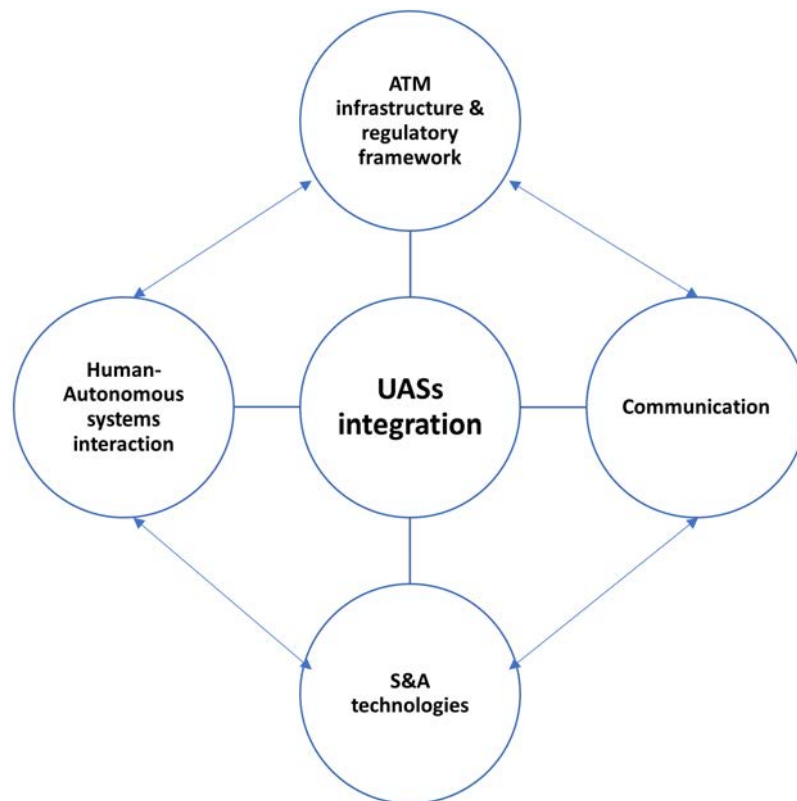
Figure 1.1: Hurdles of UASs operations integration.

Current communication capabilities, as an example, force civil UASs operation to share transmission bandwidth with mobile phones or other telecommunication infrastructure, limiting the ability to coordinate multi UASs and manned aircraft operations with ground. In UASs operations there are no flight rules, no visual-line-of-sight and beyond visual-line-of sight rules, and there could be areas where civil and military radars, or just solar panels, can interfere with the communications between manned and UASs vehicles. An important aspect concerns also the 4.5G telecommunications services. Indeed, some UTM developer using the 4.5G as communication network might experience incompatible latency to receive navigation messages.

Another obstacle is represented by the absence of robust and reliable S&A techniques which allows UASs to operate safely in presence of uncertainty, or unexpected events. The scenario become more complex if one compares centralized systems, i.e., those systems where an human o computer is put as central supervisor

and monitor operations, with decentralized systems, where vehicles communicate with each other, are entrusted with certain level of awareness and decision, and can take some actions autonomously.

The limitations of the current centralized ATM network, the lack of definitive and complete procedures and standards issued by certification authorities, and concerns related to airspace users and general public, are other challenges to cope with for allowing manned aircraft and UASs to cohabit in the same airspace. Finally, the interaction between autonomous systems and humans make rockier the integration of UASs operations. Indeed, the current ATM infrastructure has been, since its birth, conceived as human-centric. When multiple autonomous operators are allowed to join into this paradigma, new studies are needed to understand how humans and autonomous systems can work collaboratively, optimizing their capabilities, without obliterating the advantages of autonomous systems.

As a result, it can be affirmed that there are still issues of integrity, security, availability and continuity for the UASs operation integration [1]. Moreover, the above mentioned aspects indicate that the remaining challenges toward the safe and effective implementation of a human-automation collaborative system for UASs operations are still numerous.

Several efforts have been done to improve the telecommunication aspects in decentralize systems [4]. Similarly, novels technologies and new protocols are growing to support Communication, Navigation, and Communication (CNS) systems among manned and unmanned vehicles. Advance in Flight Management Systems (FMS), as an example, allow modern aircraft to compute and plan precise trajectories even in presence of adverse meteorological conditions [5]. Aerospace industry is also working on implementing important key technologies, such as, the Controller-Pilot Datalink Communication (CPDLC) protocol that could alleviate voice-communication frequencies and can reduce errors in voice message transmissions, Global Navigation Satellite Systems (GNSS), or the Automatic Dependent Surveillance-Broadcast (ADS-B). As far as sensing technique is concerned, ADS-B has gained considerable interest as sensing technology [2] for the CD&R capability. ADS-B is a system used to transmit and receive information of 3D position, velocity, bearing and intent of other aircraft. The accuracy of navigation data broadcast airborne, the maturity of the well proven communication technology, and its flexible

structure, make the ADS-B a favorable candidate for the integration of UASs in non-segregate space [6].

Concerning the computational compatibility of human and autonomous systems working collaboratively, and in an optimal manner, the works of [7, 8] expose clearly the challenges, the methods, and the technological enhancements needed for the collaborative human-UASs interaction.

The European Aviation Safety Agency (EASA), EUROCONTROL, and the International Civil Aviation Organization (ICAO), have been working together in the last years to pave the way for a unified UAS regulatory framework. "*The key challenge for drone operators is to establish trust with the manned aviation stakeholders – traditional airspace users, air navigation service providers (ANSPs), pilots, controllers and airports – who are often still in resistance mode when it comes to sharing airspace*". The worlds of Philippe Merlo, EUROCONTROL's Director of ATM, shows that the parties involved in the UAS Traffic Management (UTM) are numerous. As a consequence, EUROCONTROL objectives are mainly focused on developing a strong and common operation area, where every single operator involved is precisely aware of the objectives and speak the same language. The roadmap envisaged for the European UTM concept implementation is shown in Figure 1.2 [1]. On the other side, also United States have been working on addressing the key elements for UASs integration. In 2017 in facts, Federal Aviation Authority (FAA) gathered more than 60 people [1] in the Unmanned Aircraft System (UAS) Integration Pilot Program (IPP) [9] working on UASs integration issues.

Timescale	UTM services	RPAS integration
2019 plus	**U1 UTM Foundation services** • e registration • e identification • geo-fencing	RPAS 1 – IFR in classes A-C
2022 plus	**U2 UTM Initial services** • flight planning • flight approval • tracking • airspace dynamic information • procedural interface with ATC	RPAS 2 – IFR in classes A-G
2027 plus	**U3 UTM Advanced/enhanced services** • capacity management • assistance for conflict detection	
2030 plus		RPAS 3 – IFR and VFR in classes A-G
2035 plus	**U4 UTM Full services** • additional new services and integrated interfaces with manned aviation	

Figure 1.2: UTM implementation roadmap (courtesy of EUROCONTROL [1]).

It is clear that all partners agree on the following: the main aspect that need to be addressed for the development of a safe and reliable UTM, is the S&A technological part. Actually, in the course of the implementation of UAS operations into the existing ATM, it is requested that the S&A performance in UAS operations must offer a safety range equaling or exceeding that of manned aircraft. Albeit manned aircraft are already equipped by radars, transponders and other sensing techniques, the sense and avoid problem usually attempts to detect conflicts at very-near sensing limits, when the separation with the potential target is so short to make the response time the most critical factor. Thus, the potential midair collision avoidance is more dependent on the human eyesight capability, and without the human intervention, UASs have to solely rely on the S&A performance. As a consequence, delivering human-like capability for UASs makes the development of S&A very challenging. A part of an increased autonomy and robustness of UAS systems, it is also required that S&A system for UAS should be capable of operating under adverse weather conditions [10], and in presence of uncertainties or unexpected events. The growing

interest in stochastic algorithms, i.e. methods which can handle with uncertain events, is motivated by the need to address specific objectives also in dynamic environments, those environments subject to unexpected conditions, such as, new tasks emerging, changing weather, and potential Ultraviolet (UV) degradations. In this view, S&A for UAS are the keys for a robust and safe integration of UASs to gain access to civil airspace.

To this purpose, the focus of this work is to build a big picture of the sensing techniques available nowadays for S&A purposes, and provide a novel CD&R algorithm suitable for conflict-free optimal path planning in presence of uncertainty. Section 2.3 is a review of the existing technologies, emerging techniques and potential future challenges for the design of feasible S&A systems.

1.3   Objectives

The overall objective of the work presented in this thesis is to propose a new method to solve CD&R problems in presence of uncertainty. Without loss of generality, the objective and scopes of this work can be briefly summarized as follow:

- **Mathematical Framework**

    – Contribute in an innovative manner to improve and provide new mathematical tools for CD&R problems;

    – Propose a novel approach to solve stochastic OCP via indirect method by employing an algebra of Taylor polynomials to solve Multi-Point Boundary Value Problems (MPBVPs) and approximate the optimal solution;

- **Technological Framework**

    – Enhance quasi-real-time deconflicting technologies, such as, S&A for safe integration of UASs in non-segregated airspace;

- **ATM Operational Paradigm Framework**

    – Provide new algorithms for overhauling ATM congested airspaces, or in presence of stochastic events, such as, weather hazards, loss of aircraft-aircraft or aircraft-ground communication, misleading on-board data;

As discussed in previous sections, when uncertainties are included into CD&R problems, optimal control has to cope with unknown variables and parameters that add complexity to the OCP. Under this scope, the optimal control theory aims at finding the control variables of a system that minimize a user-defined cost in a stochastic manner, i.e., achieving the prescribed objective with a specific level of confidence. The aim of the work is also to provide different tools for modeling stochastic obstacles in CD&R problems. On one hand, pilots and remote controllers can be rely on such instruments to correctly applying avoidance maneuver while minimizing risk of collision and maintaining mission performance. On the other hand, autopilots and Guidance Navigation and Control (GNC) techniques could surely benefit from the results of such tools in the automatization of planning and tracking optimal conflict-free maneuvers.

1.4   Methodology

The stochastic obstacle avoidance problem tackled in this work is formulated as Optimal Control Problem (OCP). The obstacle conflict is defined as the violation of the minimum distance between the vehicle and the fixed obstacle, and conflict avoidance maneuvers can be achieved by varying the heading angle of the aircraft. The CD&R OCP is solved via indirect optimal control method. Necessary conditions of optimality, namely, the Euler-Lagrange equations, are obtained from calculus of variations, the obstacle constraint is modeled as stochastic variable, and it is included in the OCP. The implicit equations of optimality lead to formulate a Multi-Point Boundary value problem (MPBVP) which solution is in general not trivial. The MPBVP is firstly approximated by Taylor polynomials space, and then solved via Differential Algebra (DA) techniques.

The key role of DA techniques is to provide efficient expansion of arbitrary functions as Taylor polynomial, by replacing floating point operations with corresponding DA operations on a computer. In DA environment, sufficiently smooth functions can be operated on in an algebraic fashion similarly to real numbers. Therefore, DA efficiently represents functions in a way such that they can be easily defined, combined and evaluated through simple arithmetic expressions. Additionally, it is also possible to perform inversion of functions, explicit solution of nonlinear system, and differentiation and integration of functions in DA framework. The term differential

algebra therefore comprises both the complete set of the computer representation of polynomial expansion (DA objects), and the set of intrinsic functions and operations available to operate on the polynomials. DA techniques, within the Differential Algebra Computational Engine (DACE) computer framework (see Section 4.7), are used in this thesis to give an approximation of the optimal solution, and to map the obstacle uncertainty. As far as the uncertainty mapper is concerned, DACE is used here to introduce an optimality level, i.e., a probability indicator (related to the real probability) that a given trajectory is the optimal one in terms of flight time and constraint satisfaction. As a consequence, the solution of the OCP presented in this work is a set of polynomials representing the optimal controls in presence of uncertainty, i.e., the optimal heading angles that minimize the time of flight, while taking into account the uncertainty of the obstacle position.

Summarizing, the methodology employed for the resolution of the stochastic OCP has been developed by the following steps:

- conflict scenario is identified by an intended nominal aircraft 2D route conflicting with an obstacle modeled as circular shape;

- due to uncertainty affecting on-board sensors, it is assumed that position of the obstacle center follows a bivariate Gaussian distribution probability density function, while the radius of the obstacle is a known parameter;

- time of flight is chosen as performance index or cost function of the problem, and together with boundary conditions and dynamics of the aircraft, the CD&R problem is formulated as classical OCP;

- the OCP is then solved via optimal indirect method, i.e., by setting and solve the first-order optimality conditions, namely the Euler-Lagrange equations. The result is a Multi-Point Boundary Value Problem (MPBVP) which solution is the heading angle control law leading to a conflict-free trajectory;

- Differential Algebra Computational Tool (DACE) is used to solve the MPBVP by approximating the solution as Taylor polynomial expansion;

- obstacle uncertainty is propagated into the problem by using DACE, and optimal control probability map is obtained;

- Monte Carlo (MC) simulations are run to validate the results of DACE indirect method.

1.5   Contribution Statement

In order to reduce the computational burden required for stochastic methods, and obtain a closed-form analytical expression of the control solution, a novel approach based on indirect optimal control and differential algebra analytical tool is presented. In particular, an aircraft colliding with an uncertain fixed obstacle is considered, and the optimality conditions of the obstacle avoidance OCP are formulated by employing the indirect method approach. Once the CD&R problem is formulated as MPBVP, the polynomial approximation of the solution (solution map) is rapidly addressed by using the Differential Algebra (DA).

Summarizing the discussion above, the main contribution of this work can be stated as follow. A novel indirect optimal control method based on DA techniques to solve a stochastic OCP is introduced. The solution map of the stochastic OCP is obtained at the expense of a very low computational cost, and applicability of this method to other type of hazards (storms, no-fly zones, other aircraft) is straightforward.

1.6   Structure

The rest of the work is organized as follow. Chapter 2 is a survey of the main CD&R algorithms developed in literature, and it describes the main contribution of the thesis. Chapter 3 presents the mathematical formulation of the OCP, the optimality boundary conditions derived from the indirect OCP approach in the cases of constrained or unconstrained problem. Chapter 4 describes the model used to approximate the system, the stochastic constraint, and the optimality boundary conditions applied to the problem considered in this work. The solution approach to the problem is also exposed in Chapter 4 Case study results and Monte Carlo (MC) simulations are exposed in Chapter 5. Finally, conclusions, potential applications, and direction of future research of the proposed CD&R algorithm, are detailed in Chapter 6. Appendices A, B, and C contain some partial results of such future works.

Chapter 2

CD&R Algorithms State-of-the-Art

2.1 Introduction

Conflict Detection and Resolution algorithms have been attracting ever more attention in solving Air Traffic Management conflicts in the last 20 years. In general terms, the process of CD&R consists of: obstacle detection, decision making, trajectory prediction or path planning, and finally, path following. In this work, conflict is defined as the violation of the minimum lateral separation distance between the vehicle and a fixed obstacle. The approach is also valid for any other object modeled as circular shape of a fixed radius which center keeps constant velocity and heading angle. Trajectory prediction process is meant to find the conflict-free maneuver that lead the aircraft from initial to final waypoint, possibly maximizing a customized performance index. To achieve this objective, the surrounding environment, including weather and vehicle hazards, current state, and flight plan of the aircraft have to be considered. Aircraft conflict avoidance can be essentially achieved through three maneuvers: flight level changes, heading angle changes and speed adjustments. Based on these maneuvers, many approaches have been proposed in the last few years to address CD&R problems. A comprehensive survey on CD&R algorithms can be found in [11, 12]. In general terms, a detailed categorization of CD&R algorithms should be done according to numerous characteristics. To mention some of them:

- the dimension of the scenario considered (1D, 2D, or 3D conflict avoidance maneuvers);

- the trajectory propagation method used for establishing the point of potential conflict;

- the type of conflict avoidance maneuver (speed, heading angle, altitude changes or combination of these);

- whether or not uncertainty is included in the problem;

- the metrics used to gauge the potential conflict;

- if the avoidance maneuver is minimizing a sort of customized cost, is determined a priori, or is following other sub optimal rules;

- whether or not the algorithm is working in a cooperative scenario;

- if the algorithm is also prepared for the resolution of conflict against multiple aircraft.

In this work, a high-level categorization is done focusing on the numerical method used to set-up and solve the CD&R problem. The taxonomy available in literature indicates that the methods proposed to solve CD&R problems usually belong the following groups: the wide class of Operational Research (OR), heuristic methods, and Optimal Control Problems (OCP).

In the branch of OR approaches, the authors of [13, 14] proposed two methods to address conflict avoidance by performing aircraft heading angle or speed changes. Both methods are based on geometrical considerations on aircraft trajectories, and the problems are formulated as Mixed-Integer Linear Programming (MILP). Similar problem is also solved via semidefinite programming in [15]. In [16], the author presents a MILP problem that combines both speed and heading angle changes, and relies on space-discretization approach. MINLPs based on aircraft speed and heading angle changes are also solved in [17]. A two-step resolution is proposed in [18], where two MINLPs based on heading angle and speed changes are solved sequentially to avoid conflict and return aircraft to the original route. As highlighted in [13] and [19], the complexity of the CD&R problem increases when speed regulations and heading angle changes are considered simultaneously. These methods are very powerful when numerous instances have to be solved rapidly. On the other hand, they suffer of some drawbacks, such as, the weakness of global theoretical optimality, or the failing convergence of the neighbor solutions.

Concerning the heuristic approaches, various contributions to CD&R problems have been developed so far. Methods range from very simple A*-based algorithms [20, 21], that need to model the entire environment before addressing the conflict resolution, through Rapid-exploring Random Tree approaches [22], to other most sophisticated methods, such as, particle swarm optimization [23, 24], ant colony optimization [25], evolutionary techniques [26], or multi-objective evolutionary algorithm [27]. Although genetic algorithms can address CD&R problems without any specific knowledge of systems dynamics, constraints, or physical limitations, they are strongly penalized by the computational cost, and the weakness of theoretical optimality.

Another class of approaches relies on formulating the CD&R problem as a continuous OCP. According to these methods, the solution control of a given system has to be find, satisfying dynamical and path constraint, and minimizing a user-defined functional cost. The approaches available for the solution of optimal control problems generally belong to two main categories: direct and indirect methods.

Direct methods are meant to cast the infinite-dimensional continuous OCP as a Non-Linear Programming (NLP) problem with finite dimensions [28]. The NLP is then solved using numerical optimization algorithms widely available in literature [29, 28, 30]. The reader is referred to the works of [31] for a wider collection of software available in literature and mainly used for solutions of MINLPs and NLPs.

As an example, in the work of [32] the authors address minimum fuel trajectories satisfying waypoints and no-fly zone constraints, by transcribing the OCP as NLP. The resulting avoidance maneuvers are combination of speed and heading angle changes. The authors of [33] present an approach to commercial aircraft optimal trajectory generation, where discrete flight phases coupled with continuous aircraft dynamics results in a single hybrid optimal control problem. Recently, the hybrid optimal control approach was also used in the Mixed Integer Optimal Control Problem (MIOCP) of [34], where a complete 3-Degree-Of-Freedom flight dynamics is captured, and discrete speed and heading changes maneuver are used to avoid aircraft conflicts. The hybrid optimal solution is then formed by different A/C dynamics that allow the aircraft to change alternately speed and heading angle.

Indirect methods, instead, seek to solve the OCP by satisfying the necessary condition of optimality settled by calculus of variations [35]. The application of the indirect approach, leads to formulate the problem as Multi-Point Boundary-Value

Problem (MPBVP). The MPBVP can be then solved by different techniques available in literature [28], such as, single and multiple shooting, Sequential Quadratic Programming (SQP), or barrier algorithms.

When uncertainties are introduced into the CD&R problem, the solution becomes more complex and computationally expensive [36]. Uncertainties can derive from aircraft sensors, trajectory planning, wind gust, weather hazards, or/and pilot response latencies. Trajectory prediction in presence of such uncertainties has to be as accurate as possible in order to avoid conflicts. In facts, depending on the time instant at which the conflict is estimated to occur, the farther in time the potential conflict is predicted, the less certain the prediction is likely to be. Moreover, accurate modeling of uncertainties is of paramount importance also to preserve degradation of vehicle performance and, ATM network management.

Numerous methods have been developed in the recent years to address the solution of stochastic OCPs. The authors of [37, 38] propose two probabilistic methods to predict future trajectories, and they model the uncertainty associated to the weather as probability density function. Monte Carlo simulations [39], Markov processes [40], Markov-Monte Carlo framework [41], Bayesian optimal design [42], and more recent approaches such as, kriging and polynomial chaos expansion [43, 44] have been also employed for solving probabilistic CD&R problems. The majority the mentioned works employ statistical methods that are, in general, very computational expensive [45]. As result, their implementation is not compatible in real applications of ATM.

2.2   Indirect vs. Direct OCP Approach

Indirect and direct OCP methods essentially follow two different philosophies. On the one hand, the indirect approach relies on the principle "optimize first, then discretize". On the other hand, the direct approach is based on the idea to "discretize first, then optimize". When direct and indirect methods for the OCP solution are compared, there are numerous aspects that have to be considered. The indirect methods suffer some issues, for instance, (a) any change to the model or to the OCP objective, force to derive optimality conditions from scratch; (b) the sequence of trajectory arcs, i.e. the switching structure of the solution of the problem, is unknown a priori. On the other hand, direct methods are affected by other limitations,

such as the weakness of global theoretical optimality, or the failing convergence of the neighbor solutions. The indirect methods are instead characterized by rapid convergence in the neighborhood of the optimal solution [46]. Recent studies [47] have been developing the idea to combine direct and indirect approaches, and get benefits of employing both methods to solve OCPs. The formulation of OCP by indirect methods faces with the difficult task of guessing a proper structure of switching trajectory arcs. As showed in [48], in case of OCP bounded by inequality state constrains, the switching structure of controls, states, and multipliers could assume a well-known configuration. Nevertheless, finding correct structures is often achieved by trial-and-error, and in general it is not a trivial task for the analyst.

The CD&R problems that have been studied, and have given some cues for the development of this work, are briefly summarized here below. Some of them are based on direct methods, and those based on indirect methods are detailed in the appendices of this thesis.

One of the methods investigated for solving the CD&R has been the Hybrid Optimal Control Problem (HOCP) approach [34]. Through this approach, the dynamics of various vehicle sharing the same airspace is activated by discrete variables leading to different flight phases. The choice of which flight phase has to be activated to avoid conflict between aircraft, i.e. speed or heading changes maneuvers, is dictated by the functional cost. The solution of the HOCP has been addressed as follow: the problem has been formulated has Mixed-Integer Optimal Control Problem (MIOCP), discrete variables (the switching variables that lead to the activation of flight phases) are relaxed as continuous leading to a Relaxed MIOCP, and finally, a penalization term is added to functional cost to force the switching variables to assume discrete values. As a result, the problem is cast as classical Non-Linear Programming (NLP) problem and solved via optimal control direct method.

Another approach to solve CD&R scenario between several aircraft has been studied, and it relies on the concept of Subliminal Speed Control (SSC) [19]. The SSC method employs very small variations of the prescribed nominal speed to minimize the overall time of conflict between pairs of aircraft. By adopting very simple aircraft dynamics, and constraining the aircraft speed to small variations around a nominal value (e.g. $V = V_{nom}(1 \pm 5\%)$) the problem is formulated and solved as NLP.

Both CD&R described above are based on optimal control directs methods. The following problems, instead, mainly rely on indirect method and pave the way for future developments of the method presented in this thesis.

In Appendix A, the results of a CD&R problem between a vehicle and a stochastic obstacle is presented. The problem is formulated as OCP and solved via indirect method. The objective of the OCP is to avoid a fixed obstacle in presence of spatial uncertainty, while minimizing a collision indicator, set as Lagrangian cost term. As a result, the CD&R is treated an unconstrained OCP with cost function related to the probability to collide with the obstacle.

Small perturbation theory [49] combined with optimal indirect method has been also considered to solve CD&R problems. Although this approach has been usually used for space applications, it can be applied for CD&R in airspace in principle. The method consists in formulating and solve the collision avoidance problem between multiple aircraft by applying an approximation scheme to the optimal dual problem. The approximation scheme is based on the perturbation theory, a method commonly used to solve ordinary differential equations in space applications. More details of such approach are given in Appendix B.

Appendix C presents the preliminary mathematical formulation of a possible extension of the CD&R solved in Section 4.4. The CD&R optimality conditions, prepared against a moving obstacle, are derived via indirect method.

2.3   Sensing Techniques for CD&R

Sense and avoid is defined [50] as "the capability to see, sense or detect conflicting traffic or other hazards and take the appropriate action."

According to [51], most of the research effort on the S&A problems has been mainly focused on the fields of sensing techniques, decision making and path planning algorithms, rather than on path following techniques. Indeed, once the intruder/obstacle has been detected and the detouring path has been computed, the guidance and control function of the aircraft is a well-known problem which could be addressed routinely without any substantial changes. The selection of the proper sensors for RPAS strongly depends on the RPAS payload capability, the accuracy associated to the sensors, the development and maintenance cost and complexity.

Furthermore, depending on the specific mission that RPAS are meant for, certain sensing platform could be more suitable than others. Depending on how the sensing measurements are acquired and transmitted, S&A are basically grouped into two categories: cooperative and non-cooperative S&A approaches.

- Cooperative approaches consist of sharing the flight information (location, identification, speed, intention, etc.) among the others aircraft equipped with the same systems. In order to address aircraft detection, cooperative sensors require other aircraft in the airspace carry cooperative sensors as well.

- Non-cooperative approaches involve direct sensing of aircraft/object, regardless whether the target desires to be sensed or not. Therefore, since non-cooperative sensors do not expect other aircraft are equipped with the same sensors, air vehicles, birds, weather hazards, and both airborne and ground objects can be detected.

Cooperative sensing techniques

Numerous cooperative sensing approaches have been already extensively developed for manned aircraft. As a matter of fact, Traffic alert and Collision Avoidance System (TCAS) and Automatic Dependent Surveillance – Broadcast (ADS-B) with an integrated Global Positioning System (GPS), have reached already enough maturity as cooperative sensing approaches in manned aviation. TCAS, originally designed for manned aircraft, is a system conceived to reduce the incidence of mid-air collisions. It is capable to transmit and receive transponder information to/from other aircraft equipped by TCAS, and it is able to generate potential conflict alarms by extrapolating range, bearing, altitude of the interrogated A/C. TCAS is able to detect other aircraft up to 160 km [2], it can operate both in Visual Meteorological Condition (VMC) and Instrument Meteorological Condition (IMC), leading to consider such sort of technology suitable for RPAS S&A application [52]. Despite TCAS has been considered a feasible S&A solution for RPASs in civil airspace [53], small/miniature RPASs have very stringent constraints in terms of payload and cost compared to manned systems. Furthermore, communication between manned and unmanned vehicle (RPASs equipped by TCAS should rely on the desire and the availability of other aircraft to share the information), and the limited ability of TCAS to handle with multiple aircraft scenario [2], are all reasons that might prevent

the widespread accommodation of TCAS in RPAS systems. An alternative to the traditional TCAS is described in [54], where a TCAS based collision avoidance logic is optimized to operate on unmanned systems. Another S&A system largely adopted in manned aircraft is the ADS-B. The distinctive features of ADS-B lie on the capability to carry out not only air-to-air communication, but also air-to-ground surveillance and potentially replacing the need of secondary surveillance radars. Another essential features that stems out from the ADS-B characteristics is the type of data transmitted. Via ADS-B, the aircraft is able to exchange a high volume of information: identification, 3D position, speed, heading, time, and intent of the aircraft. Aircraft and ground stations are able to exchange via data-link a thorough depiction of aircraft equipped by ADS-B in airspace up to 240 km radius [2]. This represent an extremely important tool for RPAS collision avoidance. Although the extensive amount of data exchanged by ADS-B could be deemed redundant, verbose, and might limit the system interoperability due to the data bandwidth required [53], ADS-B has gained considerable interest as S&A technology for RPAS [55]. In fact, the accuracy of navigation data broadcasted airborne, the maturity of the well proven communication technologies, and the flexible structure for easing the interoperability of these S&A techniques, make the ADS-B a favorable candidate for RPAS S&A. There are solutions already available in the market providing low-cost and ultralight ADS-B receiver for different kind of RPAS [55–58]. With astounding accessible prices, customizable features, and a wide potential client offers, these cutting-edge technologies are adapting the traditional manned S&A to the emerging needs of novel RPAS sector, so paving the way for an easy integration of RPAS into manned civil airspace.

Non-Cooperative sensing techniques

As stated before, non-cooperative sensors imply that the air vehicles do not have the capability to communicate with each other. Within this approach, in order to detect intruders and recognize hazards the aircraft can solely rely on own detection platform. Therefore, these technologies might also be applied to sensing objects/obstacles both on ground and airborne. Although cooperative S&A allow aircraft to identify potential mid-air conflicts at very large range (hundreds of kilometers), RPASs, due to inherent nature of their operations, they need non-cooperative techniques to prevent aircraft collisions in a very narrow eyesight proximity to the vehicle

(up to tens of kilometers). The time block needed to perform hazard detection, decision making, path planning and avoidance maneuver, is therefore critical for this kind of non-cooperative sensing approach. For the reason above mentioned, non-cooperative S&A for RPAS is considered one of most challenging aspect to be faced toward a safety integration of unmanned aircraft into the existing manned ATM. The classification of non-cooperative S&A includes: radar, Laser/Light Imaging Detection And Ranging (LIDAR), Electro-Optical (EO) system, Infrared (IR) sensor, acoustic system, and novel naturally inspired sensors. In RPAS applications the main drawback of using radar as S&A technique is the high-power consumption [53]. In general, the size, weight, and power constraints of the radar does not match with the limitation of RPASs. Nonetheless, novel systems such as Synthetic-Aperture Radar (SAR) [59] are becoming increasingly interesting solutions for UAS S&A purposes. SAR is an active detection device used to determine location, velocity, and size of targets by creating an image of the object using multiple radar pulses. It also can be used under all-weather conditions since radar pulses can penetrate storms. Recent developments are delivering new and enhanced SAR configurations more suitable for RPAS. As an example, National Aeronautics and Space Administration (NASA) has developed a reconfigurable, polarimetric L-band SAR purposely designed for RPASs and capable to detect objects up to 16 km [60]. Additionally, further research has led to the design of a Doppler radar able to detect miniature RPAS [61]. An alternative and also complementary solution to the SAR is the LIDAR system. LIDAR systems are able to offer higher quality real-time imagery compared to the radars (under 2.5 cm [62]). The operating principle of LIDAR like to that of radar: it estimates distance by illuminating a target with a laser and measuring the time of the returning signal reflected from the object. LIDAR has been largely used for different applications, from meteorological and remote sensing to mapping and infrastructure inspection. The detection capability of such system usually ranges from 200m to 3 km [2]. In general, laser scanning techniques shares many of the limitations in size, weight and power, with radar systems. However, recent advances in LIDAR technologies have led to develop very compact and lightweight systems (3 kg [63], so as to implement such system in RPAS. An example of LIDAR RPAS application is discussed in [64], where the Ibeo Lux Scanner [65] is used to process the laser pulses reflected by the terrain and validate LIDAR applicability for fine-scale mapping. Laser Obstacle Avoidance and Monitoring (LOAM) is also studied in [66], where non-cooperative laser sensing techniques is integrated in a complete S&A system: from

the detection of the obstacles and its classification through the guidance for optimal avoidance maneuver to caution/warnings to ground crew. According to [53], EO sensing approach holds the greatest potential for gaining airworthiness approval as RPAS S&A application. EO systems detect obstacle/objects using airborne imaging sensors in a realistic sensing environment by virtue of reflected natural visible light. Nowadays, the challenging economy, the miniaturization of electronics and the availability of compact, power-efficient and optimized hardware, are delivering EO sensors increasingly compact, lightweight, and lower power consuming [67]. Due to this enhancement, the maturity of such systems allows them to be a feasible and affordable solution for RPAS S&A. Albeit EO sensing techniques offer many benefits and advantage for their application on RPASs, there are still many open challenges to be addressed. Adverse meteorological conditions (dust, fog, smoke, etc.) can badly affect sensors performance; since Field of View (FOV) and Field of Regard (FOR) are critical features for this system, arrays of sensors might be required to achieve wider sight capability; finally, the data provided by EO sensors (bearing and size of the target) are poor in terms of S&A. Other aspects to contend with when using visible light spectrum EO sensors are: lighting conditions of the environment, image backgrounds, and possibly image artefacts. Other problems consist in image jittering noise, caused by the movement of the camera sensor, and the intensive computational load required for image-processing algorithms in real-time. In [68], the development and evaluation of a real-time vision-based collision-detection system for fixed-wing RPASs is exposed. Another example of EO sensors for RPAS S&A is tested by the Air Force Research Laboratory (AFRL) in [69], where a wide-FOR and multisensory imaging system aboard the Global Hawk is capable to detect approaching aircraft real-time. FULMAR X [70] is another example of RPAS integrating multispectral cameras and LIDAR sensors. Alternatively, [71] illustrates the development of a prototype optical sense-and-avoid instrument from low-cost Commercial Off-The-Shelf (COTS) components. The system, installed on a Bell 205 helicopter, has been designed to detect small RPASs in a range of 5-10 km. Within the classification of EO sensing techniques, IR camera is a device that converts light in the same manner of visible-spectrum EO sensors, but sensing longer wavelengths (5μm to 14 μm). With lower resolution than optical cameras, UASs equipped by IR sensors can detect infrared light radiated from an intruder object. Compared to previous applications of IR sensors, such as in the context of missile guidance where target tends to occupy increasingly the FOV, the S&A problem involves the challenging task to discriminate

targets at near sensing limits, when the obstacle/objects have a dimension of few pixels [53, 68]. IR cameras can address specific task not accessible by human eyes, such as night-vision and bad-weather scenario, surveillance, and rescue. Conversely, they are strong affected by weather conditions, and the information provided by the IR sensor contains only bearing data. There has been considerable investigation to use this feature as S&A technique for RPASs [72, 73]. Another interesting approach to RPAS S&A problem is to use acoustic sensors to detect, track and avoid intruder aircraft. Acoustic sensors are a low-cost, effective, and lightweight solution that potentially could tackle the S&A problem identifying intruders in a 360° FOV [74]. This technology is equally effective both in day and night, but the performances are strongly deteriorated by adverse atmospheric conditions (e.g. strong wind or rain). Passive Acoustic Non-cooperative Collision-Alert System (PANCAS) [75] is a good example of novel technology that allows RPASs to detect an approaching aircraft, recognize the conflict hazard, and change course to maintain safe separation distances. With an array of four lightweight acoustic probes, PANCAS represents an excellent solution to detect aircraft by means of sensing the sound of the engines. An outstanding feature of this system is the ability to remove the effects of wind noise and platform vibration. In [76], a low cost, independent, omnidirectional, low power consuming acoustic sensor prototype for RPAS is tested.

A summary of the characteristics of main sensor techologies are summarized in Figure 2.1. An illustration of typical sensing devices with correspondent detection range, are illustrated in Fig. 2.2.

	Information provided	VMC	IMC	SWAP	Cost	Others
TCAS	Range	√	√	×	×	Well proven
	Altitude					Widely used
ADS-B	Position	√	√	×	×	
	Altitude					
	Velocity					Well proven
SAR	Range	√	√	×	×	Typically poor
	Bearing					accuracy
LIDAR	Range	√	√	×	×	Easy
						configuration
						Narrow FOV
EO system	Azimuth	√	×	√	√	Data link
						required
	Elevation					Lack of direct
						range
Acoustic system	Azimuth	√	×	√	√	Data link
						required
	Elevation					Lack of direct
						range
						Delay
IR system	Azimuth	√	×	√	√	Data link
						required
	Elevation					Lack of direct
						range

Note: SWAP: size, weight, and power; √: favorable/applicable; and ×: not favorable/applicable.

Figure 2.1: Main RPAS sensing technologies comparison table (courtesy of [2]).
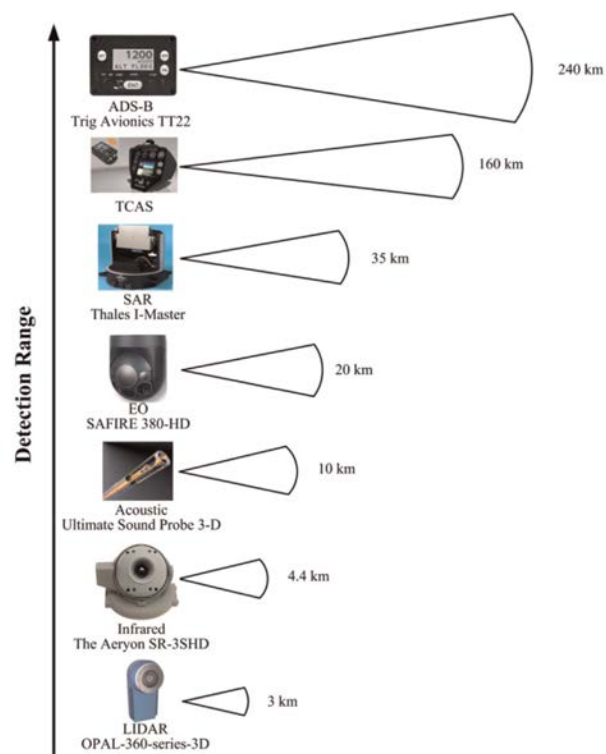
Figure 2.2: Typical RPAS sensing techniques with detection range (courtesy of [2]).

Chapter 3

Optimal Control

3.1 Optimal Control Problem Statement

The dynamic system considered in this research is defined by a state variable vector $\boldsymbol{x}(t) \in \mathbb{R}^n$, and controls $\boldsymbol{u}(t) \in \mathbb{R}^m$, on a time interval $[t_0, t_f]$, in which state variables are governed by a set of first-order differential equations, namely, the state equations $\boldsymbol{f} : \mathbb{R}^n \times \mathbb{R}^m \mapsto \mathbb{R}^n$. Over the time interval from t_0 to t_f, state or control path constraints may entail some discontinuities in system states, in state equations, and/or in controls variables. The time instants between $[t_0, t_f]$ are called interior points or *events*, and the time interval between events will be referred to as *phases*. The time of event i is denoted with t_i, and times just before and after t_i are denoted with t_i^- and t_i^+, respectively. It is supposed that interior point times t_i are considered unknowns of the problem, except for the initial time t_0 that is considered known. In general terms, the objective of a generic OCP with N phases is to find the state vector $\boldsymbol{x}(t)$, the controls $\boldsymbol{u}(t)$, and the time instants t_0, t_f, that minimize the performance index

$$J = \phi\left[\boldsymbol{x}(t_0^+), \boldsymbol{x}(t_1^-), \boldsymbol{x}(t_1^+), \ldots, \boldsymbol{x}(t_N^-); t_1, t_2, \ldots, t_N\right] + \sum_{i=1}^{N} \int_{t_{i-1}^+}^{t_i^-} L^{(i)}\left[\boldsymbol{x}(t), \boldsymbol{u}(t)\right] dt \tag{3.1}$$

subject to state equation constraints,

$$\dot{\boldsymbol{x}} = \boldsymbol{f}^{(i)}\left[\boldsymbol{x}(t), \boldsymbol{u}(t)\right]; \qquad t \in [t_{i-1}^+, t_i^-]; i = 1, \ldots, N \tag{3.2}$$

the path constraints

$$C_l \leq C[x(t), u(t)] \leq C_u, \tag{3.3}$$

and boundary conditions specified as

$$\psi\left[x(t_0^+), x(t_1^-), x(t_1^+), \ldots, x(t_N^-); t_1, t_2, \ldots, t_N\right] = 0 \tag{3.4}$$

The performance index $J : [t_0, t_f] \times \mathbb{R}^n \times \mathbb{R}^m \mapsto \mathbb{R}$ of Equation (3.1) is written in Bolza form, i.e., it is formed by the sum of the Lagrangian integral term $\int_{t_i^-}^{t_i^+} L^{(i)}[x(t), u(t), t] \, dt$, and a constant Mayer term ϕ which depends only on boundary values of state variables. It is assumed that functions $L : \mathbb{R}^n \times \mathbb{R}^m \mapsto \mathbb{R}$, and $\phi : [t_0, t_f] \times \mathbb{R}^n \mapsto \mathbb{R}$ are twice differentiable. The solution of the problem has to satisfy also path constraints given by the function $C : \mathbb{R}^n \times \mathbb{R}^m \mapsto \mathbb{R}^c$, with vectors of lower and upper bounds defined as $C_l \in \mathbb{R}^c$ and $C_u \in \mathbb{R}^c$, respectively. Finally, function $\psi : [t_0, t_f] \times \mathbb{R}^n \mapsto \mathbb{R}^q$ define q terminal conditions.

3.2   Direct Method

The basic idea behind direct methods is to realize a discretization of the system time history, and an approximation of system dynamics, state, and control vectors, using an accurate interpolation scheme (direct collocation method). According to this method, cost function, controls, and states can be expressed in terms of the values of the interpolant function at the interpolation nodes, also called the collocations points. System dynamics equations, often represented by Ordinary Differential Equations (ODEs), are approximated by quadrature rules, and enforced at the collocation points. Afterwards, the coefficients of the approximating functions become the optimization unknown of the problem, and the infinite dimensional OCP is transcribed into a NonLinear Programming (NLP) problem with a finite number of optimization variables.

3.2.1   Karush-Kuhn-Tucker Conditions

In order to detail the mathematical formulation of direct approach, the following constrained NLP is considered

$$\min_{\boldsymbol{x}} \quad J(\boldsymbol{x}) \tag{3.5}$$

$$\text{s.t.} \quad \boldsymbol{f}(\boldsymbol{x}) = 0 \tag{3.6}$$

$$\boldsymbol{C}(\boldsymbol{x}) \leq 0 \tag{3.7}$$

where $\boldsymbol{x} \in \mathbb{R}^n$ is the vector of optimization variables, $J : \mathbb{R}^n \mapsto \mathbb{R}$ the cost function which needs to be minimized, $\boldsymbol{f} : \mathbb{R}^n \mapsto \mathbb{R}^m$ the vector of equality constraints, and $\boldsymbol{C} : \mathbb{R}^n \mapsto \in \mathbb{R}^l$ the vector of inequality constraints. The classical approach to solve a constrained OCP of Equations (3.5) - (3.7), is to define the Lagrangian as

$$\mathscr{L}(\boldsymbol{x}, \boldsymbol{\lambda}, \boldsymbol{\nu}) = J(\boldsymbol{x}) + \boldsymbol{\lambda}^T \boldsymbol{f}(\boldsymbol{x}) + \boldsymbol{\mu}^T \boldsymbol{C}(\boldsymbol{x}) \tag{3.8}$$

where $\boldsymbol{\lambda} \in \mathbb{R}^m$ and $\boldsymbol{\mu} \in \mathbb{R}^l$ are the vectors of multipliers for equality and inequality constraints, respectively. First-order necessary conditions of optimality state that $(\boldsymbol{x}^*, \boldsymbol{\lambda}^*, \boldsymbol{\mu}^*)$ has to be a stationary point of $\mathscr{L}$, i.e.,

$$\nabla_{\boldsymbol{x}} \mathscr{L}(\boldsymbol{x}^*, \boldsymbol{\lambda}^*, \boldsymbol{\mu}^*) = \nabla_{\boldsymbol{x}} J(\boldsymbol{x}) + \boldsymbol{\lambda}^T \nabla_{\boldsymbol{x}} \boldsymbol{f}(\boldsymbol{x}) + \boldsymbol{\mu}^T \nabla_{\boldsymbol{x}} \boldsymbol{C}(\boldsymbol{x}) \quad = 0 \tag{3.9}$$

$$\nabla_{\boldsymbol{\lambda}} \mathscr{L}(\boldsymbol{x}^*, \boldsymbol{\lambda}^*, \boldsymbol{\mu}^*) = \boldsymbol{f}(\boldsymbol{x}) \quad = 0 \tag{3.10}$$

$$\nabla_{\boldsymbol{\mu}} \mathscr{L}(\boldsymbol{x}^*, \boldsymbol{\lambda}^*, \boldsymbol{\mu}^*) = \boldsymbol{C}(\boldsymbol{x}) \quad = 0 \tag{3.11}$$

Applying the Newton method to find $(\boldsymbol{x}^*, \boldsymbol{\lambda}^*, \boldsymbol{\mu}^*)$ which satisfy Equations (3.9) - (3.11), the following system of equation is obtained:

$$f_i(\boldsymbol{x}) = 0 \quad i = 1, ..., m \tag{3.12}$$

$$C_i(\boldsymbol{x}) = 0 \quad i = 1, ..., l \tag{3.13}$$

$$\mu_i \geq 0 \quad i = 1, ..., l \tag{3.14}$$

$$\mu_i C_i(\boldsymbol{x}) = 0 \quad i = 1, ..., l \tag{3.15}$$

$$\nabla_{\boldsymbol{x}} J(\boldsymbol{x}) + \sum_{i=1}^{m} \lambda_i \nabla_{\boldsymbol{x}} f_i(\boldsymbol{x}) + \sum_{i=1}^{l} \mu_i \nabla_{\boldsymbol{x}} C_i(\boldsymbol{x}) = 0 \tag{3.16}$$

The system of Equations (3.12) - (3.16) are the first-order conditions of optimality, also known as Karush-Kuhn-Tucker (KKT) conditions, and they express the necessary conditions that (x^*, λ^*, μ^*) have to meet in order to be an optimal solution of the problem. Often, necessary conditions are also sufficient to state the optimality of the solution, but as general approach, sufficient conditions of optimality should be calculated and they involve second derivatives of cost function and constraints. For a more comprehensive explanation, the reader is referred to [28].

3.2.2 Direct Collocation Schemes

Direct collocation methods can be distinguished by the interpolating function and the collocation points they use. The choice of the collocation points it is of primary importance. In facts, an arbitrary selection of the nodes may give very poor outcomes or it may produce the well-known Runge phenomenon at the extremes of interpolation. The collocation scheme dictates where more accuracy is desired or where discontinuity is allowed i.e., a uniform grid considers equally each time history segment, and conversely, a nonuniform node spacing creates a dense set of time step in a desired region. The interpolating functions used to approximate the solution over each time step are usually piecewise continuous polynomials, such as linear or cubic spline, or piecewise constant function [77, 78].

Other schemes, such as Hermite-Simpson collocation, use third-order Hermite interpolating polynomials enforced at the collocation points. The general formulation of this method is obtained using n-th order Hermite interpolating polynomials, and choosing the Legendre-Gauss-Lobatto points as collocation points. These types of collocation schemes are called Hermite-Legendre-Gauss-Lobatto (HLGL) collocation methods [79]. Under specific discretization nodes, the expression for the collocation constraint corresponds to the Simpson integration rule. Gauss or Radau collocation schemes [80, 79] are other examples of collocation schemes. Notwithstanding, the choice of interpolant functions and collocation points it is not limited to these cases.

For the expansion of state and control variables also orthogonal polynomials such as Legendre, Chebyshev, or Lagrange polynomials may be used [81]. If Chebyshev polynomials are adopted for OCP solution, an orthogonal polynomials expansion with unknown generalized Fourier coefficients is used to approximate both the

state and control variables. When the approximating functions space is spanned by orthogonal polynomials, the direct methods are named pseudospectral methods. The reader is referred to [82] for a more comprehensive analysis of direct collocations schemes available for the solution of OCPs. For sake of simplicity, basic collocation schemes are illustrated in this section, giving an overall idea of the working principle of such method.

Basic HLGL Collocation Schemes

According to HLGL direct methods, the time domain of the OCP is split into N subintervals between endpoints t_0 and t_f as

$$t_0 < t_1 < t_2 < ... < t_{N-1} < t_N = t_f \tag{3.17}$$

and each subinterval is spanned by an integration step

$$h_i = (t_{i+1} - t_i) \quad i = 0,...,N \tag{3.18}$$

As a result, controls and states values at the collocation points t_i are denoted by u_i and x_i, respectively. OCPs usually includes system dynamics equations represented by ODEs of the form.

$$\dot{x} = f(x(t), u(t)) \tag{3.19}$$

where x and u are the state and control vectors, respectively. Direct approach approximates ODEs via quadrature rules, and transcribes them into algebraic equality constraints as those in Equation (3.7). These constraints are called defect constraints.

Considering simple *trapezoidal* rule, where the integrand is approximated with a linear function between nodes, and an ODE of the form $\dot{x} = f(x)$, the following defect constraints are derived

$$x(t_{i+1}) - x(t_i) = \int_{t_i}^{t_{i+1}} f(x(t), u(t)) \, dt \approx \frac{h_i}{2} \left[f(x_i) + f(x_{i+1}) \right] \quad i = 0,...,N \tag{3.20}$$

If *Simpson's* rule is used for an ODE of the form $\dot{\boldsymbol{x}} = f(\boldsymbol{x})$, the integrand is approximated by a quadratic polynomial, and the defect constraints in this case are

$$\boldsymbol{x}(t_{i+1}) - \boldsymbol{x}(t_i) = \int_{t_i}^{t_{i+1}} \boldsymbol{f}(\boldsymbol{x}(t), \boldsymbol{u}(t))\, dt \approx \frac{h_i}{6} \left[\boldsymbol{f}(\boldsymbol{x}_i) + 4\boldsymbol{f}(\boldsymbol{x}_{i,C}) + \boldsymbol{f}(\boldsymbol{x}_{i+1}) \right] \quad i = 0, ..., N$$

(3.21)

where $\boldsymbol{x}_{i,C}$ defined as

$$\boldsymbol{x}_{i,C} = \frac{1}{2}(\boldsymbol{x}_{i+1} + \boldsymbol{x}_i) + \frac{h_i}{8} \left[\boldsymbol{f}(\boldsymbol{x}_i) + \boldsymbol{f}(\boldsymbol{x}_{i+1}) \right] \quad i = 1, ..., N \qquad (3.22)$$

is the approximated value of $\boldsymbol{x}(t)$ at the internal collocation point (midpoint) $t_{i,C} = (t_{i+1} + t_i)/2$.

In both trapezoidal and Simpson's rule the degree of the integrand polynomial is equal to the number of the collocation points. In facts, the trapezoid rule is the second-degree rule and it interpolates the integrand between two collocation points, whereas Simpson's rule uses a third-degree interpolant on three collocation points.

Omitting a deep discussion about truncation error in numerical integration, in general terms it is possible to assert that the accuracy of a numerical method to approximate integrals increases with the number of subintervals. Nonetheless, the higher the number of collocations points, the higher the number of optimization variables of the problem, resulting in a burdensome optimization problem. The order of accuracy is the most important measure, the greater is the order of accuracy, the greater is the reduction in error for smaller step size. Finally, in order to achieve a specified accuracy, an appropriate trade-off has to be found by combining properly number of collocation points and integration rule. When quadrature rules are used, particular attention has to be given when the interpolant is of degree higher than two. Indeed, the position of the collocation points has a strong impact on the discretization error.

Higher order quadrature rules can be also used, such as, the fifth-degree Gauss-Lobatto. Figure (3.1) shows a representation of fifth-degree Gauss-Lobatto integration scheme. This method relies on an fifth-degree Jacobi polynomial interpolant, and the defect constraints are written for the two internal collocation points $t_{i,a} = t_{i,C} - \sqrt{\frac{3}{7}}\frac{h_i}{2}$ and $t_{i,b} = t_{i,C} + \sqrt{\frac{3}{7}}\frac{h_i}{2}$. The approximated values of the states at the internal collocations points become

$$x_{i,a} = \frac{1}{686} \Big\{ (39\sqrt{21} + 231)x_i + 224x_{i,C} +$$
$$(-39\sqrt{21} + 231)x_{i+1} + h_i \Big[(3\sqrt{21} + 21)f(x_i) - 16\sqrt{21}f(x_{i,C}) + \quad (3.23)$$
$$\{ (3\sqrt{21} - 21)f(x_{i+1})] \Big\}$$

$$x_{i,b} = \frac{1}{686} \Big\{ (-39\sqrt{21} + 231)x_i + 224x_{i,C} +$$
$$(+39\sqrt{21} + 231)x_{i+1} + h_i \Big[(-3\sqrt{21} + 21)f(x_i) + 16\sqrt{21}f(x_{i,C}) + \quad (3.24)$$
$$\{ (-3\sqrt{21} - 21)f(x_{i+1})] \Big\}$$
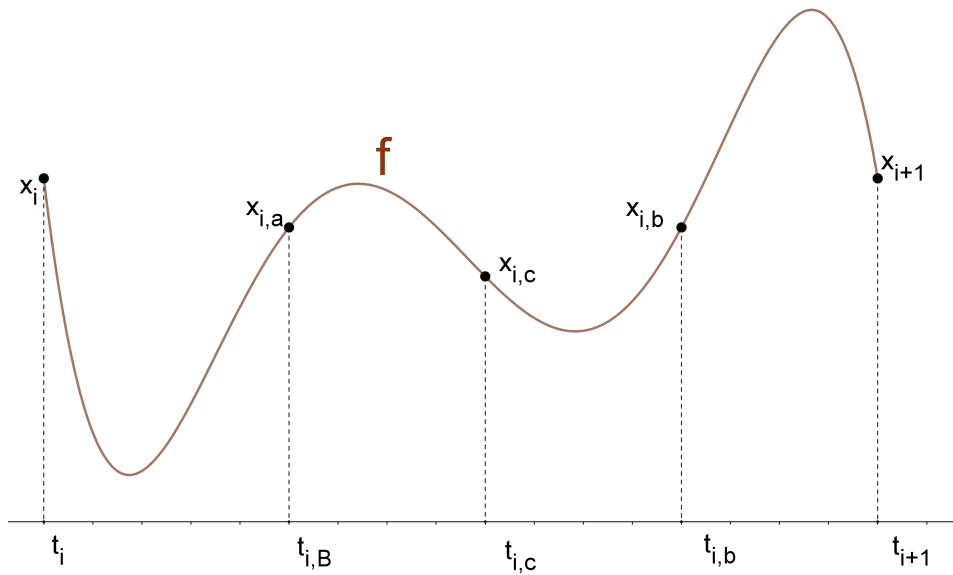
Figure 3.1: Fifth-degree Gauss-Lobatto interpolation scheme.

Beside state variables collocation schemes, also control variables need to be discretized. In order to determine the value of controls at internal collocation points, i.e., $u_{i,C}$, different collocation schemes are used in direct approach. In Simpson's rule, as an example, linear scheme approximates controls as $u_{i,C} = \frac{(u_{i,a} + u_{i,b})}{2}$, cubic scheme uses an Hermite third-degree polynomial, and free control scheme includes $u_{i,C}$ as unknown control parameters of the problem. In high-order interpolation schemes, usually free control interpolation scheme is used.

3.3   Indirect Method - Unconstrained Case

For the solution of the obstacle avoidance OCP, the indirect method approach is employed. The indirect method determines the first-order optimality conditions needed for the solution of the optimal control problem given in Equations (3.1)-(3.4). The first-order necessary conditions derived from calculus of variations, are typically derived defining the augmented Hamiltonian function $H : [t_0, t_f] \times \mathbb{R}^n \times \mathbb{R}^n \times \mathbb{R}^m \mapsto \mathbb{R}$. Lagrange multipliers (or costates) $\boldsymbol{\lambda}(t) \in \mathbb{R}^n$, and discrete Lagrange multipliers $\boldsymbol{\nu} \in \mathbb{R}^q$ are also introduced. Considering a generic unconstrained problem, Hamiltonian function H is defined as

$$H^{(i)}(\boldsymbol{x}, \boldsymbol{\lambda}, \boldsymbol{u}, t) = L^{(i)} + \boldsymbol{\lambda}^T \boldsymbol{f}^{(i)} \tag{3.25}$$

Introducing the constant part of the augmented performance index as

$$\Phi = \phi + \boldsymbol{\nu}^T \psi \tag{3.26}$$

where definitions of ϕ and ψ are the same of Section 3.1, the augmented cost function J_a becomes

$$J_a = \Phi + \sum_{i=1}^{N} \int_{t_{i-1}^+}^{t_i^-} \left(H^{(i)} - \boldsymbol{\lambda}^T \dot{\boldsymbol{x}} \right) dt \tag{3.27}$$

In order to obtain the necessary optimality conditions of the OCP solution, Equation (3.27) is expanded in Taylor series about the optimal solution, and the first variation δJ_a is obtained. Since the optimal solution variations are such small that the sign of the first increment δJ_a can be considered equal to the sign of the cost function increment J_a, in [83] is proven that the necessary conditions of optimality correspond

to a stationary point of J_a. As done in [35], the first variation of J_a is:

$$
\begin{aligned}
\delta J_a = \sum_{i=1}^{N} \int_{t_{i-1}^{+}}^{t_i^{-}} & \left[\delta \boldsymbol{\lambda}^T \left(\boldsymbol{f}^{(i)} - \dot{\boldsymbol{x}} \right) + \delta \boldsymbol{x}^T \left(\frac{\partial H^{(i)}}{\partial \boldsymbol{x}} \right)^T - \delta \dot{\boldsymbol{x}}^T \boldsymbol{\lambda} \right. \\
& \left. + \delta \boldsymbol{u}^T \left(\frac{\partial H^{(i)}}{\partial \boldsymbol{u}} \right)^T \right] dt + d\boldsymbol{\nu}^T \psi \\
& + \sum_{i=1}^{N-1} \left[\frac{\partial \Phi}{\partial t_i} + L^{(i)}(t_i^-) - L^{(i+1)}(t_i^+) \right] dt_i + \left[\frac{\partial \Phi}{\partial t_N} + L^{(N)}(t_N^-) \right] dt_N \\
& + \sum_{i=1}^{N} \left[\frac{\partial \Phi}{\partial \boldsymbol{x}(t_i^-)} \right] d\boldsymbol{x}(t_i^-) + \sum_{i=0}^{N-1} \left[\frac{\partial \Phi}{\partial \boldsymbol{x}(t_i^+)} \right] d\boldsymbol{x}(t_i^+)
\end{aligned}
\tag{3.28}
$$

By defining $\delta \boldsymbol{x}(t)$ as the perturbation of $\boldsymbol{x}$ while t is maintained fixed, and $d\boldsymbol{x}(t_i^+)$, $d\boldsymbol{x}(t_i^-)$ as the perturbation of $\boldsymbol{x}$ due to t at the event times t_i^+, t_i^-, respectively, the following relations are obtained

$$
d\boldsymbol{x}(t_i^+) = \delta \boldsymbol{x}(t_i^+) + \dot{\boldsymbol{x}}(t_i^+) dt_i \tag{3.29}
$$

$$
d\boldsymbol{x}(t_i^-) = \delta \boldsymbol{x}(t_i^-) + \dot{\boldsymbol{x}}(t_i^-) dt_i \tag{3.30}
$$

By integrating $\delta \dot{\boldsymbol{x}}^T \boldsymbol{\lambda}$ by parts, and substituting Eqs.(3.29)-(3.30) into Equation (3.28), the following expression is obtained

$$
\begin{aligned}
\delta J_a = \sum_{i=1}^{N} \int_{t_{i-1}^{+}}^{t_i^{-}} & \left\{ \delta \boldsymbol{\lambda}^T \left(\boldsymbol{f}^{(i)} - \dot{\boldsymbol{x}} \right) + \delta \boldsymbol{x}^T \left[\left(\frac{\partial H^{(i)}}{\partial \boldsymbol{x}} \right)^T + \dot{\boldsymbol{\lambda}} \right] \right. \\
& \left. + \delta \boldsymbol{u}^T \left(\frac{\partial H^{(i)}}{\partial \boldsymbol{u}} \right)^T \right\} dt + d\boldsymbol{\nu}^T \psi \\
& + \sum_{i=1}^{N-1} \left[\frac{\partial \Phi}{\partial t_i} + H^{(i)}(t_i^-) - H^{(i+1)}(t_i^+) \right] dt_i + \left[\frac{\partial \Phi}{\partial t_N} + H^{(N)}(t_N^-) \right] dt_N \\
& + \sum_{i=1}^{N} \left[\frac{\partial \Phi}{\partial \boldsymbol{x}(t_i^-)} - \boldsymbol{\lambda}^T(t_i^-) \right] d\boldsymbol{x}(t_i^-) + \sum_{i=0}^{N-1} \left[\frac{\partial \Phi}{\partial \boldsymbol{x}(t_i^+)} + \boldsymbol{\lambda}^T(t_i^+) \right] d\boldsymbol{x}(t_i^+)
\end{aligned}
\tag{3.31}
$$

As a result of setting δJ_a to zero, the following Euler-Lagrange equations are obtained,

$$\dot{x} - f^{(i)} = 0 \tag{3.32}$$

$$\dot{\lambda} + \left(\frac{\partial H^{(i)}}{\partial x} \right)^T = 0 \tag{3.33}$$

$$\frac{\partial H^{(i)}}{\partial u} = 0 \tag{3.34}$$

and the boundary conditions for optimality become

$$\frac{\partial \Phi}{\partial t_i} + H^{(i)}(t_i^-) - H^{(i+1)}(t_i^+) = 0 \qquad (i = 1, 2, \dots, N-1) \tag{3.35}$$

$$\frac{\partial \Phi}{\partial t_N} + H^{(N)}(t_N^-) = 0 \tag{3.36}$$

$$\psi \left[x(t_0^+), x(t_1^-), x(t_1^+), \dots, x(t_N^-); t_1, \dots, t_N \right] = 0 \tag{3.37}$$

$$\frac{\partial \Phi}{\partial x(t_i^-)} - \lambda^T(t_i^-) = 0 \qquad (i = 1, 2, \dots, N) \tag{3.38}$$

$$\frac{\partial \Phi}{\partial x(t_i^+)} + \lambda^T(t_i^+) = 0 \qquad (i = 0, 1, \dots, N-1) \tag{3.39}$$

Equations (3.32)-(3.39) define a multi-point boundary problem which solution satisfies the *necessary* conditions of optimality. When neither f nor L are explicit functions of time, the Hamiltonian function H is constant along the optimal trajectory. In facts, the total time derivative of H is

$$\begin{aligned} \dot{H} &= \frac{\partial H}{\partial t} + \frac{\partial H}{\partial x} \dot{x} + \frac{\partial H}{\partial u} \dot{u} + \dot{\lambda}^T f \\ &= \frac{\partial H}{\partial t} + \frac{\partial H}{\partial u} \dot{u} + \left(\frac{\partial H}{\partial x} + \dot{\lambda}^T \right) f \end{aligned} \tag{3.40}$$

If the OCP is solved by the control u, therefore Eqs. (3.33)-(3.34) are true, and Equation 3.40 becomes,

$$\dot{H} = \frac{\partial H}{\partial t} \tag{3.41}$$

and if L and $\boldsymbol{f}$ are not explicitly time dependent, the following result is obtained

$$\dot{H} = 0 \tag{3.42}$$

proving that H is constant along an optimal path.

The first order conditions guarantee that the cost function has a stationary point in correspondence of the control that solves the problem. This is a necessary condition, but not sufficient to assert that J_a has a local minimum (maximum). In order to find the local minimum (maximum), the second order expansion of δJ_a has to be nonnegative (nonpositive) about the solution point. That is

$$\delta J_a = \frac{1}{2} \left[\delta \boldsymbol{x}^T \frac{\partial^2 \Phi}{\partial \boldsymbol{x}^2} \delta \boldsymbol{x} \right]_{t=t_f} + \frac{1}{2} \int_{t_0}^{t_f} [\delta \boldsymbol{x}^T \, \delta \boldsymbol{u}^T] \begin{bmatrix} \frac{\partial^2 H}{\partial \boldsymbol{x}^2} & \frac{\partial^2 H}{\partial \boldsymbol{x} \partial \boldsymbol{u}} \\ \frac{\partial^2 H}{\partial \boldsymbol{u} \partial \boldsymbol{x}} & \frac{\partial^2 H}{\partial \boldsymbol{u}^2} \end{bmatrix} \begin{bmatrix} \delta \boldsymbol{x} \\ \delta \boldsymbol{u} \end{bmatrix} dt \geq 0 (\leq 0) \tag{3.43}$$

For the sake of giving an example of the application of such method, Appendix A presents the result of a stochastic unconstrained OCP solved via indirect method.

3.4 Indirect Method - State Constraints

In the formulation presented so far, a generic unconstrained OCP has been considered. When indirect methods are employed for the solution of OCPs in presence of path constraints, finding correct trajectory structures is not a trivial task for the analyst, and in general, it is often achieved by trial-and-error. As showed in [84], the structure of OCP solution bounded by state constraints depends on the order of such constraint. The constraint order is defined as the number of total time derivatives that have to be taken, until an explicit dependence on the control $\boldsymbol{u}$ appears in the constraint expression. For scalar state constraints of odd-order greater than two, only touch point solutions are possible [85], i.e., the trajectory touches the constraint boundary only at one discrete time instant. For first-order constraints instead, only boundary-arcs are expected, i.e., the solution has a constrained arc that links together two unconstrained arcs.

The case where there exists a scalar state constraint of the form

$$S(\boldsymbol{x},t) \leq 0 \qquad t \in [t_0, t_f] \tag{3.44}$$

is now considered. Without loss of generality, it is assumed that the solution of constrained problem has one unconstrained arc (inactive constraint, i.e. $S < 0$) between t_0 and t_1, one constrained arc (active constraint, i.e. $S = 0$) between t_1 and t_2, and finally another unconstrained arc between t_2 and t_f with $t_0 < t_1 < t_2 < t_f$. As done in [86], successive total time derivatives of Eq. (3.44) are taken, until an expression explicitly dependent on the controls u is obtained. If p-total time derivatives are needed, the Hamiltonian in Eq. (3.25) is then modified to include $S^{(p)}$ as

$$H(\boldsymbol{x}, \boldsymbol{\lambda}, \mu, \boldsymbol{u}, t) = L + \boldsymbol{\lambda}^T \boldsymbol{f} + \mu S^{(p)} \tag{3.45}$$

where μ is a scalar function such that

$$\mu = \begin{cases} > 0, & S(\boldsymbol{x},t) = 0 \\ = 0, & S(\boldsymbol{x},t) < 0 \end{cases} \tag{3.46}$$

and the condition

$$S(\boldsymbol{x},t)^{(p)} = \frac{\mathrm{d}^{(p)}S}{\mathrm{d}t^p} = 0 \qquad t \in [t_1, t_2] \tag{3.47}$$

has to be satisfied during the constrained arc, i.e., between t_1 and t_2. Obviously, since S has been substituted with its p-time derivative $S^{(p)}$, the path entering and leaving the constraint boundary has to meet p tangency conditions (interior point constraints) defined as

$$N(\boldsymbol{x},t) \triangleq \begin{bmatrix} S(\boldsymbol{x},t) \\ S(\boldsymbol{x},t)^{(1)} \\ \vdots \\ S(\boldsymbol{x},t)^{(p-1)} \end{bmatrix} = 0 \tag{3.48}$$

One can arbitrary choose the entry point instead of the exit point as the place where these conditions have to be satisfied. As a consequence, the solution at the exit point will automatically satisfy the tangency condition. Eq. (3.48) forms a set of interior point constraints that, as it has been demonstrated in [35], entail some discontinuities in the costates $\boldsymbol{\lambda}$ at the junction points between constrained and unconstrained arc. On the other hand, state variables continuity has to be imposed at the entry and exit

point as

$$
\begin{aligned}
\boldsymbol{x}(t_1^-) - \boldsymbol{x}(t_1^+) &= 0 \\
\boldsymbol{x}(t_2^-) - \boldsymbol{x}(t_2^+) &= 0
\end{aligned}
\tag{3.49}
$$

The tangency and state continuity conditions expressed by Eq. (3.48) and Eq. (3.49), respectively, are therefore enforced by inserting them into the vector of boundary conditions $\boldsymbol{\psi}$ of Eq. (3.4). Equations (3.32) - (3.39), applied now to the new augmented Hamiltonian of Eq. (3.45), and conditions on $\boldsymbol{\mu}$ of Eq. (3.46), form a MPBVP which solution satisfies the necessary conditions of optimality of the constrained OCP. In particular, considering only t_0 and t_f, the optimality conditions of Equations (3.34) and (3.47) determine the $m+1$ quantities $\boldsymbol{u}$ and $\boldsymbol{\mu}$. The solution of the $2n$ differential equations (3.32) and (3.33), together with choice of the $q+1$ parameters $\boldsymbol{\nu}$ and t_f, are determined by the $2n+q+1$ boundary conditions of Equations (3.36)-(3.39). Regarding the internal point constraints, Equations (3.38) introduce a p-component vector of constant Lagrange multipliers that have to satisfy the p conditions of Eq. (3.48).

Chapter 4

OCP with Stochastic Path Constraint - Problem Modeling and Solution Approach

4.1 Vehicle-Obstacle Encountering Scenario

In this section, a 2-Dimensional (2D) portion of airspace is considered within which the planned trajectory of an aircraft collides with a fixed obstacle. It is also supposed that the initial and final waypoints of the planned trajectory, referred to as $O(x_O, y_O)$ and $F(x_F, y_F)$, respectively, are known, and they coincide with the initial and final position of the aircraft, respectively. The initial time t_0 is also supposed known, whereas the final time t_f is a control parameter of the problem to be found in addition to the control $\boldsymbol{u}$. The shape of the obstacle is supposed to be circular with its center in $\boldsymbol{x}_C(x_C, y_C)$ and radius Γ. Finally, the points $A(x_A, y_A)$ and $B(x_B, y_B)$ are defined as the intersection points (i.e, collision points) between the straight route $\overline{OF}$ and the obstacle boundary. A schematic of the aircraft-obstacle configuration is shown in Fig. 4.1.
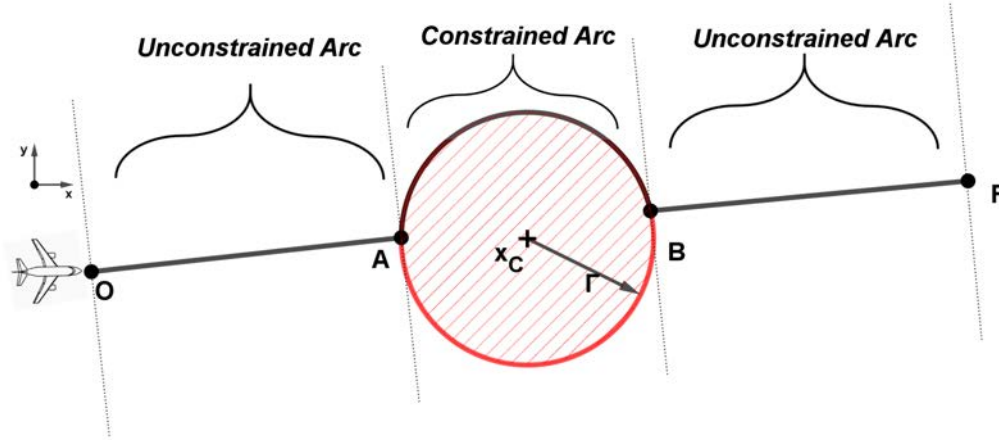
Figure 4.1: Schematic configuration of aircraft and fixed obstacle.

4.2 States and Control Variables

Under the assumption of heading angle control only, the vector of state variables $\boldsymbol{x}(t)$, and the vector of controls $\boldsymbol{u}(t)$ are introduced as

$$\boldsymbol{x}(t) = \begin{bmatrix} x(t) \\ y(t) \end{bmatrix} \tag{4.1}$$

$$\boldsymbol{u}(t) = \chi(t) \tag{4.2}$$

where $x(t)$, $y(t)$ are the Cartesian coordinates of the aircraft, and $\chi \in [-\pi, \pi]$ is the aircraft heading angle. For simplicity, aircraft equations of motion are expressed as pure kinematics equations, i.e.

$$\boldsymbol{f}[\boldsymbol{x}(t), \boldsymbol{u}(t)] = \dot{\boldsymbol{x}}(t) = \begin{bmatrix} V \cos \chi(t) \\ V \sin \chi(t) \end{bmatrix} \tag{4.3}$$

where aircraft true airspeed V is assumed to be constant.

4.3   Obstacle Constraint

Obstacle conflict is defined as the violation of the obstacle boundary, or in other terms, a conflict occurs if the position of the aircraft is within the circle representing the obstacle. In mathematical terms, no conflicts occur as long as

$$C(\boldsymbol{x}) = 1 - \sqrt{\frac{(x-x_C)^2}{\Gamma^2} + \frac{(y-y_C)^2}{\Gamma^2}} \leq 0 \qquad t \in [t_0, t_f] \qquad (4.4)$$

where $x(t)$, $y(t)$ are the 2-dimensional coordinates of the aircraft. It is supposed that the position of the obstacle center is provided by an on-board sensing platform affected by measurement errors, whereas the obstacle shape is known. As a consequence, the coordinates of the obstacle $C(x_C, y_C)$ are supposed to be affected by uncertainty, and they are characterized by a Gaussian normal Probability Density Function (PDF) of the form

$$p_{\mathbf{X}_C}(x_C, y_C) = \frac{1}{2\pi\sigma_{x_C}\sigma_{y_C}} \exp\left(-\frac{(x_C - \mu_{x_C})^2}{2\sigma_{x_C}^2} - \frac{(y_C - \mu_{y_C})^2}{2\sigma_{y_C}^2}\right) \qquad (4.5)$$

or, in symbols, $\mathbf{X}_C \sim \mathcal{N}(\boldsymbol{\mu}, \boldsymbol{\Sigma})$, where $\boldsymbol{\mu} = (\mu_{x_C}, \mu_{y_C})$ is the expected sensed value, and $\boldsymbol{\Sigma}$ is a diagonal covariance matrix defined by the standard deviations σ_{x_C} and σ_{y_C}. One point of strength of this modeling is that obstacle do not necessary represent a physical obstacle, so it could be employed to model a storm, another aircraft, or other types of obstacles in the airspace characterized by constant relative velocity with respect to the own aircraft.

4.4   Deriving Optimality Boundary Conditions by Indirect Method

Considering the Fig. 4.1, it is supposed that trajectory can be divided in three phases: one unconstrained arc ($C < 0$) from initial point to the obstacle boundary, referred to as $\overline{0A}$, followed by one constrained arc ($C = 0$) along the obstacle boundary identified as $\overline{AB}$, and eventually another unconstrained arc from the obstacle boundary to the final waypoint, referred to as $\overline{BF}$.

According to the indirect method explained in Section 3.3, Equation (3.1) is used to define the performance index J as

$$J = \int_{t_0^+}^{t_f^-} dt \; . \tag{4.6}$$

For the unconstrained arc, i.e., when $C < 0$ and $\mu = 0$, the Euler-Lagrange Equations (3.32)-(3.34) become

$$\dot{\boldsymbol{x}} = \boldsymbol{f} \tag{4.7}$$

$$\dot{\boldsymbol{\lambda}} = 0 \tag{4.8}$$

with the algebraic equation

$$\boldsymbol{\lambda}^T \frac{\partial \boldsymbol{f}}{\partial \boldsymbol{u}} = 0 \tag{4.9}$$

and boundary conditions

$$\boldsymbol{x}(t_0) = O(x_O, y_O) \tag{4.10}$$

$$\boldsymbol{x}(t_f) = F(x_f, y_f) \tag{4.11}$$

$$\boldsymbol{\lambda}(t_0) = \boldsymbol{\nu}_0 \tag{4.12}$$

$$\boldsymbol{\lambda}(t_f) = \boldsymbol{\nu}_f \tag{4.13}$$

$$H(t_f) = 0 \tag{4.14}$$

where $\boldsymbol{\nu}_0 \in \mathbb{R}^2$ and $\boldsymbol{\nu}_f \in \mathbb{R}^2$ are two vectors of constant control parameters. Equation (4.8) shows that costates are constant along unconstrained arcs, therefore heading angle optimal controls are also constants. As a result, unconstrained trajectories results in two simple straight lines between waypoints and obstacle collision points.

For the constrained arc, i.e, when $C = 0$ and $\mu \neq 0$, Equation (3.45) is used to define the Hamiltonian as

$$H = 1 + \boldsymbol{\lambda}^T \boldsymbol{f} + \mu C^{(p)} \; . \tag{4.15}$$

Since C represents an inequality constraint on function of state variables only, total p time derivatives of C are taken until an explicit dependence on controls χ appears.

Therefore, taking the first total time derivative of C

$$\dot{C} = \frac{\mathrm{d}C}{\mathrm{d}t} = \frac{\partial C}{\partial t} + \frac{\partial C}{\partial x}\frac{\partial x}{\partial t} + \frac{\partial C}{\partial y}\frac{\partial y}{\partial t} \tag{4.16}$$

$$= 0 - \frac{(x-x_C)/\Gamma^2}{\sqrt{\frac{(x-x_C)^2}{\Gamma^2} + \frac{(y-y_C)^2}{\Gamma^2}}}V\cos\chi - \frac{(y-y_C)/\Gamma^2}{\sqrt{\frac{(x-x_C)^2}{\Gamma^2} + \frac{(y-y_C)^2}{\Gamma^2}}}V\sin\chi \tag{4.17}$$

and by using the relation $C = 0$ the following expression is obtained

$$\dot{C} = -\frac{V}{\Gamma^2}\left((x-x_C)\cos\chi + (y-y_C)\sin\chi\right) \tag{4.18}$$

Equation (4.18) shows that explicit dependence on controls appears in the first derivative, therefore, it is proved that the constraint order is one, and the structure of the trajectory is formed by two unconstrained arcs, linked together by a constrained arc. Since the order of the constraint is one, the Hamiltonian becomes

$$H = 1 + \boldsymbol{\lambda}^T \boldsymbol{f} + \mu\dot{C} \tag{4.19}$$

and the interior point constraint N is defined as

$$N(\boldsymbol{x}) = C(\boldsymbol{x}) = 1 - \sqrt{\frac{(x-x_C)^2}{\Gamma^2} + \frac{(y-y_C)^2}{\Gamma^2}} = 0 \tag{4.20}$$

Without loss of generality, is assumed that Equation (4.20) has to be satisfied at the exit point of the constrained arc, i.e., $C(\boldsymbol{x}(t_B^-)) = C(\boldsymbol{x}(t_B^+))$. Under these conditions the Euler-Lagrange equations (3.32)-(3.34) become

$$\dot{\boldsymbol{x}} = \boldsymbol{f} \tag{4.21}$$

$$\dot{\boldsymbol{\lambda}} = -\mu\frac{\partial\dot{C}}{\partial\boldsymbol{x}} \tag{4.22}$$

subject to the algebraic equations

$$\dot{C} = 0 \tag{4.23}$$

$$\boldsymbol{\lambda}^T\frac{\partial\boldsymbol{f}}{\partial\boldsymbol{u}} + \mu\frac{\partial\dot{C}}{\partial\boldsymbol{u}} = 0 \tag{4.24}$$

and boundary conditions

$$\boldsymbol{x}(t_{A+}) = \boldsymbol{x}(t_{A-}) \tag{4.25}$$

$$\boldsymbol{x}(t_{B+}) = \boldsymbol{x}(t_{B-}) \tag{4.26}$$

$$C(\boldsymbol{x}(t_{A+})) = 0 \tag{4.27}$$

$$C(\boldsymbol{x}(t_{B-})) = 0 \tag{4.28}$$

$$\boldsymbol{\lambda}(t_{A+}) = \boldsymbol{\lambda}(t_{A-}) \tag{4.29}$$

$$\boldsymbol{\lambda}(t_{B+}) = \boldsymbol{\lambda}(t_{B-}) + \pi \left.\frac{\partial N}{\partial \boldsymbol{x}}\right|_{\boldsymbol{x}(t_{B+})} \tag{4.30}$$

$$H(t_{A+}) = H(t_{A-}) \tag{4.31}$$

$$H(t_{B+}) = H(t_{B-}) \tag{4.32}$$

where π is a constant non-zero scalar.

As previously stated in Section 3.4, Equation (4.30) proves that the presence of time invariant state constraint in the problem entails discontinuity in costates. Indeed, the vector

$$\left.\frac{\partial N}{\partial \boldsymbol{x}}\right|_{\boldsymbol{x}(t_{B+})} = -\frac{(\boldsymbol{x}(t_B) - \boldsymbol{x}_C)}{\Gamma^2} \tag{4.33}$$

is in general not zero, generating a jump in costates at the collision point B. A specular result would have been obtained if the interior point constraint of Equation (4.20) would have been set at A. In that case, the jump would appear at collision point A.

Heading angles during unconstrained arcs were proved to be constant, therefore the resulting trajectories are straight lines. As for constrained arc, Equation (4.22) is an Ordinary Differential Equation (ODE) which solution is in general not trivial. Since during optimal constrained arc both relations $C = 0$ and $\dot{C} = 0$ are true, the resulting trajectories are circular args tangent to the constraint boundary.

In order to better observe the trend of controls at junction points, some considerations need to be done. For convenience, the following notation for aircraft speed is introduced

$$\boldsymbol{V} = \begin{bmatrix} V\cos\chi(t) \\ V\sin\chi(t) \end{bmatrix} \tag{4.34}$$

and the time dependence notation is dropped for all quantities, e.g., $\boldsymbol{V}(t_A^+)$ or $\boldsymbol{\lambda}(t_B^-)$ is dropped for $\boldsymbol{V}_A^+$ and $\boldsymbol{\lambda}_B^-$. Concerning the junction point A, the Hamiltonian continuity of Equation (4.31) becomes

$$1 + \boldsymbol{\lambda}_A^+ \cdot \boldsymbol{V}_A^+ + \mu_A^+ \dot{C}_A^+ = 1 + \boldsymbol{\lambda}_A^- \cdot \boldsymbol{V}_A^- \tag{4.35}$$

$\dot{C}_{A+} = 0$ is true during constrained arc, and the costates continuity of Equation (4.29) into Equation (4.35) leads to the following result

$$\boldsymbol{\lambda}_A^+ \cdot (\boldsymbol{V}_A^+ - \boldsymbol{V}_A^-) = 0 \tag{4.36}$$

Equation (4.36) is true when, for non-zero multipliers, the vector $\boldsymbol{V}_A^+$ is equal to $\boldsymbol{V}_A^-$. Since they have same magnitude (constant speed scenario), the two vectors are equal if and only if they have same direction, i.e. heading angle χ. Therefore, at the junction point A the optimal control χ is continuous.

Similar considerations can be done for the junction point B. Indeed, the discontinuity in the costate expressed by Equation (4.30) can be written as

$$\boldsymbol{\lambda}_B^+ = \boldsymbol{\lambda}_B^- + \pi \left.\frac{\partial N}{\partial \boldsymbol{x}}\right|_{\boldsymbol{x}_B} = \boldsymbol{\lambda}_B^- - \pi \frac{(\boldsymbol{x}_B - \boldsymbol{x}_C)}{\Gamma^2} \tag{4.37}$$

Multiplying each term of Equation (4.37) by the speed vector $\boldsymbol{V}_B^-$

$$\boldsymbol{\lambda}_B^+ \cdot \boldsymbol{V}_B^- = \boldsymbol{\lambda}_B^- \cdot \boldsymbol{V}_B^- - \frac{\pi}{\Gamma^2}(\boldsymbol{x}_B - \boldsymbol{x}_C) \cdot \boldsymbol{V}_B^- \tag{4.38}$$

Since during constrained arc the speed vector is tangent to the constraint boundary, and it is also perpendicular to the radius vector $(\boldsymbol{x}_B - \boldsymbol{x}_C)$ at the junction point B, the right-hand side of Equation (4.38) becomes

$$\boldsymbol{\lambda}_B^+ \cdot \boldsymbol{V}_B^- = \boldsymbol{\lambda}_B^- \cdot \boldsymbol{V}_B^- \tag{4.39}$$

Recalling Hamiltonian continuity at t_B of Equation (4.32)

$$\boldsymbol{\lambda}_B^+ \cdot \boldsymbol{V}_B^+ = \boldsymbol{\lambda}_B^- \cdot \boldsymbol{V}_B^- \tag{4.40}$$

and subtracting Equations (4.39) and (4.40) the following relation is obtained

$$\boldsymbol{\lambda}_B^+ \cdot (\boldsymbol{V}_B^- - \boldsymbol{V}_B^+) = 0 \tag{4.41}$$

Equation (4.41) is true when, for non-zero multipliers, the vector $\boldsymbol{V}_B^-$ is equal to $\boldsymbol{V}_B^+$. Since they have same magnitude (constant speed scenario), the two vectors are equal if and only if they have same direction, i.e. heading angle χ. Therefore, at the junction point B the optimal control is continuous. In the view of the foregoing, it is reasonable to assume that the shape of the optimal trajectory is composed by two straight lines tangent to the constraint boundary (unconstrained arcs), linked together by a circular arc (constrained arc). Figure 4.2 represent an exemplifying shape of the optimal solution.
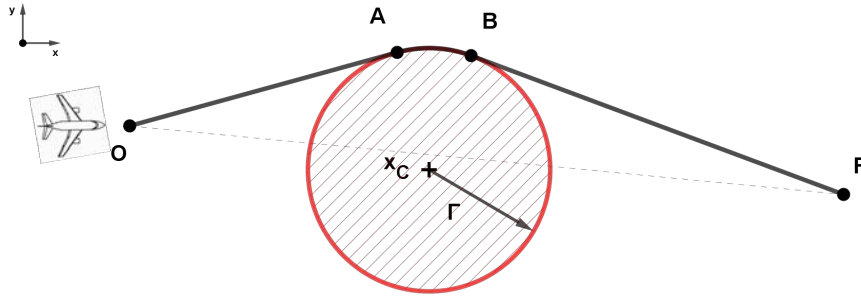
Figure 4.2: Example of conflict-free optimal trajectory.

Equations (4.7)-(4.14), together with Equations (4.21)-(4.32), form the MPBVP that has be solved to find the optimal solution of the CD&R formulated as OCP. To completely solve the problem, the optimal control parameters that have to be found are: the constant heading angles χ_{0A} and χ_{BF} during the constrained arcs $\overline{0A}$ and $\overline{BF}$, respectively, and the final time t_f. Firstly, a trial shooting algorithm has been run, and it has been observed that the two controls χ_{0A} and χ_{BF} can be obtained by satisfying two conditions: the "jump" on the costates at t_B defined by Equation (4.30), and the continuity of the Hamiltonian function at t_A expressed by Equation (4.31).

4.5 Differential Algebra for MPBVP - Rationale

As has been highlighted previously, the solution of MPBVP of Equations (4.7)-(4.14), and (4.21)-(4.32) by indirect method, is in general not trivial. Firstly, the solution trajectory structure (sequence of constrained arcs, internal points, and unconstrained arcs) could be a priori unknown. Any change in constraint, or addition instances in the problem, lead to derive again the necessary optimality conditions. Other difficulties regard the need to define initial guesses for state, control and, most of all, adjoint variables which usually do not have a clear physical interpretation. Secondly, the solution of this kind of boundary value problems is usually addressed by shooting algorithms, or by NLP techniques. As a consequence, the values of the initial guess strongly affect the convergence of the numerical solution. Therefore, it is quite difficult to automatize the solution of CD&R OCP by indirect methods.

Despite the above, the usage of a differential algebra based on Taylor expansions lead to obtain some advantage when solving a MPBVP. For instance, no numerical approach is needed - DACE tool returns a closed-form analytical expression of the control solution. Secondly, once an analytical expression is obtained, post processing and further manipulations are easily addressed. Another important aspect is that DA treats the variables and parameters of the problem, as independent variable with respect which Taylor polynomial are computed. The results of inversion, derivatives, integrals, and any other algebraic operation on control and state variables are polynomials.

Maps, here referred to as $\mathscr{M}$, express how the variation of any observation (input variable) affects dependent variables. If such maps are the polynomial approximation of implicit equations, that are functions of state and controls, its inversion returns the optimal control solution of the problem as showed in the following sections.

4.6 Differential Algebra

Differential Algebra (DA) is based on the idea to implements a new algebra of Taylor polynomials of any function $f : \mathbb{R}^n \to \mathbb{R}^m$, belonging to the space of k times continuous differentiable functions $\mathscr{C}^k(\mathbb{R}^n)$.

Two k differentiable functions, f and g in n variables are introduced. In the framework of differential algebra, the functions f and g are transformed in their kth-order Taylor expansions, F and G, respectively. Similarly to computer transformation for floating point arithmetic, for each operation in the k differentiable functions space $\mathscr{C}^k$, an adjoint operation in the space of Taylor polynomials is defined. Specifically, expanding the Taylor approximation of f and g and operating them in the space of Taylor polynomials, namely the $_kD_n$ space, returns the same result of operating f and g in their original space and then extracting the Taylor expansion of the resulting function. Fig. 4.3 shows a diagram of the $_kD_n$ algebra.

$$
\begin{array}{ccc}
f, g & \xrightarrow{\ \mathcal{T}\ } & F, G \\[1mm]
\downarrow{\scriptstyle \times} & & \downarrow{\scriptstyle \otimes} \\[1mm]
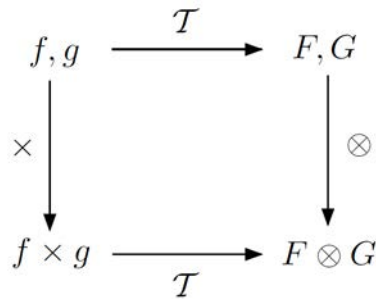f \times g & \xrightarrow[\ \mathcal{T}\ ]{} & F \otimes G
\end{array}
$$

Figure 4.3: Representation of Taylor polynomial algebra $_kD_n$.

On the space $_kD_n$, the following equivalence relation is introduced: given two functions f and $g \in \mathscr{C}^k(\mathbb{R})^n$, $f =_k g$ if and only if $f(0) = g(0)$, and all the partial derivatives of f and g agree at zero up to order k. Therefore, the equivalence $=_k$ satisfies the following conditions

$$f =_k f \quad \forall \quad f \in \mathscr{C}^k(\mathbb{R})^n$$

$$f =_k g \Rightarrow g =_k f \quad \forall \quad f, g \in \mathscr{C}^k(\mathbb{R})^n$$

$$f =_k g \quad \wedge \quad g =_k h \Rightarrow f =_k h \quad \forall \quad f, g, h \in \mathscr{C}^k(\mathbb{R})^n$$

All the elements related to f can be grouped together in one set, namely, the equivalence class $[f]$ of the function f. As a result, each of these classes is then identified by a collection of partial derivatives in all n variables up to order k. This class is so called $_kD_n$, and the following conditions hold

$$[f + g] = [f] + [g], \quad t \cdot [g] = [t \cdot g], \quad [f \cdot g] = [f] \cdot [g]$$

Under these operations, $_kD_n$ becomes an algebra, and the set $(_kD_n, \partial x_1, \ldots \partial x_v)$ with $v = 1, \ldots, n$ is a differential algebra [87]. As a result, f belongs to the same class of its Taylor polynomial $\mathscr{T}_f$ of order k around the origin, so they have the same function values and derivatives up to order k. In symbol,

$$[f] = \mathscr{T}_f \tag{4.42}$$

The differential algebra introduced so far is referred to as Taylor polynomial algebra. Consequently, the derivatives of any function f belonging to $\mathscr{C}^k(\mathbb{R})^n$ can be computed up to order k with low effort in DA environment.

DA techniques can be used for addressing numerous mathematical problems:

- fast computing of high-order Taylor expansion of no polynomial functions;

- fast computing of high-order inverse functions;

- parametric implicit equation solver;

- constraint manifold satisfaction;

- boundary value problem solver;

- Ordinary Differential Equation (ODE) flow expansion in time, in initial conditions, and parameters;

- accurate invariant manifolds expansions.

Various computer implementations of DA have been developing in the last decade. COSY INFINITY [88, 89] employs DA for high-order multivariate study of ODEs, Flows, PDEs, and it also allow high-order multivariate automatic differentiation. Another application of DA techniques is the purpose of the study in [90], where a full Earth-orbiting objects propagator by using model Taylor Algebra approach is implemented. Other examples of DA implementations are the approach developed by [91], or TIDES [92]. Differential Algebra Computational Engine (DACE) [93] developed by Dinamica Srl, is another implementation of basic DA routines in which the result of any mathematical operation is approximated by its Taylor expansion. DACE operations are defined using scripts written in C++ programming language. In DACE framework, is possible to write mathematical expressions in typical computer

programming way, and evaluating them using DA and double precision numbers. In addition to the elementary algebraic operations, DA environment includes operation to perform composition and inversion of functions, explicit solution of nonlinear system, and differentiation and integration of functions. For the reasons above mentioned, DACE is the software used for the purposes of this work.

In this work, DA technique is used as implicit equation solver for the MPBVP defined in Section 3.3, and as Probability Density Function (PDF) mapper. The indirect DA solution approach, and the application as PDF mapper will be treated in Section 4.7.

4.7   Indirect DACE Approach

DA variable is denoted as

$$[x] = x_0 + \delta x \tag{4.43}$$

where $[x]$ represents a Taylor polynomial of the form $\mathscr{T}(\delta x) = x_0 + \delta x$, x_0 is a constant part (the origin of the expansion), and δx represents the independent variable of the expansion. Similarly, given a sufficiently smooth function $f(x) \in \mathscr{C}^k(\mathbb{R})^n$, its Taylor expansion around x_0 truncated at order k is written in DACE environment as

$$[f(x)] = \mathscr{T}_{f(x+x_0)}(\delta x) = \sum_{n=0}^{k} \frac{f^{(n)}(x_0)}{n!}(\delta x - x_0)^n \tag{4.44}$$

and it is easily computed in DACE environment as double precision numbers algebra, i.e., $[f(x)] = f([x])$.

In the work presented here, DACE is used to solve the OCP via indirect method as implicit equation solver for the MPBVP defined in Section 3.3. To this purposes, 4 different DA variables are introduced in the problem: the two controls χ_{OA} and χ_{BF}, and the obstacle center coordinates x_C, y_C. These variables are introduced in a

DACE fashion as,

$$[\chi_{0A}] \triangleq \overline{\chi_{0A}} + \delta\chi_{0A} \tag{4.45}$$

$$[\chi_{BF}] \triangleq \overline{\chi_{BF}} + \delta\chi_{BF} \tag{4.46}$$

$$[x_C] \triangleq \overline{x_C} + \delta x_C \tag{4.47}$$

$$[y_C] \triangleq \overline{y_C} + \delta y_C \tag{4.48}$$

where $\overline{\chi_{0A}}$ indicates the constant part of the DA variables $[\chi_{0A}]$, whereas $\delta\chi_{0A}$ is the independent variables with respect to the taylor polynomial is extracted. Similar considerations can be done for DA variables in Equations (4.46)-(4.48). Since all independent variables treated here are DA variables, for convenience, the input notation $[\cdot]$ to indicate DA variables is dropped.

In order to meet the optimal boundary conditions of the OCP, the two Equations (4.30) and (4.31) have to be satisfied, obtaining

$$f_{HA}(\chi_{0A}, \chi_{BF}, x_C, y_C]) = f_{HA} = H(t_{A+}) - H(t_{A-}) \qquad = 0 \tag{4.49}$$

$$f_{\Pi}(\chi_{0A}, \chi_{BF} x_C, y_C) = f_{\Pi} = \Pi_x(t_{B+}, t_{B-}) - \Pi_y(t_{B+}, t_{B-}) \qquad = 0 \tag{4.50}$$

where Π_x and Π_y are the two components of multiplier vector $\boldsymbol{\Pi}$ defined as

$$\boldsymbol{\Pi} = (\boldsymbol{\lambda}(t_{B+}) - \boldsymbol{\lambda}(t_{B-})) \Big/. \left. \frac{\partial N}{\partial \boldsymbol{x}} \right|_{x(t_{B+})} \tag{4.51}$$

where $/.$ is defined as the element by element division operator. A DA-based evaluation of the functions in Equations (4.49)-(4.50), delivers the kth-order Taylor expansions of such functions with respect to the DA variables χ_{0A} and χ_{BF} as:

$$\delta f_{HA} = \mathcal{M}_{f_{HA}}(\delta\chi_{0A}, \delta\chi_{BF}, \delta x_C, \delta y_C) \tag{4.52}$$

$$\delta f_{\Pi} = \mathcal{M}_{f_{\Pi}}(\delta\chi_{0A}, \delta\chi_{BF}, \delta x_C, \delta y_C) \tag{4.53}$$

where $\mathcal{M}_{f_{HA}}$ and $\mathcal{M}_{f_{\Pi}}$ denote the Taylor maps for f_{HA} and f_{Π}, respectively. The maps are then augmented by introducing the identity function as maps for the others

DA variables (i.e., x_C, y_C) as

$$
\begin{bmatrix} \delta f_{HA} \\ \delta f_{\Pi} \\ \delta x_C \\ \delta y_C \end{bmatrix} = \begin{bmatrix} \mathcal{M} \\ \mathcal{I} \end{bmatrix} \begin{bmatrix} \delta \chi_{0A} \\ \delta \chi_{BF} \\ \delta x_C \\ \delta y_C \end{bmatrix} \tag{4.54}
$$

where $\mathcal{M} : \mathbb{R}^4 \mapsto \mathbb{R}^2$ is the matrix containing the maps $\mathcal{M}_{f_{HA}}$ and $\mathcal{M}_{f_{\Pi}}$, and $\mathcal{I}$ is the 2×2 identity matrix. Equation (4.54) is inverted using DACE built-in tool obtaining

$$
\begin{bmatrix} \delta \chi_{0A} \\ \delta \chi_{BF} \\ \delta x_C \\ \delta y_C \end{bmatrix} = \begin{bmatrix} \mathcal{M} \\ \mathcal{I} \end{bmatrix}^{-1} \begin{bmatrix} \delta f_{HA} \\ \delta f_{\Pi} \\ \delta x_C \\ \delta y_C \end{bmatrix} \tag{4.55}
$$

where $\mathcal{M}^{-1} : \mathbb{R}^4 \mapsto \mathbb{R}^2$ now contains $\mathcal{M}_{\chi_{0A}}(\delta f_{HA}, \delta f_{\Pi}, \delta x_C, \delta y_C)$ and $\mathcal{M}_{\chi_{BF}}(\delta f_{HA}, \delta f_{\Pi}, \delta x_C, \delta y_C)$. To compute the kth-order Taylor expansion of the solution of Equations (4.49)-(4.50), the map vector of Equation (4.55) is evaluated for $\delta f_{HA} = 0$ and $\delta f_{\Pi} = 0$, as

$$
\begin{bmatrix} \delta \chi_{0A} \\ \delta \chi_{BF} \\ \delta x_C \\ \delta y_C \end{bmatrix} = \begin{bmatrix} \mathcal{M} \\ \mathcal{I} \end{bmatrix}^{-1} \begin{bmatrix} 0 \\ 0 \\ \delta x_C \\ \delta y_C \end{bmatrix} \tag{4.56}
$$

obtaining the polynomial approximation of the solution as

$$
\delta \chi_{0A}^* = \mathcal{M}_{\chi_{0A}}(\delta x_C, \delta y_C) \tag{4.57}
$$

$$
\delta \chi_{BF}^* = \mathcal{M}_{\chi_{BF}}(\delta x_C, \delta y_C) \tag{4.58}
$$

Equations (4.57) and (4.58) express how the variation of the variables $\delta x_C, \delta y_C$ affects the solution of the implicit Equations (4.49) and (4.50). In particular, by plugging the maps of Equations (4.57) and (4.58) in the Equations (4.45) and (4.46), respectively, the following relations are obtained

$$
\mathcal{T}_{\chi_{0A}} = \overline{\chi_{0A}} + \mathcal{M}_{\chi_{0A}}(\delta x_C, \delta y_C) \tag{4.59}
$$

$$
\mathcal{T}_{\chi_{BF}} = \overline{\chi_{BF}} + \mathcal{M}_{\chi_{BF}}(\delta x_C, \delta y_C) \tag{4.60}
$$

which are the kth-order Taylor expansions of the solution of the problem. The accuracy of the approximation depends on both the order of the Taylor expansion, and the displacement from the origin of the expansion. Equations (4.59) and (4.60) maps the control solution $\chi(t)^*$ taking into account the uncertainty of the obstacle position. As a result, the trajectory solution map derived from such controls, it describes the trajectory uncertainty based on the the obstacle position stochasticity. The method employed to find the solution of problem is summarized in Algorithm 1. Moreover, manipulating the PDF of the obstacle center, and combining the polynomial expansions of the solution trajectory with the PDF of the solution controls, a trajectory probability indicator is introduced. This aspect will be treated in Subsection 4.8.

Algorithm 1 Indirect DACE approach

Require: : $(x_0, x_f, \mu, \Sigma, p_{X_C}, k)$
Ensure: : $u = \chi(t)$
 1: Set order of expansion k
 2: Initialize DA Variables $[\chi_{0A}], [\chi_{BF}], [x_C], [y_C]$
 3: Find collision points $A(\chi_{0A}, x_C, y_C)$ and $B(\chi_{BF}, x_C, y_C)$
 4: Define functions $f_{HA}(\chi_{0A}, \chi_{BF}, x_C, y_C) = H(t_{A+}) - H(t_{A-})$
 5: Define function $f_\Pi(\chi_{0A}, \chi_{BF}, x_C, y_C) = \Pi_x(t_{B+}, t_{B-}) - \Pi_y(t_{B+}, t_{B-})$
 6: Compute polynomial expansion $\delta f_{HA}(\chi_{0A}, \chi_{BF}, x_C, y_C)$
 7: Compute polynomial expansion $\delta f_\Pi(\chi_{0A}, \chi_{BF}, x_C, y_C)$
 8: Invert δf_{HA}, δf_Π to obtain the maps $\mathcal{M}_{\chi_{0A}}$ and $\mathcal{M}_{\chi_{BF}}$
 9: Evaluate $\mathcal{M}_{\chi_{0A}}(0, 0, \delta x_C, \delta y_C)$ and $\mathcal{M}_{\chi_{BF}}(0, 0, \delta x_C, \delta y_C)$
10: Compute the k-th order Taylor expansion $\mathcal{T}_{\chi_{0A}}(\delta x_C, \delta y_C)$ and $\mathcal{T}_{\chi_{BF}}(\delta x_C, \delta y_C)$

4.8 DACE as PDF Mapper

With objective of mapping the PDF of obstacle position into the PDF of the OCP solution, DACE is used to determine the PDF Taylor expansion with respect to the controls χ_{0A}, χ_{BF}, namely $p(\chi_{0A}, \chi_{BF})$. As described in [94], and using the axiom of probability conservation and the rules of change of variables in multiple integrals, the PDF $p(\chi_{0A}, \chi_{BF})$ can be approximated as

$$p(\chi_{0A}(x_c, y_c), \chi_{BF}(x_c, y_c)) = p_{\mathbf{X}_C}(x_c, y_c) \, 1 / \mathcal{T}_{|\det \mathbf{J}_{\mathcal{M}}|} \tag{4.61}$$

where $\mathcal{M} : \mathbb{R}^2 \mapsto \mathbb{R}^2$ is the matrix containing the maps $\mathcal{M}_{\chi_{0A}}$ and $\mathcal{M}_{\chi_{BF}}$, and $\mathbf{J}_{\mathcal{M}}$ is the Jacobian Matrix of $\mathcal{M}$. This approach is named as partial DA mapping method, and the final PDF is obtained by the multiplication of the starting PDF $p_{\mathbf{X}_c}(x_c, y_c)$ and the Taylor polynomial of the Jacobian determinant term.

The method employed to approximate the PDF solution map $p(\chi_{0A}, \chi_{BF})$ is summarized in Algorithm 2. For the purpose of this work, PDF solution map is used to introduce a trajectory "optimality level", i.e., a probability indicator (PDF discrete value) that it is related to the real probability that such trajectory is the optimal one in terms of flight time and constraint satisfaction. In other words, given the optimal trajectory $S^*(\chi^*(t)) : \mathbb{R} \mapsto \mathbb{R}^2$ derived from initial and final controls $(\chi_{0A}^*, \chi_{BF}^*)$ is considered, the optimality level of the trajectory S^* is defined as the PDF value associated to controls $(\chi_{0A}^*, \chi_{BF}^*)$, i.e., $p(\chi_{0A}^*, \chi_{BF}^*)$.

Algorithm 2 DACE as PDF mapper

Require: $: (\mathcal{M}_{\chi_{0A}}, \mathcal{M}_{\chi_{BF}}, \boldsymbol{\mu}, \boldsymbol{\Sigma}, p_{\mathbf{X}_C}, k)$
Ensure: $: p(\chi_{0A}, \chi_{BF})$
  1: Set order of expansion k
  2: Compute polynomial expansion of $\det \mathbf{J}_{\mathcal{M}}(\delta x_C, \delta y_C)$
  3: Compute
      $p(\chi_{0A}(\delta x_C, \delta y_C), \chi_{BF}(\delta x_C, \delta y_C)) = p_{\mathbf{X}_C}(x_C, y_C) \, 1 / [|\det \mathbf{J}_{\mathcal{M}}(\delta x_C, \delta y_C)|]$

As a further step, the PDF of the obstacle center is manipulated to obtain trajectories that avoid the obstacle with a certain Level of Confidence (LoC). This is addressed by employing the three-sigma rule generalized for the multivariate normal distribution. In [95], the Standard Deviation Curves (SDCs) are defined as the regions containing the uncertain variable with a specified confidence interval, and the dimension of such regions depend only on the covariance matrix $\boldsymbol{\Sigma}$. Once

the SDCs for each desired confidence interval are obtained, DACE provides all the possible optimal trajectories considering the obstacle on the SDC. For each SDC, an envelope of optimal trajectories is obtained, and the envelope boundaries represent the optimal trajectories with free-conflict probability equal to the LoC.

Chapter 5

OCP with Stochastic Path Constraint - Results

5.1 Results Overview

In this section, the results of the CD&R problem introducing the obstacle position as Normal Gaussian PDF are presented. Firstly, the optimal trajectory is computed in a deterministic manner by using the DACE indirect approach and the expected value of the obstacle position $\boldsymbol{\mu}$. Then, the uncertainty map (or optimality map), i.e., the Taylor expansion of the solution with respect to the uncertain parameter $\boldsymbol{X}_c(x_C, y_C)$, is computed. Afterwards, SDCs [95] associated to the covariance matrix $\boldsymbol{\Sigma}$ are drawn, and trajectories with constant Collision Avoidance (CA) probability are obtained for different confidence levels. Finally, the effectiveness of the proposed algorithm based on DA technique is verified by Monte Carlo (MC) simulations. In each MC iteration, the optimal control MPBVP is solved by a simple shooting algorithm. For the sake of observing MC simulations convergence, before running the MC simulations with a bi-variate Gaussian Normal distribution $\mathbf{X}_C \sim \mathcal{N}(\boldsymbol{\mu}, \boldsymbol{\Sigma})$, each of the obstacle center coordinates are assumed to follow 1D Normal Gaussian distributions $X_C \sim \mathcal{N}(\mu_{xc}, \Sigma_{xc})$ and $Y_C \sim \mathcal{N}(\mu_{yc}, \Sigma_{yc})$, separately. Eventually, the comparison between the optimal controls obtained with DACE and MC simulations is presented. All simulations were performed on a Windows 64-bit system with two Intel-i7 of 2GHz and 8GB RAM.

5.2   DACE Indirect Method and PDF Mapper

With respect to the scenario represented in Figure. 4.1, the normalized set-up data of Table 5.1 are introduced. For the nondimensionalization of coordinates and velocity, the maximum Cartesian coordinate x, and the aircraft true air speed V_{TAS} have been used, respectively [1].

In order to choose a suitable expansion order for DACE Taylor polynomials, different DACE simulations are computed iteratively by increasing the order of expansion. Table 5.2 shows the DACE expected solutions [2], i.e., the deterministic trajectory obtained by assuming the position of the obstacle equal to the mean values μ_{x_C}, μ_{y_C}, by varying the order of polynomials. t is possible to observe that, as the order of expansions increases, the DACE solution tends to converge to specific angles. By simple geometric considerations, it is possible to rapidly verify the correctness of these values, which correspond to the tangent angles to the circumference centered in μ_{x_C}, μ_{y_C} and also included in Table 5.2.

Theoretically, the higher the order of expansion, the lower is the truncation error of polynomial approximation. Nonetheless, since DACE handles with DA polynomials numerically, increasing the order of expansion to very high values could lead to divergence problems, i.e., polynomials diverge very fast (tend to infinity) around the origin of the expansion. For the purpose of the problem presented here, to avoid burdensome evaluation of very high order polynomials, and to avoid divergence issues, the solution of the CD&R problem by indirect DACE approach has been addressed by using polynomials up to 9-th order. Figure 5.1 represents the expected solutions (black solid lines).

Hamiltonian and Lagrange multipliers deriving from the indirect method have been also validated by shooting algorithm. Figure 5.3, Figures 5.4a-5.4b, and Figure 5.5, show the time history of the expected values (black solid lines) of controls, costates, and inequality constraint multipliers, respectively. At this stage, it is possible to state that indirect DACE method solved correctly the deterministic OCP, and the solution of the deterministic problem corresponds to the $0 - th$ order term of the DA Taylor polynomial approximation.

---

[1]Distance between initial and final waypoint $\|\overline{OF}\|$ is the most suitable choice for distance nondimensionalization. This choice affected only numerical values of boundary conditions.

[2]For the sake of conciseness, and since both trajectories are symmetric, only one optimal trajectory (two tangent angles) is presented in Table 5.2.

Figure 5.2 shows the contour lines of the PDF Taylor approximation $p(\chi_{0A}, \chi_{BF})$ obtained by DACE, the PDF maxima (the mode), and the DACE expected controls. Figure 5.1 gives a qualitative indication of the probability that a prescribed avoidance trajectory is the optimal one. With reference to Figure. 5.1, darker areas are more probable to contain the optimal trajectory than the lighter areas. Conversely, trajectories in darker areas are more probable to collide with the obstacle. Therefore, the aircraft can choose the proper maneuver to avoid the obstacle by relying on Figure 5.3, but considering only the control at the initial time t_0, i.e. χ_{0A}. In facts, the solution expansion is not time-based, or in other words, given a time instant $t_k \in [t_0, t_f]$, it is not necessary true that the most probable optimal control at t_k is the corresponding heading angle $\chi(t_k)$ with the highest optimality level. This is due to the fact that, depending on the real position of the aircraft and the cross-track error with respect to the real optimal route, a certain heading can lead the vehicle far from the final waypoint, or worse, colliding the obstacle. On the other hand, at t_0, and during the constrained arc $\overline{0A}$, it is true that the maneuver that are most probable to be tangent to the obstacle are those with highest optimality level (darker region in Figure 5.1). Similar consideration can be done for the time history of controls, costates, and inequality constraint multiplier. Figure 5.3, Figures 5.4a-5.4b, and Figure 5.5, depict the polynomial expansion (optimality map) of controls, costates, and inequality constraint multipliers, respectively.
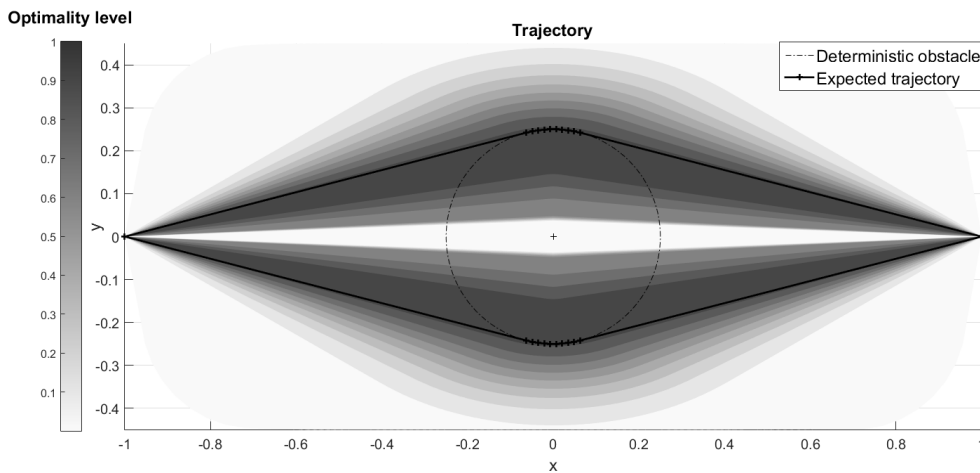

Figure 5.1: Optimal trajectory map, and expected trajectories (black solid lines).

Table 5.1: Normalized set-up data for the stochastic obstacle case study.

Waypoint	x	y	Γ	V	μ_{x_C},	μ_{y_C}	σ_{x_C}	σ_{y_C}
O	-1	0	0.25	1	0	0	0.2	0.1
F	1	0						

Table 5.2: DACE expected solution as a function of polynomial expansion order, and analytical solution (tangent angles).

order of expansion of DA polynomials	Expected solution χ_{0A} [deg]	expected value of χ_{BF} [deg]
1	14.3984026	-14.3984026
2	14.4561381	-14.4561381
3	14.4766188	-14.4766188
4	14.4773355	-14.4773355
5	14.4775001	-14.4775001
6	14.4775102	-14.4775102
7	14.4775120	-14.4775120
8	14.4775122	-14.4775122
9	14.4775122	-14.4775121
Analytical Solution	14.4775122	-14.4775122
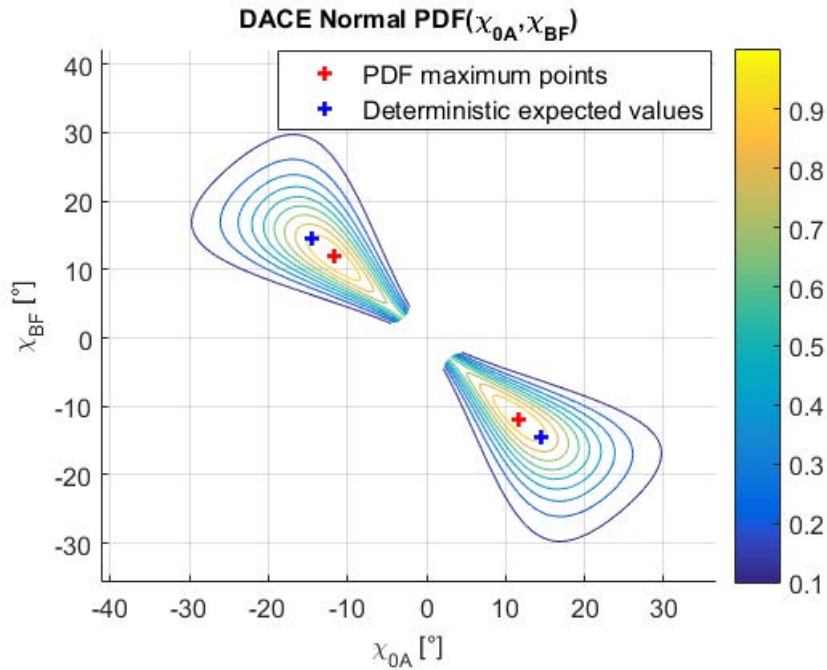
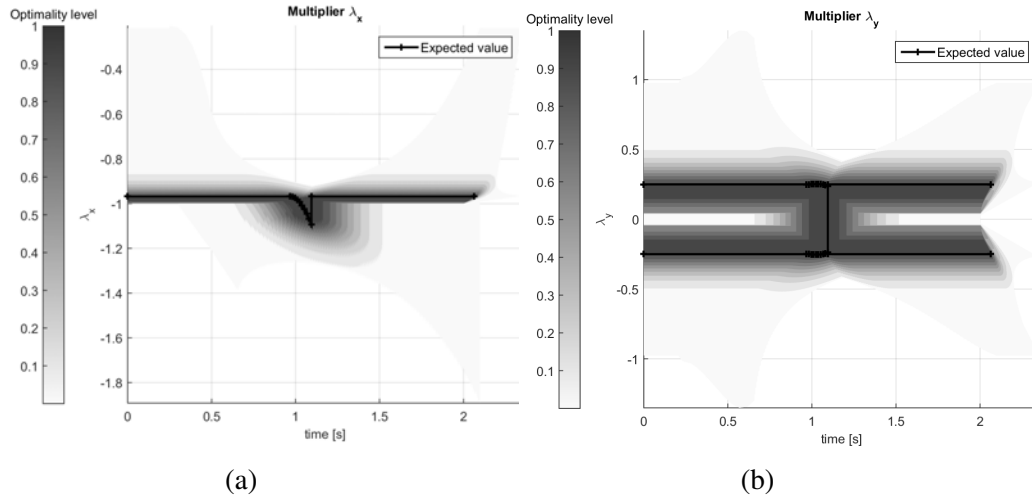Figure 5.2: PDF Taylor expansion of controls χ_{0A}, χ_{BF}.

(a)

(b)

Figure 5.4: Optimality level and expected time history (solid black line) of costates λ_x (a) and λ_x (b).
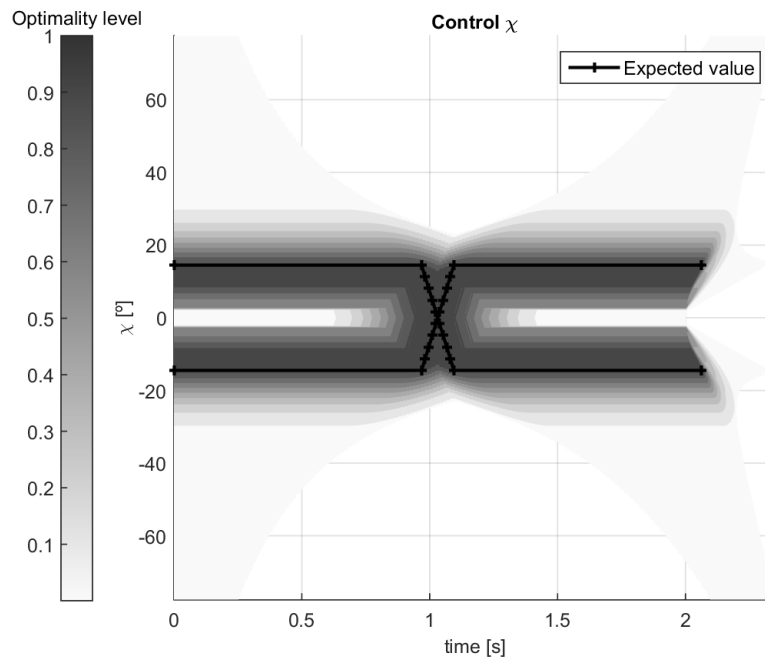

Figure 5.3: Optimality level and expected time history (solid black line) of controls χ.
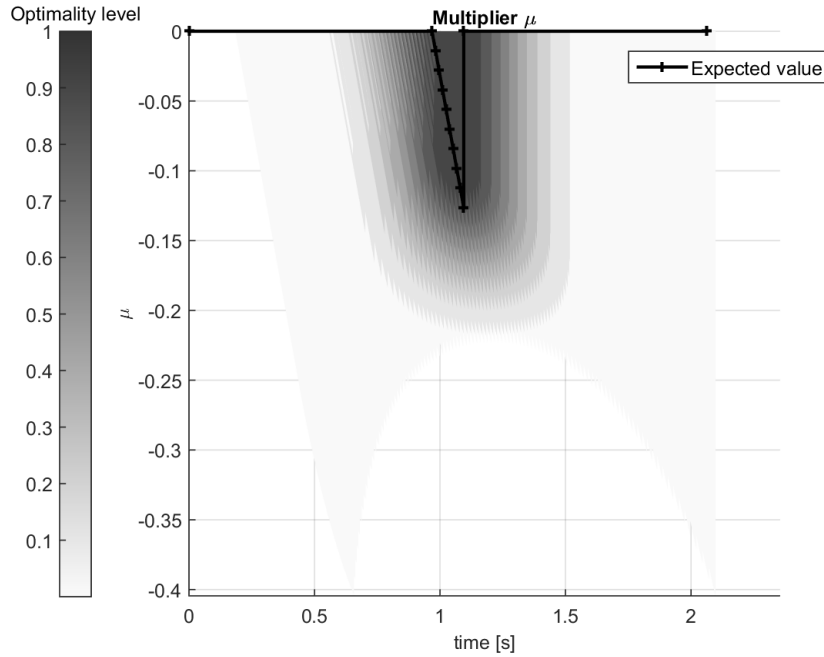
Figure 5.5: Optimality level and expected time history (solid black line) of inequality constraint multiplier μ.

5.3 Collision Avoidance Probability

Later, PDF $p_{\boldsymbol{X}_C}(x_C, y_C)$ is used to compute the optimal trajectories with specific Collision Avoidance (CA) probability values. In order to know the optimal trajectories that avoid the obstacle with a prescribed confidence level, DACE software is employed along the SDCs for three different CA probabilities, i.e., 68%, 95%, and 99%. These LoCs correspond to three-sigma rule generalized for the multivariate normal distribution. Figure 5.6 shows the obstacle distribution SDCs for the levels of confidence chosen. SDCs are those regions that contain the obstacle center with a probability equal to the level of confidence chosen. Therefore, trajectories tangents to the envelope traced by the obstacle along these curves, have a probability to avoid the obstacle equal to the chosen level of confidence.
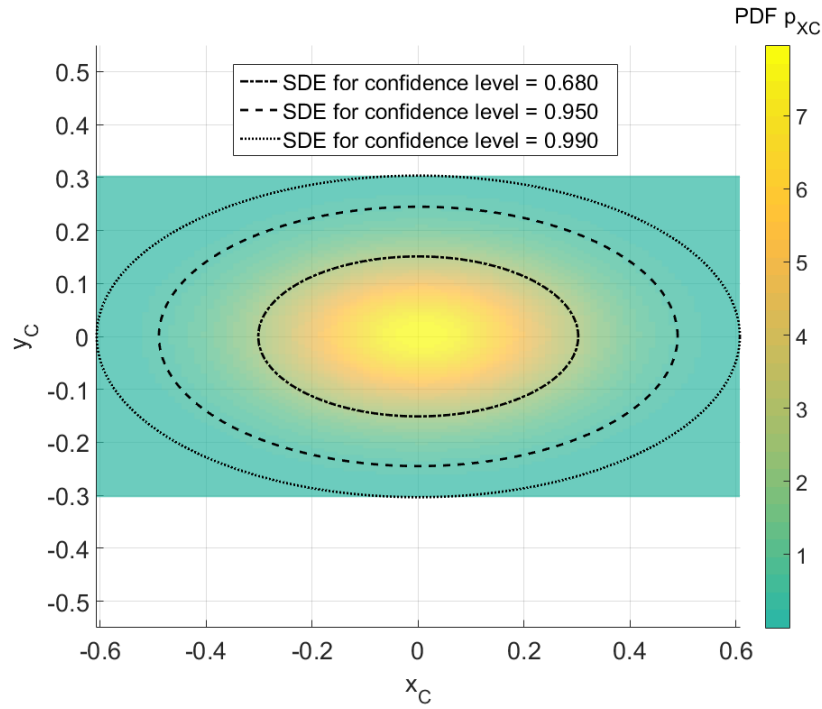
Figure 5.6: Standard Deviation Curves for 68%, 95%, and 99% levels of confidence.

Figure 5.7 shows the trajectories that avoid the obstacle with the prescribed CA probability. According to this approach, the CA probability of the expected trajectory is equal to 0, indeed, this trajectory touches the constraint on the boundary. From an operational point of view, when the obstacle is detected by on-board sensors, the aircraft should want to choose the best trade-off between optimality (time of flight), and collision risk. Assuming χ_{0A} as the decision variable, Figure. 5.8 compares different Time of Flight (ToF) values accordingly to χ_{0A} and CA probabilities chosen. Clearly, Figure 5.8 shows that collision risk generally grows when ToF decreases. For instance, when CA probability is 95%, the corresponding χ_{0A} and ToF are 37.18° and 2.29 s, respectively, so χ_{0A} is greater than the expected value 14.4775°, and the ToF is about 10% greater than the expected one that is about 2.06. The graph of Figure. 5.8 gives therefore an indication for making the best trade-off decision: a χ_{0A} close to the expected value means saving ToF while assuming a bigger risk of collision, and vice versa. The limitation of this methodology is that no considerations can be done for χ_{0A} lower than the expected one, i.e., when the aircraft wants to risk more than the expected value.

Table 5.3: DACE expected solution and initial and final heading for different CA probabilities.

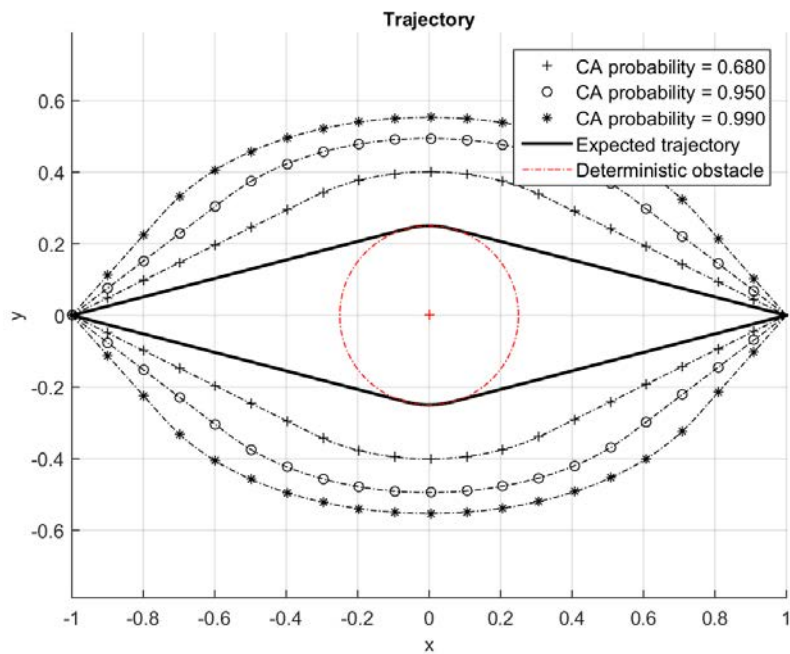|	χ_{0A} [deg]	χ_{BF} [deg]	ToF [s]
DACE Expected solution	14.4775	-14.4775	2.063
CA 0.68	26.0881	-26.0881	2.174
CA 0.95	37.1790	-37.1790	2.289
CA 0.99	48.0460	-48.0460	2.394

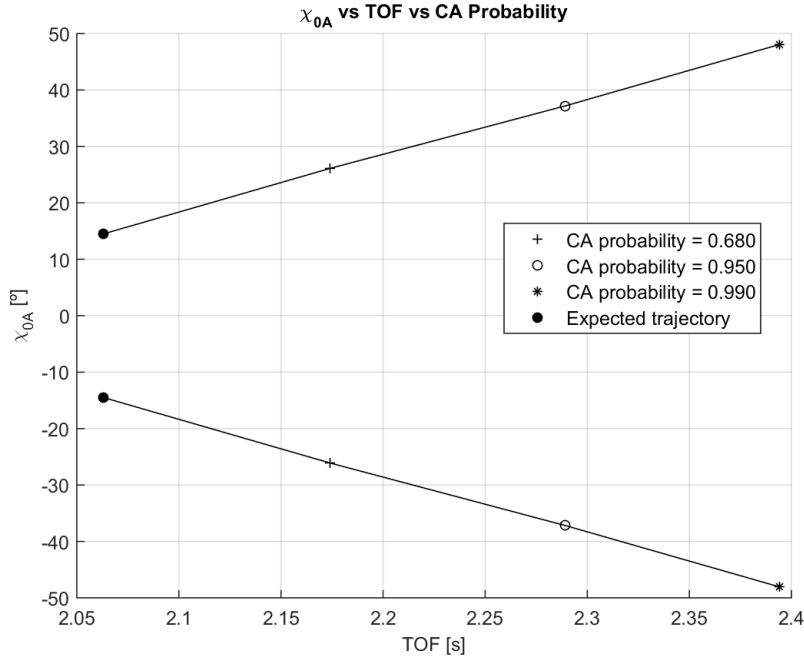Figure 5.7: Optimal trajectories for different CA probability.

Figure 5.8: CA probability and Time of Flight (ToF) as functions of the decision variable χ_{0A}.

5.4   Montecarlo Simulation - Univariate Case

In general terms, it is difficult to estimate the size of samples needed for achieving a prescribed precision with multivariate MC simulation. For this reason, the validation of DACE results were validated firstly by running unidimensional cases.

The aim of the simulations was to find a suitable parametric distribution for optimal controls, among those available in statistics, which fits properly MC results and DACE Taylor approximation. Main attention was given to the mode of the optimal controls, i.e., the maximum of the PDF, here referred to as χ_{0A}^* and χ_{BF}^*. For the sake of clarity and ease of comprehension, only one group of tangents are presented in this section. In facts, since a symmetric scenario was chosen, in principle, two sets of (χ_{0A}, χ_{BF}) would have been obtained as optimal solutions. Without loss of generality, all the results presented here refers to $\chi_{0A} \geq 0$ and $\chi_{BF} \leq 0$, which correspond to an "upper" solution trajectory.

According to the univariate approach, each of the obstacle coordinates was assumed to follow a 1D Normal Gaussian PDF of the form

$$X_C(x_C) \sim \mathcal{N}(\mu_{x_C}, \sigma_{x_C}) = \frac{1}{\sqrt{2\pi\sigma_{x_C}^2}} \exp\left(-\frac{(x_c - \mu_{x_C})^2}{2\sigma_{x_C}^2}\right) \qquad (5.1)$$

$$Y_C(y_C) \sim \mathcal{N}(\mu_{y_C}, \sigma_{y_C}) = \frac{1}{\sqrt{2\pi\sigma_{y_C}^2}} \exp\left(-\frac{(y_c - \mu_{y_C})^2}{2\sigma_{y_C}^2}\right) \qquad (5.2)$$

Two distinct cases were run: the *1DX* case, where X_C was assumed to be a stochastic variable, while y_C was fixed to its constant expected value μ_{y_C}; and the *1DY* case, where Y_C was assumed to be a stochastic variable, while x_C was equal to its constant expected value μ_{x_C}. Parameters $\sigma_{x_C}, \sigma_{y_C}, \mu_{x_C}, \mu_{y_C}$, are those defined in Table 5.1.

5.4.1 Case 1DY

Table 5.4 shows the results of optimal solution mode obtained by DACE, and the mode estimated by MC simulations for the 1DY case. At the expense of a great computational burden for MC simulations, in Table 5.4 it is possible to observe that MC results seem to converge to DACE values for modes χ_{0A}^* and χ_{BF}^*.

Table 5.4: DACE and MC mode results - case 1DY

	Expected solution[deg]		Error % w.r.t. DACE		CPU time [s]
	χ_{0A}^*	χ_{BF}^*	χ_{0A}^*	χ_{BF}^*	
DACE	14.5480	-14.5480	n.a.	n.a	0.774
MC 1e1	18.4113	-18.4924	26.56	27.11	1.64
MC 1e2	8.0764	-16.5311	44.48	13.63	2.76
MC 1e3	12.936	-13.0406	11.08	10.36	18.49
MC 1e4	16.1918	-11.9885	11.3	17.59	170.92
MC 1e5	15.0493	-15.1726	3.45	4.29	2010.90
MC 1e6	13.3999	-14.8936	7.89	2.38	15984
MC 1e7	15.0508	-14.7553	3.46	1.42	147760

With reference to the optimal control χ_{0A}, Figure 5.9 shows the trend of χ_{0A} DACE PDF polynomial, and the PDF histogram graph fitted by a normal Gaussian distribution for MC simulation with 10^7 samples. In Figure 5.12 a comparison between both curves is shown.

With reference to the optimal control χ_{BF}, similar considerations can be done. Figure 5.11 shows the trend of χ_{BF} DACE PDF polynomial, and the PDF histogram graph fitted by a normal Gaussian distribution for MC simulation with 10^7 samples. In Figure 5.12 a comparison between both curves is shown.

Even though DACE PDF mode is similar to the value estimated by MC, it is possible to observe a discrepancy between the two curves for both χ_{0A} and χ_{BF} in Figures 5.10 and 5.12, respectively. The cause of this discrepancy can reside on wrong scaling factor chosen for the DACE approximation, in a wrong parametric distribution fitting function chosen for MC results, or in a combination of both. Nonetheless, other causes of discrepancy are still under investigation up to the date on which this work is presented.
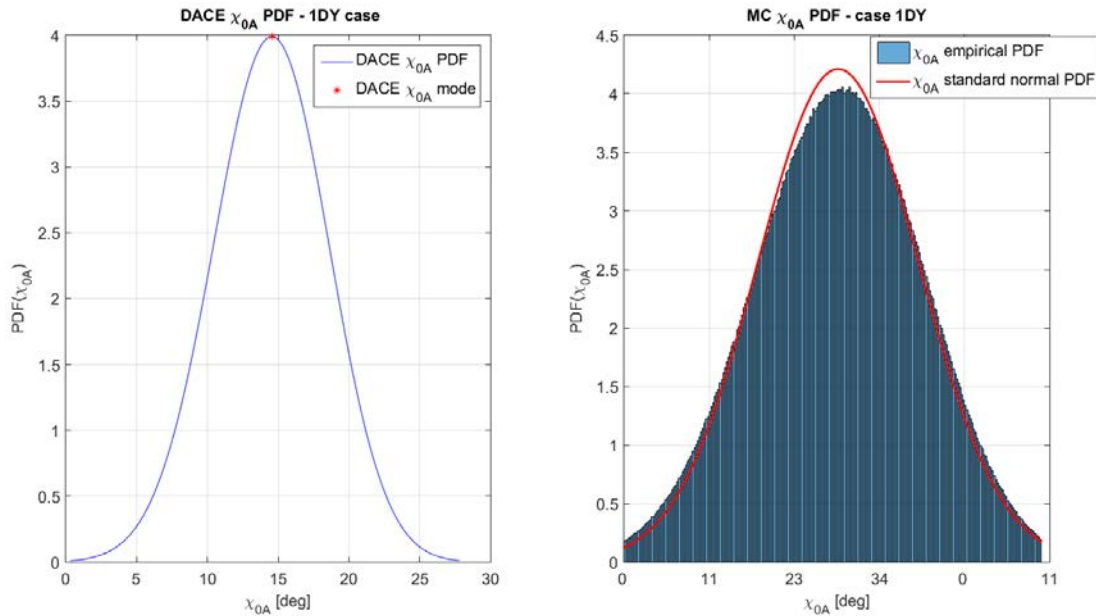

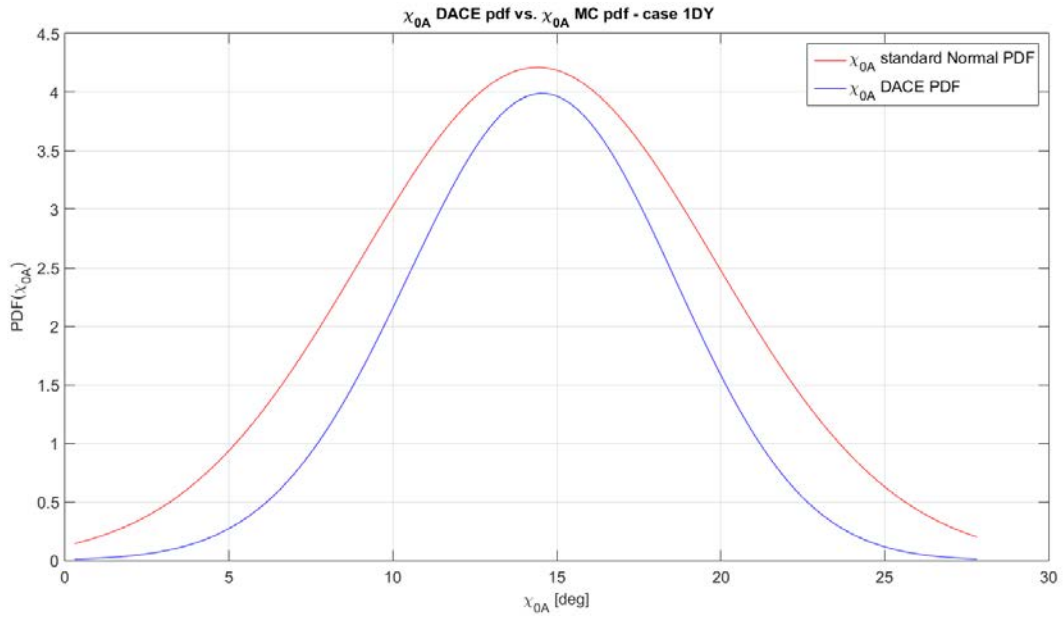Figure 5.9: DACE (left) and MC χ_{0A} PDFs for 10^7 samples (right) - case 1DY.

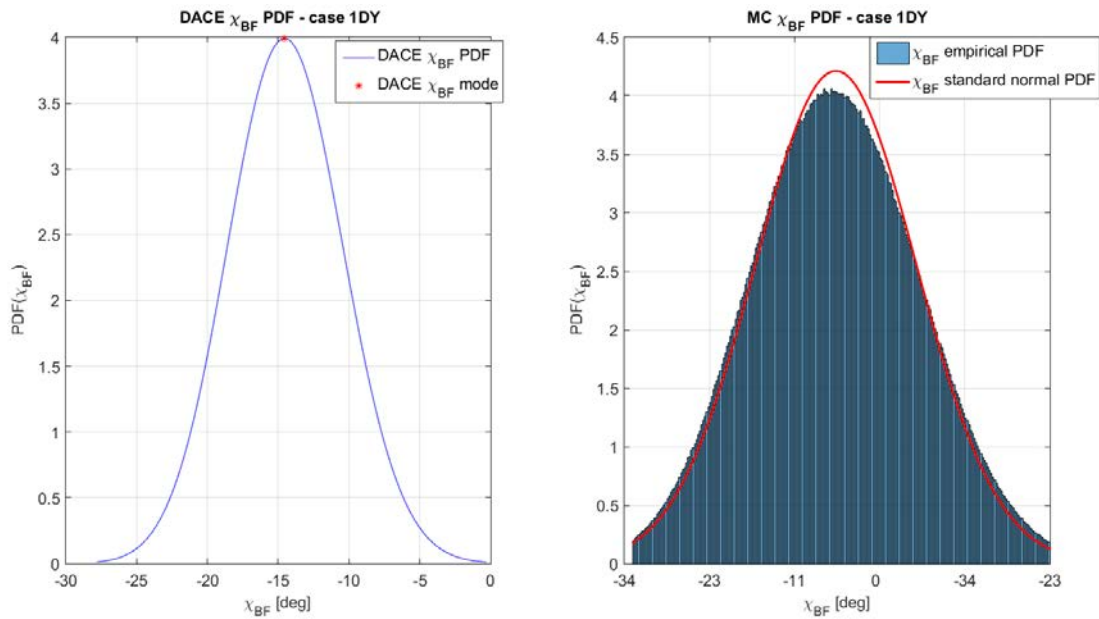Figure 5.10: DACE and MC χ_{0A} PDFs for 10^7 samples - case 1DY.

Figure 5.11: DACE (left) and MC χ_{BF} PDFs for 10^7 samples (right) - case 1DY.

Figure 5.12: DACE and MC χ_{BF} PDFs for 10^7 samples - case 1DY.

Table 5.5: Mean and standard deviation of MC results for 10^7 samples - case 1DY

	distribution	μ [deg]	σ [deg]
	PDF interpolant of MC 10^7 simulation		
χ_{0A}	normal	14.412	5.427
χ_{BF}	normal	-14.412	5.427

5.4.2   Case 1DX

Table 5.6 shows the results of optimal solution mode obtained by DACE, and the mode estimated by MC simulations for the 1DY case. At the expense of a great computational burden for MC simulations, in Table 5.6 it is possible to observe that MC results seem to converge to DACE values for modes χ_{0A}^* and χ_{BF}^*.

Table 5.6: DACE and MC mode results - case 1DX

	Expected solution [deg]		Error % w.r.t. DACE		CPU time [s]
	χ_{0A}^*	χ_{BF}^*	χ_{0A}^*	χ_{BF}^*	
DACE	13.8418	-13.8418	n.a.	n.a.	0.774
MC 1e1	11.4139	-11.5321	17.54	16.69	1.83
MC 1e2	12.3438	-15.6006	10.82	12.71	2.40
MC 1e3	11.9035	-14.8178	14	7.05	14.69
MC 1e4	11.7605	-14.7861	15.04	6.82	173.65
MC 1e5	13.6935	-13.5464	1.07	2.13	2752.6
MC 1e6	13.7552	-13.6257	0.63	1.56	24643
MC 1e7	13.5158	-13.4432	2.35	2.88	203640

With reference to the optimal control χ_{0A}, Figure 5.13 shows the trend of chi_{0A} DACE PDF polynomial, and the PDF histogram graph fitted by a log-logistic Gaussian distribution for MC simulation with 10^7 samples. In Figure 5.12 a comparison between both curves is shown.

With reference to the optimal control χ_{BF}, similar considerations can be done. Figure 5.15 shows the trend of χ_{BF} DACE PDF polynomial, and the PDF histogram graph fitted by a log-logistic Gaussian distribution for MC simulation with 10^7 samples. In Figure 5.16 a comparison between both curves is shown.

Even though DACE PDF mode is similar to the value estimated by MC, it is possible to observe a discrepancy between the two curves for both χ_{0A} and χ_{BF} in Figures 5.14 and 5.16, respectively. The cause of this discrepancy can reside on wrong scaling factor chosen for the DACE approximation, in a wrong parametric distribution fitting function chosen for MC results, or in a combination of both. Nonetheless, other causes of discrepancy are still under investigation up to the date on which this work is presented.

Figure 5.13: DACE (left) and MC χ_{0A} PDFs for 10^7 samples (right) - case 1DX.

Figure 5.14: DACE and MC χ_{0A} PDFs for 10^7 samples - case 1DX.

Figure 5.15: DACE (left) and MC χ_{BF} PDFs for 10^7 samples (right) - case 1DX.
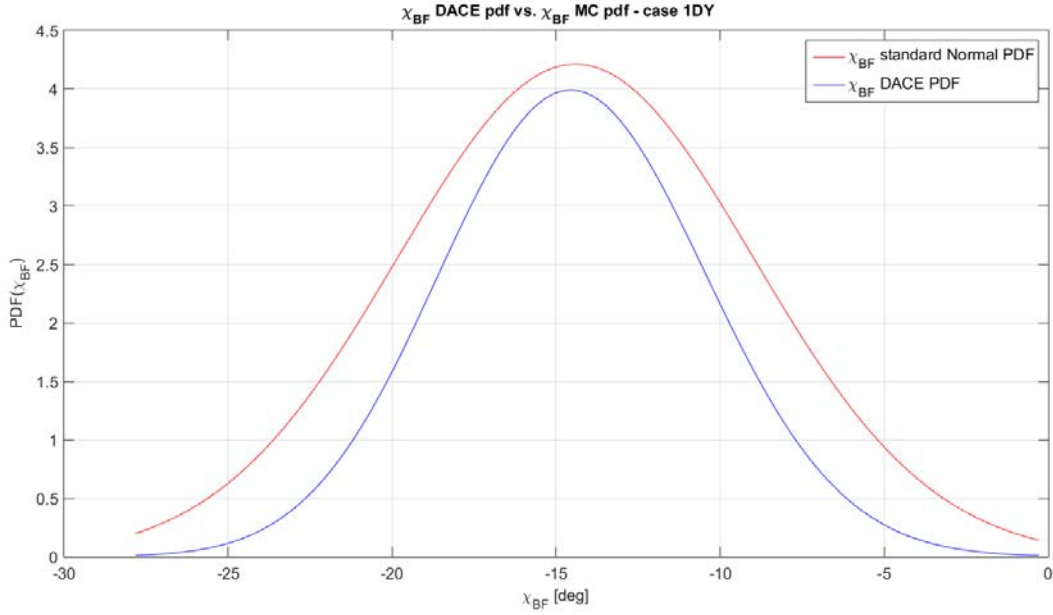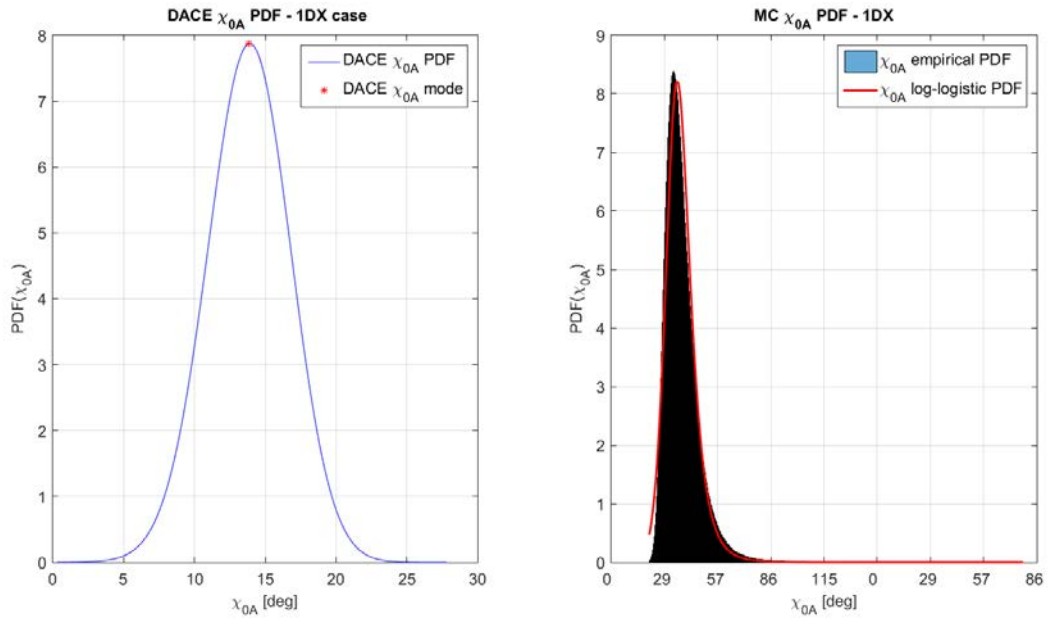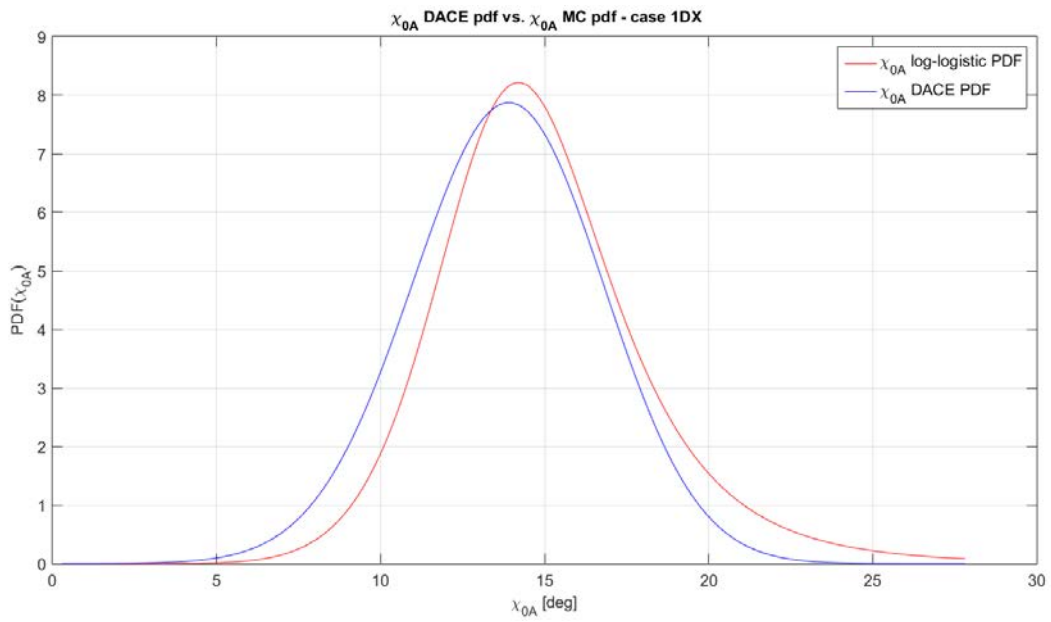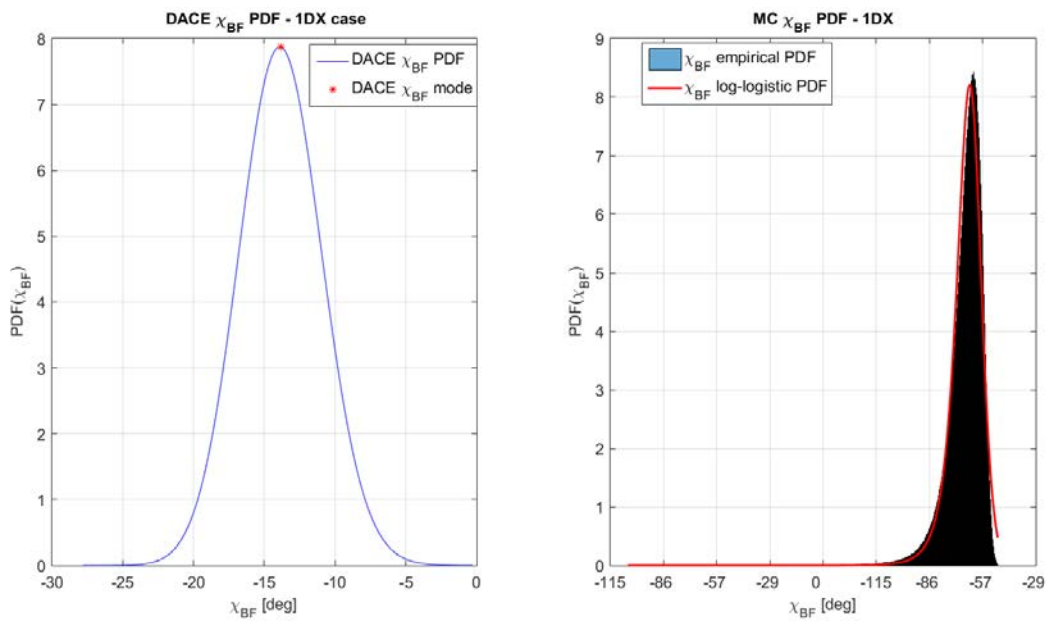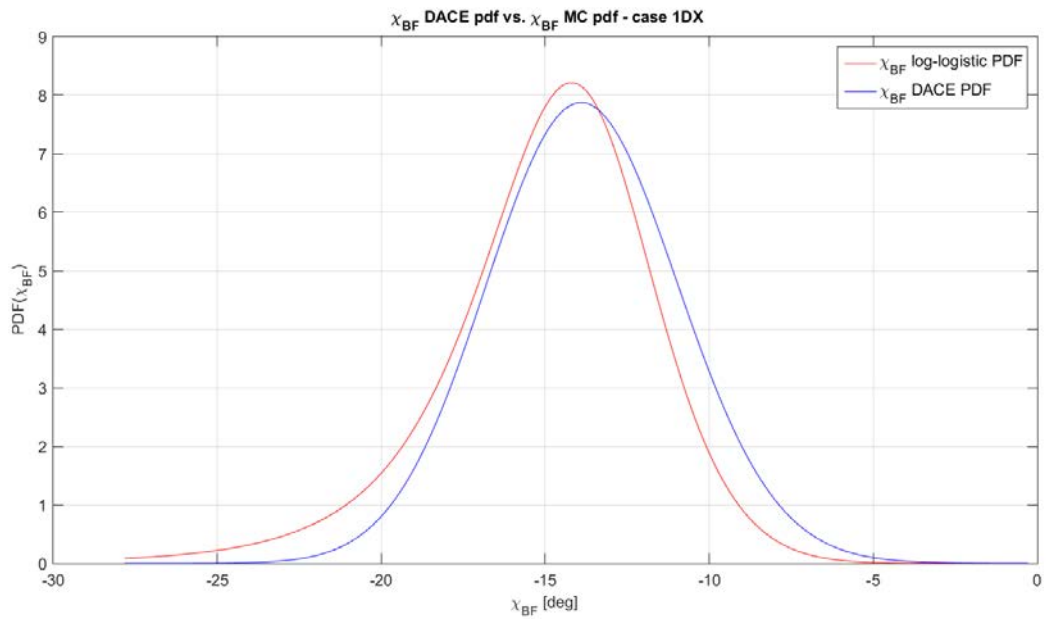

Figure 5.16: DACE and MC χ_{BF} PDFs for 10^7 samples - case 1DX.

Table 5.7: Mean and standard deviation of MC results for 10^7 samples - case 1DX

	PDF interpolant of MC 10^7 simulation		
	distribution	μ [deg]	σ [deg]
χ_{0A}	log-logistic	14.625	6.930
χ_{BF}	log-logistic	-14.626	6.931

5.5 Montecarlo Simulation - Bivariate Case

Finally, the effectiveness of indirect DACE approach has been validated by running set of MC simulations for bi-variate normal distribution data. In the simulations presented here, the obstacle center coordinates are supposed to follow a 2D Normal Gaussian Distribution defined in Equation (4.5). As a result, both MC and DACE optimal control modes have been compared in Figure.5.17, and simulation results are resumed in Table 5.8. Clearly, the mode estimated by MC simulations tends to converge to the DACE solution showing an error at most of 4.2% for 10^5 samples. Higher samples simulations were limited by the CPU load required. As a consequence, the advantage that stands out by using DACE is the very low computational load required. In order to obtain an accurate solution, the CPU time for the MC simulation is several orders of magnitudes bigger than those required for the Indirect DACE approach. Moreover, when compared to MC approach, DACE provides the polynomial expansion of the solution around a point, therefore returning an analytical continuous solution of the problem.

Table 5.8: Comparison between DACE and MC solution - bivariate case.

	Mode [deg]		Error % w.r.t. DACE		CPU time [s]
	χ_{0A}^*	χ_{BF}^*	χ_{0A}^*	χ_{BF}^*	
DACE	11.7164	-11.8874	n.a.	n.a.	1.18
MC 10^1	19.7892	-29.9064	68.9	151.58	3.27
MC 10^2	17.3244	-20.2686	47.86	70.51	4.77
MC 10^3	19.5177	-15.5716	66.58	30.99	32.46
MC 10^4	19.5898	-11.8694	67.2	0.15	258.63
MC 10^5	15.2008	-13.6178	29.74	14.56	2430.4
MC 10^6	10.9143	-10.7503	6.85	9.56	25125.74
MC 10^7	11.589	-11.7017	1.09	1.56	280091.16
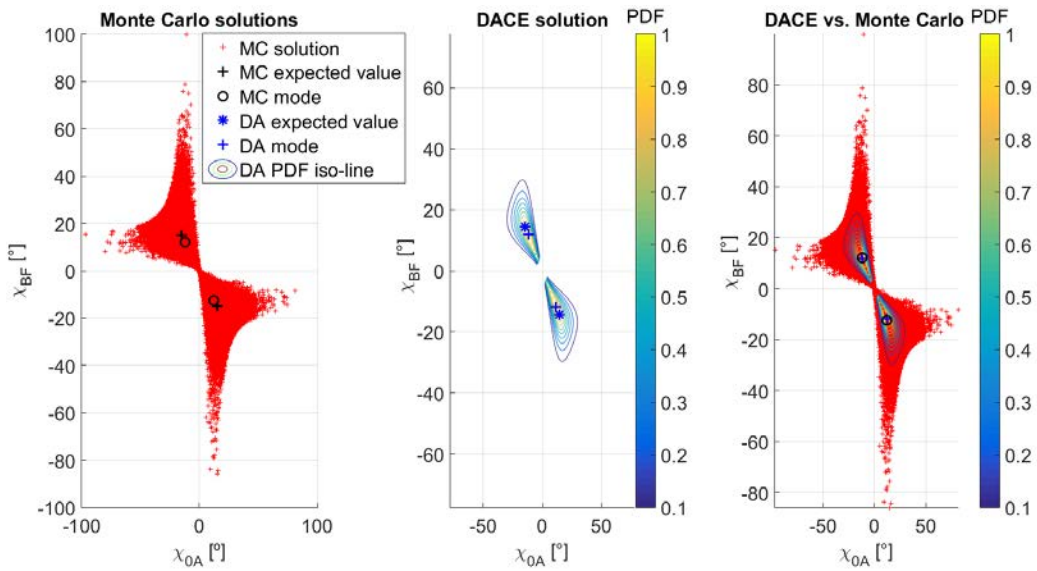
Figure 5.17: DACE and MC solutions for 10^5 samples.

Chapter 6

Conclusions

The stochastic CD&R problem presented in this work has been solved by employing the indirect optimal control approach, and DACE tool. DACE defined a differential algebra of Taylor polynomials that easily provided the solution map of implicit optimality conditions. DACE has been also used to model the uncertainty of the obstacle position in the airspace, and consequently, to obtain the polynomial expansion of the optimal solution trajectory. Trajectories with prescribed CA confidence levels have been also computed. The algorithm proposed has shown great potential in rapidly solving the implicit equation formed by optimality conditions in presence of a stochastic constraint. The effectiveness of such method has been validated by Monte Carlo (MC) simulation, and both solutions (DACE and MC) have been compared in terms of accuracy and computational cost.

With respect to other approaches, DACE has been exploited to obtain a closed-form analytical expression of the OCP solution in presence of uncertainties. The accuracy of the solution approximation has been observed, and it was showed it depends on the order of polynomial expansion (see Table 5.2) and on the distance from the expansion point.

Due to the very large computational time required to run MC simulations with larger sample sizes (more than 10^8, 10^9, etc.), only a partial validation has been done up to the date on which this work is presented. Larger sample sizes would be required for a more complete and definitive validation of indirect DACE method.

It is worthy to be mentioned that several challenges have been faced to solve the CD&R OCP by indirect method. Any change in the model, in the dynamics, or

in the optimal control parameters, entails relevant modification of the theoretical formulation, and Euler-Lagrange equations have to be found again from scratch. Additionally, when stochasticity is introduced in the CD&R problem, the solution via indirect method becomes more complex. This is mainly due to fact that handling with integral cost terms involving PDF is in general not trivial. This aspect has been highlighted in the problem solved in Appendix A. Furthermore, the resulting costates and inequality constraint multipliers might not have a physical meaning, and they can be misleading or can be misinterpreted.

Despite of the above, this work achieved a satisfactory resolution of the stochastic CD&R OCP, providing tools for the collision risk analysis, such as, probability levels map (optimality map) and CA levels.

6.1   Problem Assumptions and Limitations

The assumptions of the problem, and the limitations of the method employed in this work can be mainly summarized as follow

- A bi-dimensional scenario has been considered, therefore obstacle modeling and avoidance trajectory have been very simple;

- Unicycle model and simple kinematics equations of motion have been employed for describing aircraft dynamics. As a consequence, the trajectories do not suffers of those holonomic constraints typical of more realistic aircraft dynamics (Dubins path);

- The optimal solution analytically obtained in Chapter 3 essentially represents the minimum length path between two waypoints, avoiding a circular fixed obstacle in the middle of this path. The problem, even if has been solved by a novel approach, still remains a simple problem which solution is well known.

- Trajectory collision probability computed in Chapter 4 can be also computed analytically, without using DACE.

- Introducing conflict probability as integral cost function through indirect methods has been very difficult. This is mainly due to the analytical manipulation needed for the solution of collision probability integral (see Equation (A.7) in

Appendix A). In general, stochastic OCP with conflict probability cost function are usually solved by direct approach relying on kriging and polynomial chaos expansion, as in [43, 44].

6.2   Future Research and Improvements

To pave the way for future research aligned with the aim of this dissertation, and to overcome the actual limitations of the method proposed, some future developments and improvements have been envisaged.

For instance, the objective of the CD&R OCP presented in Appendix A is to avoid a fixed obstacle in presence of spatial uncertainty, while minimizing a collision indicator set as Lagrangian cost term. As a result, the CD&R is treated as unconstrained OCP with cost function related to the probability to collide with the obstacle.

As additional research lines, the applicability of the method to multi-obstacle or multi-aircraft scenarios is straightforward, and at the expense of a very low computational cost. According to this idea, Appendix B presents an algorithm intended to solve conflicts between N aircraft in a 2D scenario, relying on small perturbation theory. Since this approach handles with several Taylor polynomials, it represents a very interesting and appealing starting point for DACE tool applications.

In Appendix C, the idea to employ indirect DACE approach to the case of moving obstacle is explored. Again, Euler-Lagrange equations have to be formulated from scratch, but the MPBVP is very similar to that treated Section 4.4. In case of moving obstacle, Hamiltonian function has an explicit dependence on time that could not be neglected, and Euler-Lagrange equations lead to different state and costates equations of motion. Additionally, deterministic predictions have to be conducted to find potential collision points with the moving obstacle, and this make more complex the introduction of stochastic variables. According to this view, moving obstacle can model weather hazards, aircraft, or other kinds of dynamic threats. Implementation done in this direction is, for example, the work presented in [96], where optimal trajectories in presence of stochastic meteorological adverse conditions have been found by direct collocation method. For a preliminary mathematical formulation of the moving obstacle CD&R problem, the interested reader is referred to Appendix C.

Beside the works mentioned above, during the development of this work other minor ideas have been standing out to improve the method proposed, and to see possible extensions of its applications. Some of those are briefly summarized as follow:

- Combining optimality levels and CA probability to analyze also trajectories with lower cost (lower ToF), and consequent higher collision risk.

- Complexity can be added to CD&R problem by employing more realistic aircraft models, including the aircraft speed as additional control, considering moving obstacle scenario, or extending the problem to various encountering aircraft scenarios.

- CA probability and optimality levels can be used to the define a time-base collision probability map, indicating the pilot what is the most probable (obstacle avoidance) vs. optimal (time of flight) maneuver at each time.

- Additional tests can be run to better estimate the quality of DACE PDF fitting distribution. As examples, T-student and Kolmogorov-Smirnov tests, or less powerful Chi-squared - Median test can be performed for MC results.

- From a mere computational point of view, alternative methods to increase MC sample sizes can be explored. This shall be done to observe clearer convergence of MC estimates to DACE results. A possible solution could rely on chunking the population by means of automatic parallelization.

- The accuracy of the solution map can be improved, and its domain expanded by using domain-splitting DACE built-in functions.

- The approach used to solve unconstrained stochastic problems in Appendix A can be fostered, and real collision probability values can be included as Lagrangian cost term of the OCP.

References

[1] SKYWAY magazine EUROCONTROL. Eurocontrol sits at the heart of regulatory, research and operational drone integration work, Feb 2018. [Online; accessed 07/02/2019].

[2] Xiang Yu and Youmin Zhang. Sense and avoid technologies with applications to unmanned aircraft systems: Review and prospects. *Progress in Aerospace Sciences*, 74:152–166, 2015.

[3] EASA. Concept of operations for drones a risk based approach to regulation of unmanned aircraft, May 2015. [Online; accessed 07/02/2019].

[4] Han-Lim Choi, Luc Brunet, and Jonathan P How. Consensus-based decentralized auctions for robust task allocation. *IEEE transactions on robotics*, 25(4):912–926, 2009.

[5] Randy Walter. Flight management systems. In *The Avionics Handbook*. CRC press Boca Raton, FL, 2001.

[6] D Hempe. Airworthiness approval of automatic dependent surveillance-broadcast (ads-b) out systems. *US Department of Transportation Federal Aviation Administration, AC-20-165*, 2010.

[7] Piero Miotto, Leena Singh, James D Paduano, Andrew Clare, Mary L Cummings, and Lesley A Weitz. Aircraft autonomy. In *Advances in Control System Technology for Aerospace Applications*, pages 81–107. Springer, 2016.

[8] Andrew Clare, Mary Cummings, and Luca Bertuccelli. Identifying suitable algorithms for human-computer collaborative scheduling of multiple unmanned vehicles. In *50th AIAA Aerospace Sciences Meeting including the New Horizons Forum and Aerospace Exposition*, page 485, 2012.

[9] FAA. Uas integration pilot program, Feb 2017. [Online; accessed 08/02/2019].

[10] A Zeitlin. Sense & avoid evaluations and standards for civil airspace access. *Unmanned aircraft systems, the global perspective*, 2008:156–157, 2007.

[11] James K Kuchar and Lee C Yang. A review of conflict detection and resolution modeling methods. *IEEE Transactions on intelligent transportation systems*, 1(4):179–189, 2000.

[12] Martín Campo and Francisco Javier. *The collision avoidance problem: Methods and algorithms*. PhD thesis, Universidad Rey Juan Carlos, 2010.

[13] Lucia Pallottino, Eric M Feron, and Antonio Bicchi. Conflict resolution problems for air traffic management systems solved with mixed integer programming. *IEEE transactions on intelligent transportation systems*, 3(1):3–11, 2002.

[14] Arthur Richards and Jonathan P How. Aircraft trajectory planning with collision avoidance using mixed integer linear programming. In *American Control Conference, 2002. Proceedings of the 2002*, volume 3, pages 1936–1941. IEEE, 2002.

[15] Emilio Frazzoli, Z-H Mao, J-H Oh, and E Feron. Resolution of conflicts involving many aircraft via semidefinite programming. *Journal of Guidance, Control, and Dynamics*, 24(1):79–86, 2001.

[16] Jérémy Omer. A space-discretized mixed-integer linear model for air-conflict resolution with speed and heading maneuvers. *Computers & Operations Research*, 58:75–86, 2015.

[17] Sonia Cafieri. Minlp in air traffic management: aircraft conflict avoidance. In *Advances and Trends in Optimization with Engineering Applications*. MOS-SIAM Book Series on Optimization, Philadelphia: SIAM, 2017.

[18] Sonia Cafieri and Riadh Omheni. Mixed-integer nonlinear programming for aircraft conflict avoidance by sequentially applying velocity and heading angle changes. *European Journal of Operational Research*, 260(1):283–290, 2017.

[19] David Rey, Christophe Rapine, Rémy Fondacci, and Nour-Eddin El Faouzi. Subliminal speed control in air traffic management: Optimization and simulation. *Transportation Science*, 50(1):240–262, 2016.

[20] Jing-Chao Chen. Dijkstra's shortest path algorithm. *Journal of Formalized Mathematics*, 15(9):237–247, 2003.

[21] Géraud Granger, Nicolas Durand, and Jean-Marc Alliot. Optimal resolution of en route conflicts. In *ATM 2001, 4th USA/Europe Air Traffic Management Research and Development Seminar*, 2001.

[22] Jayesh Amin, Jovan Boškovic, and Raman Mehra. A fast and efficient approach to path planning for unmanned vehicles. In *AIAA Guidance, Navigation, and Control Conference and Exhibit*, page 6103, 2006.

[23] Dominique Alejo, JA Cobano, G Heredia, and A Ollero. Particle swarm optimization for collision-free 4d trajectory planning in unmanned aerial vehicles. In *2013 International Conference on Unmanned Aircraft Systems (ICUAS)*, pages 298–307. IEEE, 2013.

[24] Mauro Pontani and Bruce A Conway. Particle swarm optimization applied to space trajectories. *Journal of Guidance, Control, and Dynamics*, 33(5):1429–1441, 2010.

[25] Nicolas Durand and Jean-Marc Alliot. Ant colony optimization for air traffic conflict resolution. In *ATM Seminar 2009, 8th USA/Europe Air Traffic Management Research and Developpment Seminar*, 2009.

[26] Robert Vivona, David Karr, and David Roscoe. Pattern-based genetic algorithm for airborne conflict resolution. In *AIAA Guidance, Navigation, and Control Conference and Exhibit*, page 6060, 2006.

[27] Gary B Lamont, James N Slear, and Kenneth Melendez. Uav swarm mission planning and routing using multi-objective evolutionary algorithms. In *Computational Intelligence in Multicriteria Decision Making, IEEE Symposium on*, pages 10–20. IEEE, 2007.

[28] John T Betts. *Practical methods for optimal control and estimation using nonlinear programming*, volume 19. Siam, 2010.

[29] Dimitri P Bertsekas. *Nonlinear programming*. Athena scientific Belmont, 1999.

[30] Pierre Bonami, Mustafa Kilinç, and Jeff Linderoth. Algorithms and software for convex mixed integer nonlinear programs. In *Mixed integer nonlinear programming*, pages 1–39. Springer, 2012.

[31] Michael R Bussieck and Stefan Vigerske. Minlp solver software, 2010.

[32] Daniele Giuseppe Mazzotta, Giuseppe Sirigu, Mario Cassaro, Manuela Battipede, and Piero Gili. 4d trajectory optimization satisfying waypoint and no-fly zone constraints. In *WSEAS Transactions on systems and control*, volume 12, pages 221–231, 2017.

[33] Manuel Soler, Alberto Olivares, and Ernesto Staffetti. Hybrid optimal control approach to commercial aircraft trajectory planning. *Journal of Guidance, Control, and Dynamics*, 33(3):985–991, 2010.

[34] Manuel Soler, Maryam Kamgarpour, Javier Lloret, and John Lygeros. A hybrid optimal control approach to fuel-efficient aircraft conflict avoidance. *IEEE Transactions on Intelligent Transportation Systems*, 17(7):1826–1838, 2016.

[35] Arthur Earl Bryson. *Applied optimal control: optimization, estimation and control*. CRC Press, 1975.

[36] Yoshinori Matsuno, Takeshi Tsuchiya, and Naoki Matayoshi. Near-optimal control for aircraft conflict resolution in the presence of uncertainty. *Journal of Guidance, Control, and Dynamics*, 39(2):326–338, 2015.

[37] Georgios Chaloulos and John Lygeros. Effect of wind correlation on aircraft conflict probability. *Journal of Guidance, Control, and Dynamics*, 30(6):1742–1752, 2007.

[38] Eulalia Hernández, Alfonso Valenzuela, and Damián Rivas. Probabilistic aircraft conflict detection considering ensemble weather forecast. *6th SESAR Innovation Days, the Netherlands*, 2016.

[39] Maria Prandini, Jianghai Hu, John Lygeros, and Shankar Sastry. A probabilistic approach to aircraft conflict detection. *IEEE Transactions on intelligent transportation systems*, 1(4):199–220, 2000.

[40] Selim Temizer, Mykel Kochenderfer, Leslie Kaelbling, Tomas Lozano-Pérez, and James Kuchar. Collision avoidance for unmanned aircraft using markov decision processes. In *AIAA guidance, navigation, and control conference*, page 8040, 2010.

[41] Andrea Lecchini Visintini, William Glover, John Lygeros, and Jan Maciejowski. Monte carlo optimization for conflict resolution in air traffic control. *IEEE Transactions on Intelligent Transportation Systems*, 7(4):470–482, 2006.

[42] N Kantas, A Lecchini-Visintini, and JM Maciejowski. Simulation-based bayesian optimal design of aircraft trajectories for air traffic management. *International Journal of Adaptive Control and Signal Processing*, 24(10):882–899, 2010.

[43] Roland Schöbi and Bruno Sudret. Combining polynomial chaos expansions and kriging for solving structural reliability problems. In *7th International Conference on Computational Stochastic Mechanics (CSM 7)*. ETH Zürich, 2014.

[44] Yoshinori Matsuno, Takeshi Tsuchiya, Jian Wei, Inseok Hwang, and Naoki Matayoshi. Stochastic optimal control for aircraft conflict resolution under wind uncertainty. *Aerospace Science and Technology*, 43:77–88, 2015.

[45] Yoshinori Matsuno and Takeshi Tsuchiya. Probabilistic conflict detection in the presence of uncertainty. In *Air traffic management and systems*, pages 17–33. Springer, 2014.

[46] Robert R. Bless and Dewey H. Hodges. A finite element method for the solution of optimal control problems. In C.T. Leondes, editor, *Discrete-Time Control System Implementation Techniques*, volume 72 of *Control and Dynamic Systems*, pages 183 – 263. Academic Press, 1995.

[47] Olivier Cots, Joseph Gergaud, and Damien Goubinat. Direct and indirect methods in optimal control with state constraints and the climbing trajectory of an aircraft. *Optimal Control Applications and Methods*, 39(1):281–301, 2018.

[48] Robert R Bless, Dewey H Hodges, and Hans Seywald. Finite element method for the solution of state-constrained optimal control problems. *Journal of Guidance, Control, and Dynamics*, 18(5):1036–1043, 1995.

[49] William E Wiesel. *Modern Astrodynamics*, volume 2652. Aphelion Press Beavercreek, OH, 2010.

[50] ICAO. Amendment 43 to annex 2 'rules of the air' - appendix 4 - remotely piloted aircraft systems.

[51] J Lai, JJ Ford, L Mejias, P O'Shea, and R Walker. See and avoid using onboard computer vision, sense and avoid in uas research and applications, plamen angelov, 2012.

[52] Andrew D Zeitlin and Michael P McLaughlin. Safety of cooperative collision avoidance for unmanned aircraft. In *25th Digital Avionics Systems Conference, 2006 IEEE/AIAA*, pages 1–7. IEEE, 2006.

[53] Luis Mejias, John Lai, and Troy Bruggemann. Sensors for missions. In *Handbook of Unmanned Aerial Vehicles*, pages 385–399. Springer, 2015.

[54] Thomas B Billingsley, Mykel J Kochenderfer, and James P Chryssanthacopoulos. Collision avoidance for general aviation. *IEEE Aerospace and Electronic Systems Magazine*, 27(7):4–12, 2012.

[55] Edward Valovage. Enhanced ads-b research. In *25th Digital Avionics Systems Conference, 2006 IEEE/AIAA*, pages 1–7. IEEE, 2006.

[56] Ultra lightweight low cost ads-b transponder for uas. https://uavionix.com/news/ultra-lightweight-low-cost-ads-b-transponder-for-uas/. [Online; accessed 17-October-2018].

[57] Navworx ads600-b. https://www.seaerospace.com/sales/product/NavWorx/ADS600-B. [Online; accessed 17-October-2018].

[58] Google targets low-cost ads-b out avionics market. https://www.flightglobal.com/news/articles/google-targets-low-cost-ads-b-out-avionics-market-410473/. [Online; accessed 17-October-2018].

[59] Scaneagle uav gets synthetic aperture radar (sar). https://newatlas.com/scaneagle-uav-gets-synthetic-aperture-radar-sar/9007/. [Online; accessed 17-October-2018].

[60] Paul A Rosen, Scott Hensley, Kevin Wheeler, Greg Sadowy, Tim Miller, Scott Shaffer, Ron Muellerschoen, Cathleen Jones, Soren Madsen, and Howard Zebker. Uavsar: New nasa airborne sar system for research. *IEEE Aerospace and Electronic Systems Magazine*, 22(11):21–28, 2007.

[61] Allistair Moses, Matthew J Rutherford, and Kimon P Valavanis. Radar-based detection and identification for miniature air vehicles. In *Control Applications (CCA), 2011 IEEE International Conference on*, pages 933–940. IEEE, 2011.

[62] Rps delivers a range of lidar, uav and traditional aerial photography and photogrammetry services. https://www.rpsgroup.com/Australia-Asia-Pacific/Services/Surveying-Mapping/LiDAR,-Aerial-Photography-and-Photogrammetry.aspx. [Online; accessed 17-October-2018].

[63] Riegl uav laser scanning. https://www.3dlasermapping.com/riegl-uav-laser-scanners/. [Online; accessed 17-October-2018].

[64] Yi Lin, Juha Hyyppa, and Anttoni Jaakkola. Mini-uav-borne lidar for fine-scale mapping. *IEEE Geoscience and Remote Sensing Letters*, 8(3):426–430, 2011.

[65] Ibeo automotive lidar. http://www.ibeo-as.com/aboutibeo/lidar/. [Online; accessed 17-October-2018].

[66] Roberto Sabatini, Alessandro Gardi, Subramanian Ramasamy, and Mark A Richardson. A laser obstacle warning and avoidance system for manned and unmanned aircraft. In *Metrology for Aerospace (MetroAeroSpace), 2014 IEEE*, pages 616–621. IEEE, 2014.

[67] Brian C Karhoff, Jason I Limb, Shane W Oravsky, and Alfred D Shephard. Eyes in the domestic sky: an assessment of sense and avoid technology for the army's" warrior" unmanned aerial vehicle. In *Systems and Information Engineering Design Symposium, 2006 IEEE*, pages 36–42. IEEE, 2006.

[68] John Lai, Luis Mejias, and Jason J Ford. Airborne vision-based collision-detection system. *Journal of Field Robotics*, 28(2):137–157, 2011.

[69] John McCalmont, James Utt, Michael Deschenes, and Michael Taylor. Sense and avoid, phase i (man-in-the-loop) advanced technology demonstration. In *Infotech@ Aerospace*, page 7176. 2005.

[70] Thales fulmar x. https://www.thalesgroup.com/en/fulmar-x. [Online; accessed 17-October-2018].

[71] Cyrus Minwalla, Paul Thomas, Kristopher Ellis, Richard Hornsey, and Sion Jennings. Flight test evaluation of a prototype optical instrument for airborne sense-and-avoid applications. In *Unmanned Systems Technology XIV*, volume 8387, page 83870R. International Society for Optics and Photonics, 2012.

[72] Hu Sheng, Haiyang Chao, Cal Coopmans, Jinlu Han, Mac McKee, and YangQuan Chen. Low-cost uav-based thermal infrared remote sensing: Platform, calibration and applications. In *Mechatronics and Embedded Systems and Applications (MESA), 2010 IEEE/ASME International Conference on*, pages 38–43. IEEE, 2010.

[73] RW Osborne, Yaakov Bar-Shalom, Peter Willett, and G Baker. Design of an adaptive passive collision warning system for uavs. *IEEE Transactions on Aerospace and Electronic Systems*, 47(3):2169–2189, 2011.

[74] Subramanian Ramasamy and Roberto Sabatini. A unified approach to cooperative and non-cooperative sense-and-avoid. In *Unmanned Aircraft Systems (ICUAS), 2015 International Conference on*, pages 765–773. IEEE, 2015.

[75] Uav acoustic collision-alert system from sara. https://www.suasnews.com/2010/10/uav-acoustic-collision-alert-system-from-sara/. [Online; accessed 17-October-2018].

[76] Anthony Finn and Stephen Franklin. Acoustic sense & avoid for uav's. In *Intelligent Sensors, Sensor Networks and Information Processing (ISSNIP), 2011 Seventh International Conference on*, pages 586–589. IEEE, 2011.

[77] D Gottlieb, MY Hussaini, and SA Orszag. Theory and applications of spectral methods spectral methods for partial differential equations eds rg voigt. *D Gottlieb and MY Hussainni (Philadelphia, PA: SIAM) p*, 1, 1984.

[78] Charles R Hargraves and Stephen W Paris. Direct trajectory optimization using nonlinear programming and collocation. *Journal of Guidance, Control, and Dynamics*, 10(4):338–342, 1987.

[79] JV Villadsen and WE Stewart. Solution of boundary-value problems by orthogonal collocation. *Chemical Engineering Science*, 22(11):1483–1501, 1967.

[80] Carl De Boor and Blâir Swartz. Collocation at gaussian points. *SIAM Journal on Numerical Analysis*, 10(4):582–606, 1973.

[81] Kouamana Bousson and Paulo Machado. 4d flight trajectory optimization based on pseudospectral methods. *World Academy of Science, Engineering and Technology*, 70:551–557, 2010.

[82] Manuel Soler. *Comercial aircraft trajectory planning based on multiphase mixed-integer optimal control.* Omm Editorial, 2013.

[83] Izrail Moiseevitch Gelfand, Richard A Silverman, et al. *Calculus of variations*. Courier Corporation, 2000.

[84] David H Jacobson, Milind M Lele, and Jason L Speyer. New necessary conditions of optimality for control problems with state-variable inequality constraints. 1969.

[85] Hans Seywald and Eugene M Cliff. Short communications on the existence of touch points for first-order state inequality constraints. *Optimal Control Applications and Methods*, 17(5):357–366, 1996.

[86] Arthur E Bryson, Walter F Denham, and Stewart E Dreyfus. Optimal programming problems with inequality constraints. *AIAA journal*, 1(11):2544–2550, 1963.

[87] M Valli, R Armellin, P Di Lizia, and MR Lavagna. Nonlinear mapping of uncertainties in celestial mechanics. *Journal of Guidance, Control, and Dynamics*, 36(1):48–63, 2012.

[88] Kyoko Makino and Martin Berz. Cosy infinity version 9. *Nuclear Instruments and Methods in Physics Research Section A: Accelerators, Spectrometers, Detectors and Associated Equipment*, 558(1):346–350, 2006.

[89] Roberto Armellin, Pierluigi Di Lizia, Franco Bernelli-Zazzera, and M Berz. Asteroid close encounters characterization using differential algebra: the case of apophis. *Celestial Mechanics and Dynamical Astronomy*, 107(4):451–470, 2010.

[90] Mercier-P. Azzopardi V. Bignon, E. and R. Pinède. Accurate numerical orbit propagation using polynomial algebra computational engine pace. In *ISSFD 2015 congress*, 2015.

[91] Daniel Pérez-Palau, Josep J Masdemont, and Gerard Gómez. Tools to detect structures in dynamical systems using jet transport. *Celestial mechanics and dynamical astronomy*, 123(3):239–262, 2015.

[92] Alberto Abad, Roberto Barrio, Fernando Blesa, and Marcos Rodríguez. Algorithm 924: Tides, a taylor series integrator for differential equations. *ACM Transactions on Mathematical Software (TOMS)*, 39(1):5, 2012.

[93] Alexander Wittig, Pierluigi Di Lizia, and Roberto Armellin. From particle accelerators to celestial dynamics: An introduction to differential algebra. *Key Topics in Orbit Propagation Applied to Space Situational Awareness*, page 57, 2014.

[94] Roberto Armellin and Pierluigi Di Lizia. Probabilistic initial orbit determination. In *Proceedings of the 26th AAS/AIAA Space Flight Mechanics Meeting held February 14–18, 2016, Napa, California, USA*, pages 1–17, 2016.

[95] Bin Wang, Wenzhong Shi, and Zelang Miao. Confidence analysis of standard deviational ellipse and its extension into higher dimensional euclidean space. *PloS one*, 10(3):e0118537, 2015.

[96] Manuel Sanjurjo. D. González-Arribas, Manuel Soler. Wind-based robust aircraft route optimization using meteorological ensemble prediction systems. In *proceedings of SESAR Innovation Days 2016 (SIDs'16)*. Eurocontrol, D. Shaefer (Ed.). ISSN 0770-1268. pp. 1-8., 2016.

Published and Submitted Articles, and Contributions

1. B.A.E. Lehner, J.Schlechten, A. Filosa, A.C. Pou, D.G. Mazzotta, F. Spina, L. Teeney, J. Snyder, S.Y. Tjon, A.S. Meyer, S.J.J. Brouns, A. Cowley and L.J. Rothschild, End-to-end mission design for microbial ISRU activities as preparation for a moon village, *Acta Astronautica* (2019).

2. B.A.E. Lehner, J. Schlechten, A. Filosa, A. Canals Pou, D. G. Mazzotta, F. Spina, L. Teeney, J. Snyder, S.Tjorn, S. Brouns, L. Rothschild, A. Cowley, End-to-End Mission Design for Microbial Isru Activities as Preparation for a Moon Village, IAC-18,A3,2C,6,x42648, *69th International Astronautical Congress*, Bremen, Germany, 2018, 1-5 October

3. A.E.M. Casini, A. Cowley, D.G Mazzotta, P. Maggiore, N. Viola, A Virtual Reality approach for studying a future human lunar outpost: an integrated simulation case study of a Stand Alone Power System, *68th International Astronautical Congress*, Adelaide, Australia, 2017, 25-29 September 2017.

4. B.A.E. Lehner, D. G. Mazzotta., L. Teeney, F. Spina, A. Filosa, A. Pou Canals, J. Schlechten, S. Campbell, P. Soriano López, Human Assisted Robotic Vehicle Studies - a conceptual end-to-end mission architecture, *Acta Astronautica* (2017).

5. D.G. Mazzotta, G. Sirigu, M. Cassaro, M. Battipede, P. Gili, 4D Trajectory Optimization Satisfying Waypoint and No-Fly Zone Constraints, *Wseas Transactions on Systems and Control*, Vol. 12 (2017): 171-231.

6. B. Lehner, D. G. Mazzotta, L. Teeney, F. Spina, A. Filosa, A. Canals Pou, J. Schlechteng, P. López Soriano, Human Assisted Robotic Vehicle Studies - a conceptual end-to-end mission architecture, IAC-16.A3.2C.3, *67th International Astronautical Congress*, Guadalajara, Mexico, 2016, 26-30 September.

7. A. E. M. Casini, D. G. Mazzotta, P. Maggiore, N. Viola, V. Basso, M. Ferrino, J. A. Hoffman, A. Cowley, Analysis of a Moon outpost for Mars enabling technologies through a Virtual Reality environment, IAC-16.A3.2C.5, *67th International Astronautical Congress*, Guadalajara, Mexico, 2016, 26-30 September.

8. D.G. Mazzotta, Guidance Navigation and Control Techniques for 4D Trajectory Optimization Satisfying Waypoint and No-Fly Zone Constraints, *12th Pegasus-AIAA Student Conference*, Valencia, Spain, 2016, 20-17 April.

Appendix A

Unconstrained Stochastic OCP Solved via Indirect Method

In this section, the results of a CD&R problem between a vehicle and a stochastic obstacle are presented. The obstacle is assumed to be affected by uncertainty on its center position, and the problem is formulated as OCP and solved via indirect method. The objective of the OCP is to lead the aircraft from initial to final waypoint by varying only its heading angle, while minimizing a collision indicator related to the probability to collide with the obstacle. As a result, the path constraint related to the obstacle disappears, and the CD&R problem becomes an unconstrained stochastic OCP. It is expected that optimal solution is just an unconstrained arc leading the aircraft from initial to final waypoint, meeting the necessary conditions of optimality expressed by the indirect method and minimizing the collision probability indicator.

States and Control Variables

For the stochastic OCP presented here, the vectors of states $\boldsymbol{x}$ and controls $\boldsymbol{u}$ are defined as

$$\boldsymbol{x}(t) = \begin{bmatrix} x(t) \\ y(t) \end{bmatrix} \tag{A.1}$$

$$\boldsymbol{u}(t) = \chi(t) \tag{A.2}$$

where $x(t)$, $y(t)$ are the Cartesian coordinates of the aircraft in a 2D plane, and $\chi \in [-\pi, \pi]$ is the heading angle control. Unicycle model is employed for vehicle dynamics therefore, the equations of motion becomes pure kinematics as

$$\boldsymbol{f}\left[\boldsymbol{x}(t), \boldsymbol{u}(t)\right] = \dot{\boldsymbol{x}}(t) = \begin{bmatrix} V\cos\chi(t) \\ V\sin\chi(t) \end{bmatrix} \tag{A.3}$$

and aircraft true airspeed V is assumed to be constant.

Obstacle Uncertainty Propagation

The information about the position of the obstacle center is assumed to be provided by a sensing platform on-board the aircraft affected by measurement errors. As a consequence, the coordinates of the obstacle $C(x_C, y_C)$ are supposed to be affected by uncertainty, and characterized by a Gaussian normal Probability Density Function (PDF) of the form

$$p_{\mathbf{X}_C}(x_C, y_C) = \frac{1}{2\pi\sigma_{x_C}\sigma_{y_C}} \exp\left(-\frac{(x_C - \mu_{x_C})^2}{2\sigma_{x_C}^2} - \frac{(y_C - \mu_{y_C})^2}{2\sigma_{y_C}^2}\right) \tag{A.4}$$

or, in symbols, $\mathbf{X}_C \sim \mathcal{N}(\boldsymbol{\mu}, \boldsymbol{\Sigma})$, where $\boldsymbol{\mu} = (\mu_{x_C}, \mu_{y_C})$ is the expected sensed value, and $\boldsymbol{\Sigma}$ is a diagonal covariance matrix defined by the standard deviations σ_{x_C} and σ_{y_C}. Once the analytic expression of obstacle position uncertainty is known, the consecutive step is to determine a collision probability indicator associated with each point of the airspace surrounding the obstacle. With regards to Figure A.1, $P(x^*, y^*)$ is a generic point of the optimal trajectory Ω^*, and Γ refers to the prescribed minimum separation distance to be maintained between vehicle and obstacle.
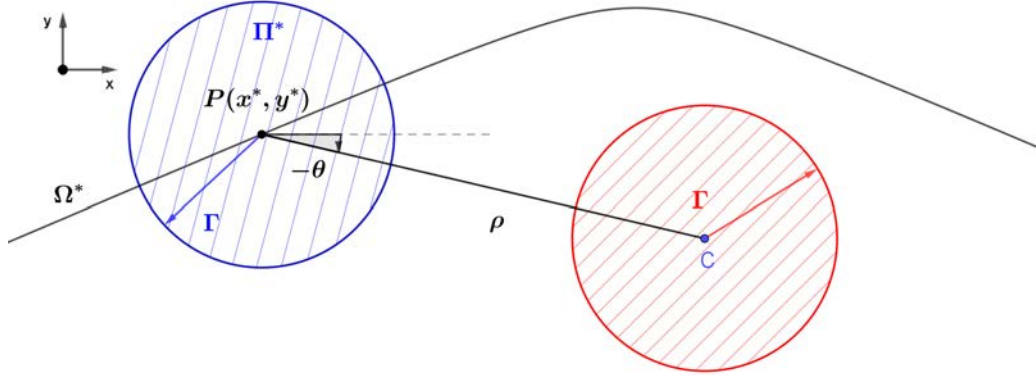
Figure A.1: Schematic representation of polar reference frame, for collision risk indicator calculation.

A new polar reference frame carried by a generic point of the optimal trajectory is represented in Fig. A.1. The stochastic variable $\mathbf{X}_C$ can be therefore expressed by the coordinates transformation

$$\mathbf{g}(x^*, y^*, \rho, \theta) = \begin{bmatrix} x_C = x^* + \rho \cos\theta \\ y_C = y^* + \rho \sin\theta \end{bmatrix} \tag{A.5}$$

Using the axiom of probability conservation, and the rules of change of variables in multiple integrals, the probability density function of $\mathbf{X_c}$ can be written as

$$p_{\mathbf{X}_C}(x^*, y^*, \rho, \theta) = p_{\mathbf{X}_C}[\mathbf{g}(x^*, y^*, \rho, \theta)] \left| \det \mathbf{J_g} \right| \tag{A.6}$$

where $\mathbf{J_g}$ is the Jacobian matrix of the transformation $\mathbf{g}$. The collision risk probability indicator for the generic point $P(x^*, y^*)$, which is related to probability that the distance between the point $P(x^*, y^*)$ and the center of the obstacle is less or equal to Γ, is represented by the marginal PDF $P_{CRP} : \mathbb{R}^2 \mapsto \mathbb{R}$ defined as

$$P_{CRP}(x^*, y^*) = P(\mathbf{X}_C \in \Pi^*) = \int_0^\Gamma \int_0^{2\pi} p_{\mathbf{X}_C}(x^*, y^*, \rho, \theta) d\theta d\rho \tag{A.7}$$

It can be observed that, for each point $P(x^*, y^*)$ of the optimal trajectory, conflict occurs if and only if the obstacle center is within the circular region Π^* centered in P of radius Γ as showed in Fig. A.1.

Indirect Approach

The collision probability indicator $P_{CRP}(x,y)$ of Equation. (A.7) is adjoined to the cost function J as

$$J = \int_{t_0^+}^{t_f^-} \left[w + P_{CRP}(x,y) \right] dt \tag{A.8}$$

In this manner, J assumes a Lagrangian fashion, formed by the time of flight term penalized by the weight $w \in \mathbb{R}^+$, and the collision probability indicator P_{CRP} integrated by time. As a consequence, it is expected that as w grows the OCP tends to maintain the time of flight of the mission as low as possible. In this case, the solution trajectory is expected to be a straight line linking the initial with the final waypoint. On the other hand, when w is close to zero the aircraft tries to stay as far as possible from the obstacle minimizing the collision indicator, regardless of the time of flight.

Since the solution of the integral in Equation (A.7) is not trivial, to adjoin the probability indicator (or marginal PDF) P_{CRP} to the problem cost function of Equation (A.8), two main approaches were attempted. According to the first intent, integral in Equation (A.7) was approximated by employing DA Taylor polynomials. In this manner, two main issues were observed: indirect methods cannot handle in general with empirical models where function values has to be extracted from interpolation of tabular data [28]; on the other hand, DA polynomials diverges rapidly around the origin point of the expansion. The second approach consisted in assuming that P_{PCRP} still follows a Normal Gaussian distribution as in Equation (A.4). This last approach was chosen for the simulation presented in this section.

Employing Equation (A.8) in Equation (3.25), Hamiltonian function becomes

$$H(\boldsymbol{x}, \boldsymbol{\lambda}, \boldsymbol{u}, t) = w + P_{CRP} + \boldsymbol{\lambda}^T \boldsymbol{f} \tag{A.9}$$

and the Euler-Lagrange Equations (3.32) - (3.34) result in

$$\begin{aligned} \dot{\boldsymbol{x}} &= \boldsymbol{f} \\ \dot{\boldsymbol{\lambda}} &= -\frac{\partial P_{CRP}}{\partial \boldsymbol{x}} \end{aligned} \tag{A.10}$$

with the algebraic equation

$$\boldsymbol{\lambda}^T \frac{\partial \boldsymbol{f}}{\partial \boldsymbol{u}} = 0 \tag{A.11}$$

and boundary conditions

$$\boldsymbol{x}(t_0) = O(x_O, y_O) \tag{A.12}$$

$$\boldsymbol{x}(t_f) = F(x_f, y_f) \tag{A.13}$$

$$\boldsymbol{\lambda}(t_0) = \boldsymbol{\nu}_0 \tag{A.14}$$

$$\boldsymbol{\lambda}(t_f) = \boldsymbol{\nu}_f \tag{A.15}$$

$$H(t_f) = 0 \tag{A.16}$$

where O and F are the initial and final waypoints, respectively, and $\boldsymbol{\nu}_0$ and $\boldsymbol{\nu}_f$ two vectors of constants.

Collision Probability Indicator vs. Collision Probability

The term $P_{CRP(x,y)}$ integrated by time in Equation (A.8) is not really a collision probability, instead, it is an indicator of collision probability certainly related to the real probability of collision. In order to show how to compute the probability of a collision with a generic stochastic obstacle, the trajectory depicted in Fig. A.2 is considered.

In order to know the probability of such trajectory of colliding with the obstacle, namely the collision risk probability, the PDF associated to the stochastic variable $\mathbf{X}_C$ has to be integrated over the region Π defined by the points $O_-O_+A_+B_+F_+F_-C$. Indeed, it can be observed that conflict occurs if and only if the obstacle center is within the region Π, otherwise the trajectory is conflict free. In mathematical terms, the probability of collision P_C can be calculated as

$$P_C = P(\mathbf{X}_C \in \Pi) = \int\int_\Pi p_{\mathbf{X}_C}(x_C, y_C)dxdy \tag{A.17}$$

As a consequence, the region Π will depend on the path of the optimal trajectory, and its shape will be varying according to the position of the obstacle.
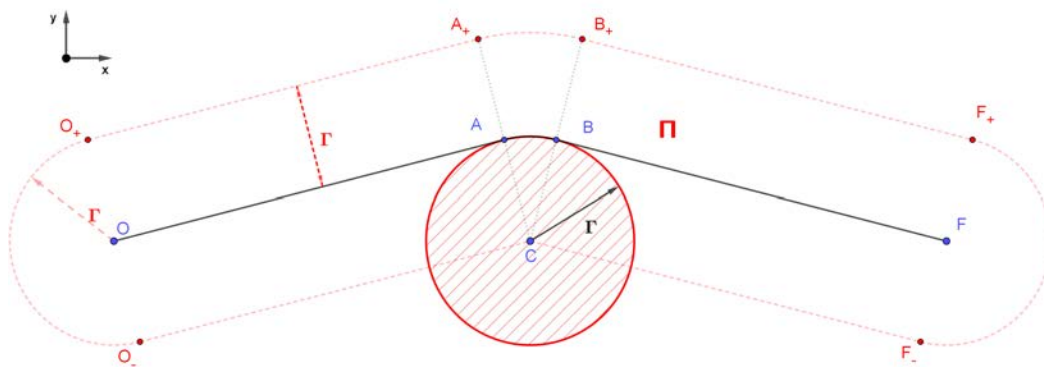
Figure A.2: Schematic representation of trajectory envelope for collision probability calculation.

Results

The results of the stochastic CD&R problem solved via indirect method are presented here. The simulations were performed on a Windows 64-bit system with two Intel Cores i7 of 2GHz and 8GB RAM. Figure A.3 represents the surface and relative iso-lines of Gaussian P_{CRP}. Normalized boundary conditions, and scenario set-up are gathered in Table A.1 and Table A.2, respectively. For the nondimensionalization of coordinates and velocity, the maximum Cartesian coordinate x and the aircraft V_{TAS} were used, respectively. Several solutions were found by varying the weights w from 0.1 to 6 by steps of 0.1. The value of the objective function J, the time of flight tf, the collision risk probability indicator $\int_0^{t_f} P_{CRP} dt$, and the computational time for $w = 0.1, 6$ simulations are showed in Table A.3. Figure A.4 shows the optimal trajectories obtained for different weight values. As expected, as w grows, trajectory tends to minimize the time of flight increasing the risk of collision, and vice versa. Figures A.5 and A.6 shows the trends of controls and costates, respectively. Similarly, A.7 represents the punctual values of $P_{CRP}(x, y)$ along trajectories. Figure A.8 is a canonical Pareto chart comparing the two cost functional terms with respect to the variation of the weight w. Finally, A.9 shows the trend of the cost function J as function of the weight w.
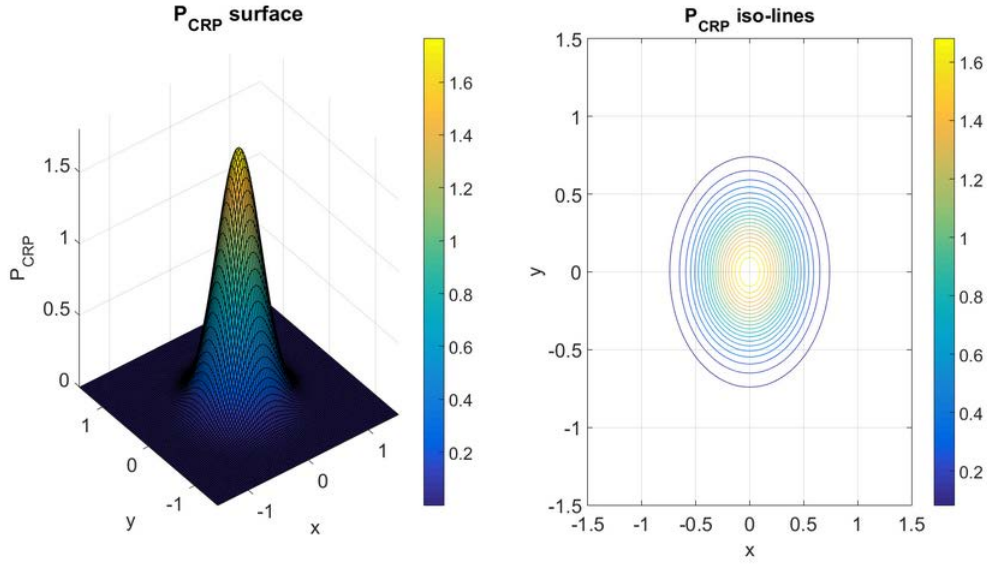
Figure A.3: Normal Gaussian P_{CRP} surface(left) and iso-lines(right).

Table A.1: Aircraft boundary conditions - Unconstrained OCP case study.

x_0	y_0	x_f	y_f	V
-1	-1	1	1	1

Table A.2: Scenario set-up data - Unconstrained OCP case study.

μ_{xc}	μ_{yc}	σ_{xc}	σ_{yc}
0	0	0.3	0.3

Table A.3: Simulation results - Unconstrained OCP case study.

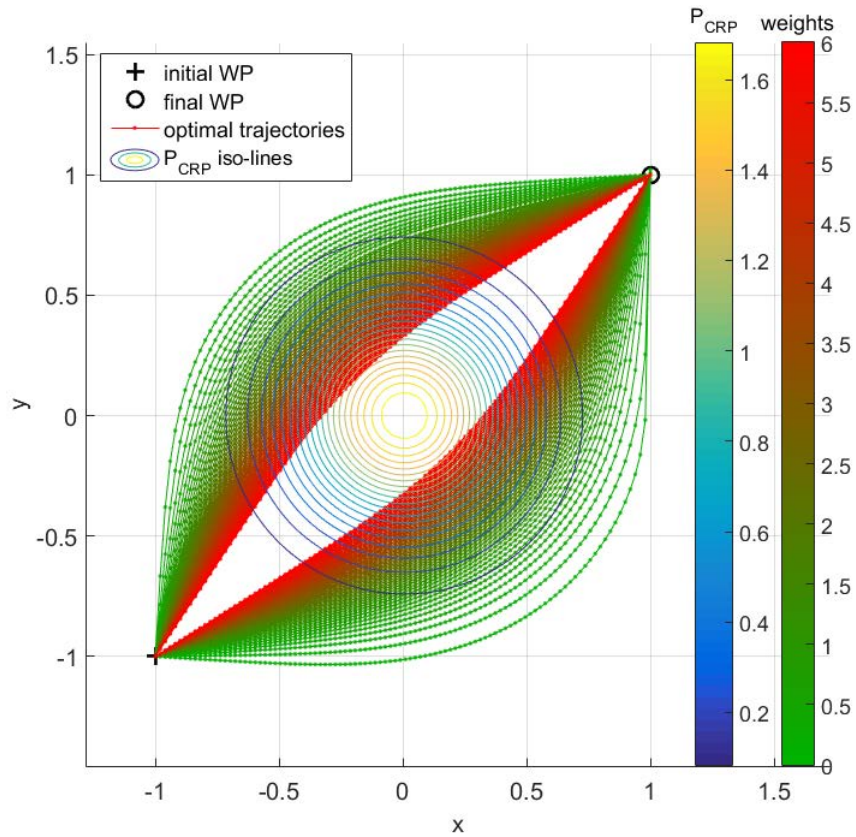| w	t_f[s]	$\int_0^{t_f} P_{CRP}dt$[s]	J[s]	CPU time [s]
0.1	3.558	0.02	0.376	0.46
⋮	⋮	⋮	⋮	⋮
6	2.875	1.01	18.26	0.46

Figure A.4: Optimal trajectories for $w = \{0.1 : 0.1 : 6\}$ - Unconstrained Stochastic OCP case study.
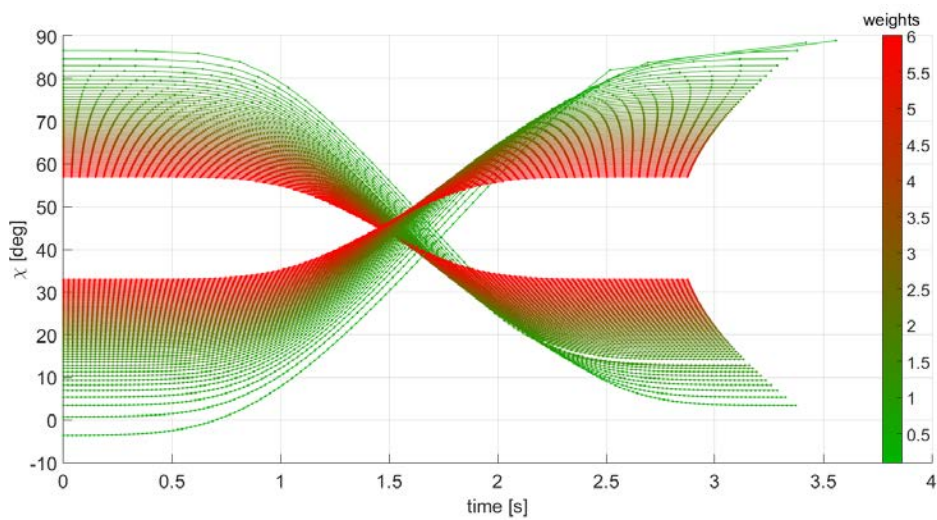

Figure A.5: Controls time history for $w = \{0.1 : 0.1 : 6\}$ - Unconstrained Stochastic OCP case study.
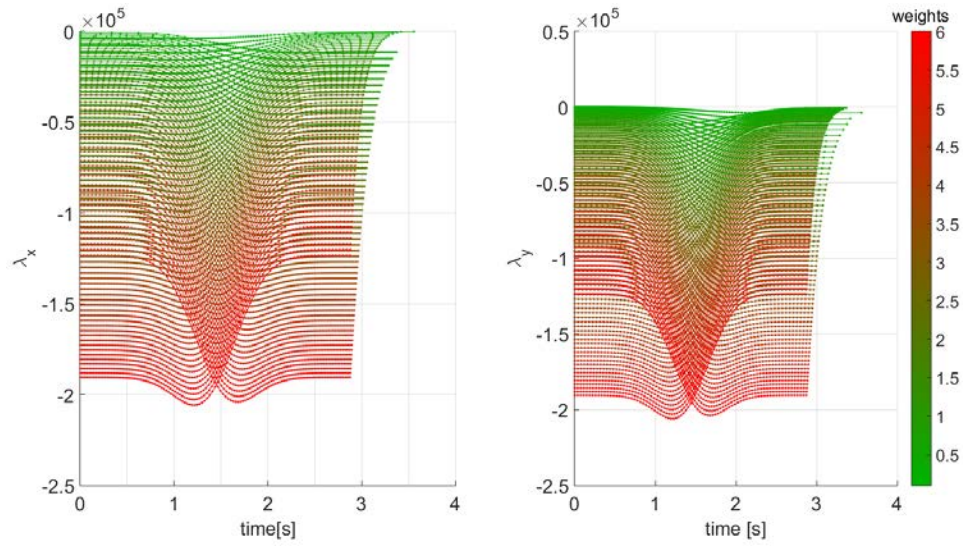
Figure A.6: Costates time history for $w = \{0.1 : 0.1 : 6\}$ - Unconstrained Stochastic OCP case study.
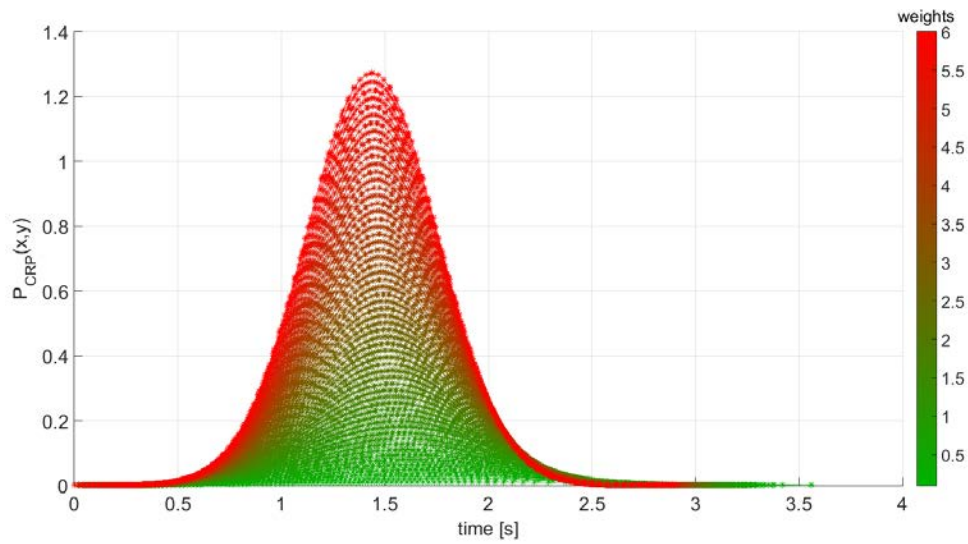

Figure A.7: Collision probability indicator for $w = \{0.1 : 0.1 : 6\}$ - Unconstrained Stochastic OCP case study.
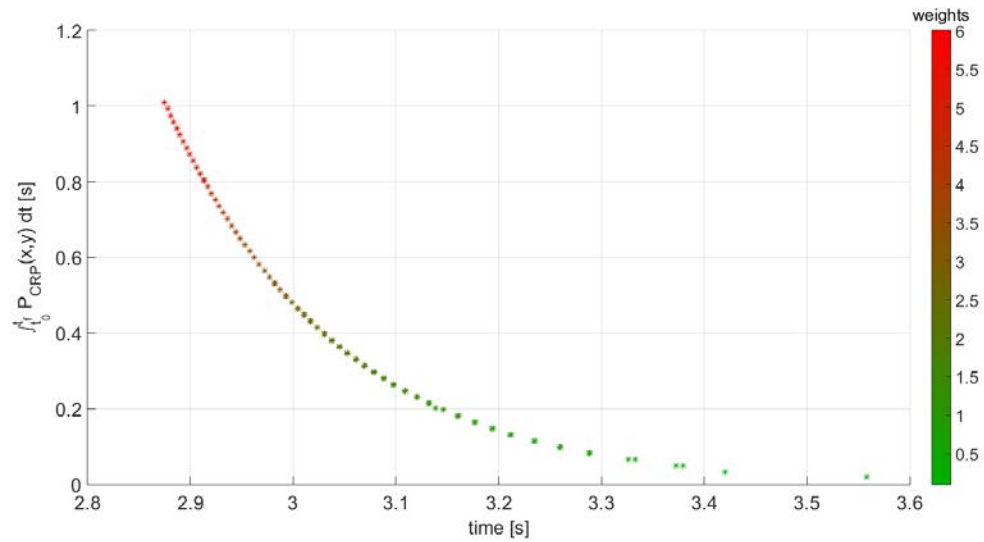
Figure A.8: Pareto chart of collision probability indicator cost term vs. time of flight for $w = \{0.1 : 0.1 : 6\}$ - Unconstrained Stochastic OCP case study .
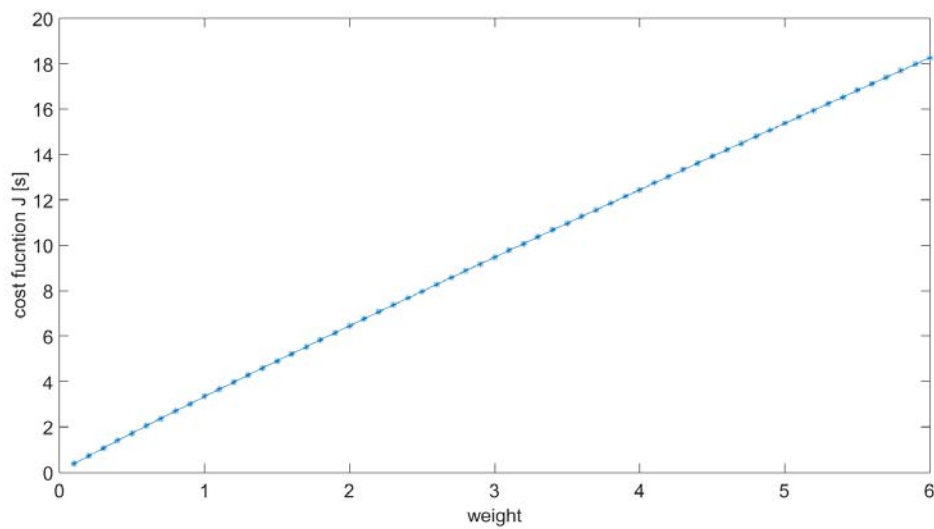

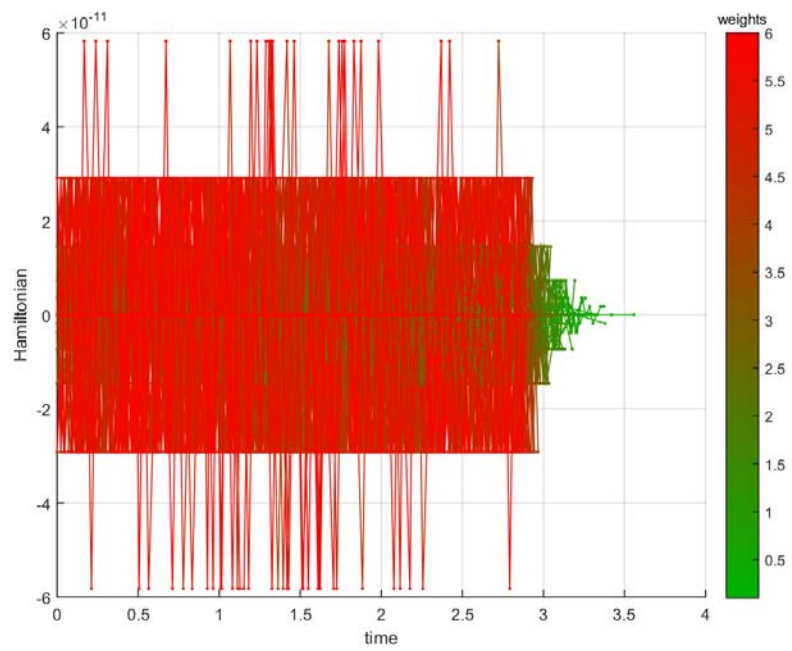Figure A.9: Cost function for $w = \{0.1 : 0.1 : 6\}$ - Unconstrained Stochastic OCP case study.

Figure A.10: Hamiltonian function for $w = \{0.1 : 0.1 : 6\}$ - Unconstrained Stochastic OCP case study.

Appendix B

Small Perturbation Method for Multiple-Aircraft OCP

B.1 Description of the Problem

The algorithm presented is intended to solve conflicts between N aircraft in a 2D scenario, providing optimal trajectory in terms of minimum flight time. Aircraft positions are identified by Cartesian coordinates $x(t), y(t)$ in the plane, and aircraft dynamics is described by two kinematic equations. Moreover, up to the date this work is presented, the control variable chosen to address conflict-free maneuver is the aircraft heading angle $\chi(t)$. Further developments might also include aircraft speed $V(t)$ as control variable.

B.2 Methodology

The method consists in developing a new strategy to formulate and solve the collision avoidance problem by applying an approximation scheme to the optimal dual problem (Euler-Lagrange equations). The approximation scheme is based on the perturbation theory, a method commonly used to solve ordinary differential equations. In particular, the algorithm consists in formulating the Hamiltonian MPVB, i.e., the necessary conditions for the optimality (Pontryagin Maximum Principle),

perturbating the solution, and then solving the problem numerically or by using DACE.

The perturbation parameter chosen in this problem is the minimum lateral separation that has be maintained between aircraft, namely Γ. This choice is supported by the fact that, if a conflict occurs in a 2D plane, this involves a region of the airspace which is very small compared to the characteristic length of the domain, i.e., the airspace dimension, or the aircraft route lengths. In other words, except for the region close to the conflict, aircraft trajectories are essentially straight lines. Close to the region of conflict, free-conflict solution can be approximated as Taylor expansion in Γ. If the conflict is not solved expanding the solution at a fixed order, successive terms of the expansion are needed to achieve free-conflict maneuvers. Eventually, the steps of the perturbation method applied to the conflict avoidance problem can be summarized as follow:

1. Find the necessary conditions of optimality;

2. Set $\Gamma = 0$, and solve the resulting system (zero-order solution);

3. Perturb the system by allowing Γ to be nonzero (but very small when compared to the domain dimension);

4. Formulate the solution to the perturbed system as a series

$$x(t) = x(t)^{(0)} + \Gamma x(t)^{(1)} + \Gamma^2 x(t)^{(2)} + \ldots + \Gamma^k x(t)^{(k)} + \mathscr{O}(\Gamma^k) \qquad \text{(B.1)}$$

5. Approximate the governing equations expanding as a series in Γ, collect the terms with equal powers of Γ, and solve each term until conflict free maneuvers are obtained for all aircraft;

6. Employ DACE as in Section 4.7 for solving optimality implicit equations truncated at each order k.

B.3   Problem Statement

Let consider N aircraft entering in a 2D sector of the airspace. Let define the vector of state variables $X(t)$, the vector of controls $u(t)$, and the system dynamics equations vector $f(u)$ as

$$X_i = \begin{bmatrix} x_i \\ y_i \end{bmatrix} \qquad i = 1,\dots,N \quad X \in \mathbb{R}^{2N\times 1} \qquad \text{(B.2)}$$

$$u_i = \chi_i \qquad i = 1,\dots,N \quad u \in \mathbb{R}^{N\times 1} \qquad \text{(B.3)}$$

$$f_i = \dot{X}_i = \begin{bmatrix} V_i \cos \chi_i \\ V_i \sin \chi_i \end{bmatrix} \qquad i = 1,\dots,N \quad f \in \mathbb{R}^{2N\times 1} \qquad \text{(B.4)}$$

It is supposed that initial and final position are known, i.e.:

$$X_i(t_0) = \begin{bmatrix} x_i(t_0) \\ y_i(t_0) \end{bmatrix} = \begin{bmatrix} x_{0,i} \\ y_{0,i} \end{bmatrix} \qquad i = 1,\dots,N \qquad \text{(B.5)}$$

$$X_i(t_f) = \begin{bmatrix} x_i(t_f) \\ y_i(t_f) \end{bmatrix} = \begin{bmatrix} x_{f,i} \\ y_{f,i} \end{bmatrix} \qquad i = 1,\dots,N \qquad \text{(B.6)}$$

and exit and entering time are also fixed and common to all aircraft (at this step of the development). Let define the vector of conflict avoidance constraints $C(x_j, x_i, y_j, y_i)$ as

$$C_{ij} = \Gamma \left(1 - \sqrt{\frac{(x_j - x_i)^2}{\Gamma^2} + \frac{(y_j - y_i)^2}{\Gamma^2}} \right) \le 0 \quad i = 1,\dots,N \ j = i+1,..,N \quad C \in \mathbb{R}^{d\times 1}$$

$$\text{(B.7)}$$

where d is the number of aircraft pairs taken disregarding the order, i.e.,

$$d = \frac{N!}{2!\,(N-2)!} = \frac{N(N-1)}{2} \qquad \text{(B.8)}$$

Cost function is defined as the total duration of the flight, i.e.:

$$J = \int_{t_0}^{t_f} d\tau \qquad \text{(B.9)}$$

Let define the Hamiltonian function as the scalar

$$H = 1 + \lambda^T f + \mu^T C \tag{B.10}$$

where

$$\lambda_i = \begin{bmatrix} \lambda_{x_i} \\ \lambda_{y_i} \end{bmatrix} \qquad\qquad i = 1,\dots,N \quad \lambda \in \mathbb{R}^{2N \times 1} \tag{B.11}$$

$$\mu_{ij} = \mu_k \qquad\qquad k = 1,\dots,d \quad \mu \in \mathbb{R}^{d \times 1} \tag{B.12}$$

are the vectors of Lagrange multipliers for each aircraft i, and multiplier of inequality constrains for each pair of aircraft ij, respectively.

With these definitions in mind, let cast the collision avoidance problem as OCP, i.e.,

$$\begin{aligned}
&\underset{u}{\text{minimize}} && J \\
&\text{subject to} && \dot{X}_i - f_i = 0, \quad i = 1,\dots,N \\
& && C_{i,j} \le 0, \quad i = 1,\dots,N \ \ j = i+1,\dots,N \\
& && \phi\left[X_i(t_0), t_0, X_i(t_f), t_f\right] = 0, \quad i = 1,\dots,N
\end{aligned} \tag{B.13}$$

Problem (B.13) is solved by indirect method, i.e., by formulating and solving the following MPBVP

$$\begin{aligned}
(a) \quad \dot{X} &= \frac{\partial X}{\partial t} = \frac{\partial H}{\partial \lambda} \\
(b) \quad \dot{\lambda} &= \frac{\partial \lambda}{\partial t} = -\frac{\partial H}{\partial X}
\end{aligned} \tag{B.14}$$

where control $u(t)$ is determined by

$$\frac{\partial H}{\partial u} = \lambda^T \frac{\partial f}{\partial u} + \mu^T \frac{\partial C}{\partial u} = 0 \tag{B.15}$$

and μ has to satisfy the *complementarity* condition expressed as

$$\mu = \begin{cases} > 0 & C = 0, \quad \text{(constrained arc)} \\ = 0 & C < 0, \quad \text{(unconstrained arc)} \end{cases} \tag{B.16}$$

Equations (B.14)(b) (equation of motion of the costates) and (B.15) are the necessary conditions for the optimality, and together are called Euler-Lagrange equations.

B.3.1   Considerations on μ

When inequality constraints are functions of only state variables, as in this case, additional considerations are required for obtaining some expression for μ during the constrained arc. In facts, from the optimality condition

$$\frac{\partial H}{\partial u} = \lambda^T \frac{\partial f}{\partial u} + \mu^T \frac{\partial C}{\partial u} = 0 \tag{B.17}$$

if the term $\frac{\partial C}{\partial u} = 0$ (since $C = C(x)$), no information is obtained for μ. To overcome this problem, successive total time derivatives of C can be taken until an explicit dependence on u appears. Thereafter, Euler-Lagrange equations are reformulated substituing C for its qth total time derivative $C^{(q)}$ in the Hamiltonian, as

$$H = 1 + \lambda^T f + \mu^T C^{(q)} \tag{B.18}$$

Let take the first total time derivative of C:

$$\dot{C} = \frac{\mathrm{d}C}{\mathrm{d}t} = \frac{\partial C}{\partial t} + \frac{\partial C}{\partial x}\frac{\partial x}{\partial t} + \frac{\partial C}{\partial y}\frac{\partial y}{\partial t} \tag{B.19}$$

in matrix form:

$$\dot{C} = \left[\frac{\partial C}{\partial x}\middle|\frac{\partial C}{\partial y}\right] \cdot f \quad \dot{C} \in \mathbb{R}^{d \times 1} \tag{B.20}$$

Let A be the matrix:

$$A = \left[\frac{\partial C}{\partial x}\middle|\frac{\partial C}{\partial y}\right] \qquad A \in \mathbb{R}^{d \times 2N} \tag{B.21}$$

$\dot{C}$ can be expressed as

$$\dot{C}(x,u) = A(x) \cdot f(u) \tag{B.22}$$

and, as expected, the above expression shows an explicit dependence on control $u(t)$.

For the unconstrained arc ($C < 0$ and $\mu = 0$) the equations

$$\frac{\partial H}{\partial u} = \lambda^T \frac{\partial f}{\partial u} = 0 \qquad \text{(N algebraic equations)} \tag{B.23}$$

determine $u(t)$.

For the constrained arc ($C = 0$ and $\mu > 0$), the equations

$$
\begin{aligned}
&(a) \quad \dot{C}(x,u) = 0 \quad\quad\quad\quad\quad\quad \text{(d algebraic equations)} \\[2mm]
&(b) \quad \frac{\partial H}{\partial u} = \lambda^T \frac{\partial f}{\partial u} + \mu^T \frac{\partial \dot{C}}{\partial u} = 0 \quad \text{(N algebraic equations)}
\end{aligned}
\tag{B.24}
$$

together determine $u(t)$ and μ.

B.4   Perturbation method

Instead of solving directly the MPBVP presented above, the perturbation method is applied to approximate the exact solution. Assuming that Γ is small (and it should be small when compared to the characteristic length of the domain), states and costates can be expanded in terms of Γ:

$$
\begin{aligned}
x_i &= x_i^{(0)} + \Gamma x_i^{(1)} + \Gamma^2 x_i^{(2)} + \mathscr{O}(\Gamma^3) && \text{(B.25)} \\
y_i &= y_i^{(0)} + \Gamma y_i^{(1)} + \Gamma^2 y_i^{(2)} + \mathscr{O}(\Gamma^3) && \text{(B.26)} \\
\lambda_{x_i} &= \lambda_{x_i}^{(0)} + \Gamma \lambda_{x_i}^{(1)} + \Gamma^2 \lambda x_i^{(2)} + \mathscr{O}(\Gamma^3) && \text{(B.27)} \\
\lambda_{y_i} &= \lambda_{y_i}^{(0)} + \Gamma \lambda_{y_i}^{(1)} + \Gamma^2 \lambda y_i^{(2)} + \mathscr{O}(\Gamma^3) && \text{(B.28)}
\end{aligned}
$$

It is expected that also Hamiltonian function can be expanded in series of Γ, as:

$$
H = H_0 + \Gamma H_1 + \Gamma^2 H_2 + \mathscr{O}(\Gamma^3)
\tag{B.29}
$$

with H, H_0, H_1, H_2 to be determined. Let recall the state and costate equation of motions given by Equation (B.14)

$$
\begin{aligned}
&(a) \quad \frac{\partial X}{\partial t} = \frac{\partial H}{\partial \lambda} \\[2mm]
&(b) \quad \frac{\partial \lambda}{\partial t} = -\frac{\partial H}{\partial X}
\end{aligned}
\tag{B.30}
$$

The expansions (B.25)-(B.28), truncated at order one, are introduced into the left-hand side of Equations (B.14) (a) and (b) as

$$\frac{\partial X}{\partial t} = \frac{\partial X^{(0)}}{\partial t} + \Gamma \, \frac{\partial X^{(1)}}{\partial t} \tag{B.31}$$

$$\frac{\partial \lambda}{\partial t} = \frac{\partial \lambda^{(0)}}{\partial t} + \Gamma \, \frac{\partial \lambda^{(1)}}{\partial t} \tag{B.32}$$

By taking the derivatives $\frac{\partial H}{\partial \lambda}$ and $\frac{\partial H}{\partial X}$, and by comparing (B.14) with (B.31) and (B.32), it should be possible to identify the kth-order terms of the equations of motion for state and costates. Once these terms are identified, instead of solving the entire problem, it should be possible to solve a N sub-problems handling with the state and costate equation of motion of each order.

Appendix C

Moving Obstacle OCP - Indirect Method Formulation

In this section, the preliminary mathematical formulation of the CD&R in presence of a moving obstacle is presented. The objective is to lead an aircraft from initial waypoint until the terminal waypoint of its route, while avoiding a moving obstacle and minimizing the time of flight. The necessary conditions of optimality are derived from Euler-Lagrange equations, and the resulting MPBVP is similar to that treated in Section 4.4 of this work.

Let consider the bi-dimensional scenario depicted in Figure 4.1. Under the assumption of heading angle control only, and constant aircraft true airspeed V, the vector of state variables $\boldsymbol{x}(t)$, controls $\boldsymbol{u}(t)$ and dynamics, are introduced as

$$\boldsymbol{x}(t) = \begin{bmatrix} x(t) \\ y(t) \end{bmatrix} \tag{C.1}$$

$$\boldsymbol{u}(t) = \boldsymbol{\chi}(t) \tag{C.2}$$

$$\boldsymbol{f}\left[\boldsymbol{x}(t), \boldsymbol{u}(t)\right] = \dot{\boldsymbol{x}}(t) = \boldsymbol{V} = \begin{bmatrix} V\cos\chi(t) \\ V\sin\chi(t) \end{bmatrix} \tag{C.3}$$

where $x(t)$, $y(t)$ are the Cartesian coordinates of the aircraft, and $\chi \in [-\pi, \pi]$ is the aircraft heading angle.

With reference to Figure C.1, let introduce also the moving obstacle as a circular shape of radius Γ, which center moves with constant speed V_{ob}, and constant ground
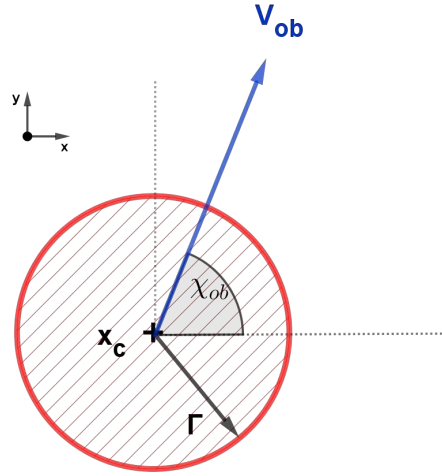
Figure C.1: Moving obstacle characterization.

track heading angle χ_{ob}. In mathematical terms, no conflicts occur as long as

$$C(\boldsymbol{x},t) = 1 - \sqrt{\frac{(x - x_C(t))^2}{\Gamma^2} + \frac{(y - y_C(t))^2}{\Gamma^2}} \le 0 \qquad t \in [t_0, t_f] \qquad (C.4)$$

where $x(t)$, $y(t)$ are the 2-dimensional coordinates of the aircraft, and $x_C(t), y_C(t)$ are the components of the time-dependent obstacle position defined as

$$\boldsymbol{x_C} = \begin{bmatrix} x_C(t) \\ y_C(t) \end{bmatrix} = \begin{bmatrix} x_{C0} \\ y_{C0} \end{bmatrix} + \boldsymbol{V_{ob}}\, t = \begin{bmatrix} x_{C0} + V_{ob}\cos\chi_{ob}\, t \\ y_{C0} + V_{ob}\sin\chi_{ob}\, t \end{bmatrix} \qquad (C.5)$$

with x_{C0}, y_{C0} are the coordinates of obstacle center at initial time.

As done in Section 4.4, it is supposed that optimal solution can be divided in one unconstrained arc ($C < 0$), followed by one constrained arc ($C = 0$), and eventually another unconstrained arc.

Equation (3.1) of Section 3.3 defines the performance index J as

$$J = \int_{t_0^+}^{t_f^-} dt \ . \qquad (C.6)$$

For the unconstrained arc, i.e., when $C < 0$ and $\mu = 0$, the Euler-Lagrange Equations (3.32)-(3.34) become

$$\dot{x} = f \tag{C.7}$$

$$\dot{\lambda} = 0 \tag{C.8}$$

with the algebraic equation to determine control u as

$$\lambda^T \frac{\partial f}{\partial u} = 0 \tag{C.9}$$

and same boundary condition of Equations (4.11) - (4.14). The considerations done in Section 4.4 for the unconstrained trajectory and junction points (internal point constraints) remain valid for this problem.

For the constrained arc, Equation. (3.45) is used to define the Hamiltonian as

$$H = 1 + \lambda^T f + \mu C^{(p)} . \tag{C.10}$$

If the first total time derivative of C is taken as

$$\dot{C} = \frac{dC}{dt} = \frac{\partial C}{\partial t} + \frac{\partial C}{\partial x}\frac{\partial x}{\partial t} + \frac{\partial C}{\partial y}\frac{\partial y}{\partial t} \tag{C.11}$$

and if relation $C = 0$ is used, the following expression is obtained

$$\dot{C} = \frac{1}{\Gamma^2}(x - x_C) \cdot (V_{ob} - V) \tag{C.12}$$

$$= \frac{1}{\Gamma^2}[(x - x_C(t))(V_{ob}\cos\chi_{ob} - V\cos\chi) + (y - y_C(t))(V_{ob}\sin\chi_{ob} - V\sin\chi)] \tag{C.13}$$

For the constrained arc ($C = 0$ and $\mu \neq 0$), the Euler-Lagrange Equations (3.32)-(3.34) become

$$\dot{x} = f \tag{C.14}$$

$$\dot{\lambda} = -\mu \frac{\partial \dot{C}}{\partial x} \tag{C.15}$$

subject to the algebraic equations

$$\dot{C}(\boldsymbol{x}, \boldsymbol{u}, t) = 0 \tag{C.16}$$

$$\frac{\partial H}{\partial \boldsymbol{u}} = \boldsymbol{\lambda}^T \frac{\partial \boldsymbol{f}}{\partial \boldsymbol{u}} + \boldsymbol{\mu}^T \frac{\partial \dot{C}}{\partial \boldsymbol{u}} = 0. \tag{C.17}$$

which together determine $\boldsymbol{u}(t)$ and $\boldsymbol{\mu}$. Defining the interior point constraint N as

$$N(\boldsymbol{x}, t) = C(\boldsymbol{x}, t) \tag{C.18}$$

which has been arbitrarily chosen to be satisfied at et the exit point t_B, the optimality boundary conditions for the unconstrained arc are as follow

$$\boldsymbol{x}(t_{A+}) = \boldsymbol{x}(t_{A-}) \tag{C.19}$$

$$\boldsymbol{x}(t_{B+}) = \boldsymbol{x}(t_{B-}) \tag{C.20}$$

$$C(\boldsymbol{x}(t_{A+})) = 0 \tag{C.21}$$

$$C(\boldsymbol{x}(t_{B-})) = 0 \tag{C.22}$$

$$\boldsymbol{\lambda}(t_{A+}) = \boldsymbol{\lambda}(t_{A-}) \tag{C.23}$$

$$\boldsymbol{\lambda}(t_{B+}) = \boldsymbol{\lambda}(t_{B-}) + \pi \left. \frac{\partial N}{\partial \boldsymbol{x}} \right|_{\boldsymbol{x}(t_{B+})} \tag{C.24}$$

$$H(t_{A+}) = H(t_{A-}) \tag{C.25}$$

$$H(t_{B+}) = H(t_{B-}) + \pi \left. \frac{\partial N}{\partial t} \right|_{t_{B+}} \tag{C.26}$$

where π is a constant non-zero scalar.

With respect to the problem solved in Section 4.4, some differences deriving from time dependent constraint C have to be pointed out. First of all, costate equations of motion of Equation (C.15) are quite different, therefore controls evolution will follow a different trend. In particular, one can intuitively envisage the optimal trajectory as two straight line joined by a trajectory typical of cycloidal motions. Indeed, with respect to an external inertial reference frame, the constrained trajectory is that traced by a point moving tangent to a circle while its center is translating along a straight line. The second relevant difference is represented by the jump entailed in the Hamiltonian at the exit point t_B. In facts, with reference to Equation (C.26), the

vector

$$\left.\frac{\partial N}{\partial t}\right|_{t_{B+}} = \frac{(\boldsymbol{x}(t_B) - \boldsymbol{x}_C(t_B)) \cdot \boldsymbol{V}_{ob}}{\Gamma^2} \tag{C.27}$$

is in general not zero. Discontinuity of costates at t_B (Equation (C.24)) also changes slightly, in facts, the vector

$$\left.\frac{\partial N}{\partial \boldsymbol{x}}\right|_{\boldsymbol{x}_{(t_{B+})}} = -\frac{(\boldsymbol{x}(t_B) - \boldsymbol{x}_C(t_B))}{\Gamma^2} \tag{C.28}$$

is in general not zero.

When compared to the problem of Section 4.4, other different conditions on Hamiltonian can be highlighted. Since during constrained arc Hamiltonian function has an explicit dependence on time, recalling Equation (3.41)

$$\dot{H} = \frac{\partial H}{\partial t} \neq 0. \tag{C.29}$$

it can be asserted that Hamiltonian zero during unconstrained arc, but different than zero during constrained arc.